APS (2004) 170:169–273
DOI 10.1007/b94405

Two-Photon Photopolymerization and 3D Lithographic Microfabrication

Hong-Bo Sun[1, 2] (✉) · Satoshi Kawata[1, 3] (✉)

[1] Department of Applied Physics, Osaka University, Suita, 565–0871 Osaka, Japan
hbsun@ieee.org
kawata@ap.eng.osaka-u.ac.jp
[2] PRESTO, Japan Science and Technology Corporation (JST), Japan
[3] RIKEN (The Institute of Physical and Chemical Research), Hirosawa, Wako, 351–0198 Saitama, Japan
kawata@ap.eng.osaka-u.ac.jp

Abstract This chapter attempts to give an overview of the historical development and current progress of femtosecond laser micro-nanofabrication based on multiphoton absorption, and particular emphasis is placed on two-photon photopolymerization. Femtosec-

ond laser interaction with matter differs essentially from those with longer pulses or CW lasers in its significant nonlinearity, ultrafast characteristics and the possibility of highly localization of reaction volume. These features enable three-dimensional (3D) micro-nanofabrication in solid and liquid media. In two-photon photopolymerization, when a near-infrared femtosecond laser is tightly focused into a photopolymerizable resin, 3D polymer micro-nanostructures are produced by pinpoint photopolymerization of liquid precursory resins. Using this direct laser writing scheme, various photonic, micro-optical components and micromechanical devices have been readily produced. The two-photon photopolymerization technology is expected to play a similar role to that played by lithography for planar semiconductor device processing, but for micro-nanofabrication of 3D polymer-based optoelectronic devices as well for microelectromechanical systems.

Keywords 3D lithography · Two-photon photopolymerization · Femtosecond laser · Micro-nanodevice · Micro-nanofabrication

Abbreviations and Symbols

2D	Two-dimensional
3D	Three-dimensional
AFM	Atomic force microscope
B1536	1,2-Dicyano-1,2-bis(2,4,5-trimethyl-3-thienyl)ethane
BCC	Body-centered cubic
BSA	Bovin serum albumin
CAM	Computer-aided manufacturing
CAD	Computer-aided design
CCD	Charge coupled device
CW	Continuous wave
DBR	Distributed Bragg reflection
DFB	Distributed feedback
DMF	Dimethyl formamide
FCC	Face-centered cubic
FWHM	Full width at half maximum
HCP	Hexagonal close packing
IR	Infrared
LD	Laser diode
LED	Light emitting diode
μCP	Microcontact printing
MEMS	Microelectromechanical system
MMA	Methyl methacrylate
MW	Molecular weight
NA	Mumerical aperture
NIR	Near-infrared
NSOM	Near-field scanning optical microscope
PAG	Photoacid generator
PBG	Photonic bandgap
PDMS	Poly(dimethyl siloxane)
PhC	Photonic crystal
PMMA	Poly(methyl methacrylate)
PSF	Point spread function
PVK	Poly(vinyl carbazole)
PZT	Lead zirconate titanate

R	Radical
RB	Rose Bengal
S	Photosensitizer
SC	Simple cubic
SDL	Sub-diffraction-limited
SEM	Scanning electron microscope
SLI	Square of light intensity
SLM	Spatial light modulator
STM	Scanning tunneling microscope
TE	Transverse electric
THPMA	Tetrahydropyranyl methacrylate
TM	Transverse magnetic
TPA	Two-photon absorption
TPE	Two-photon excitation
UV	Ultraviolet
Voxel	Volume element
XUV	Extreme UV
n	Refractive index
δ	Two-photon absorption cross-section
ϵ	Electrical permittivity
T_g	Glass transition temperature
E	Electric field strength; Young's modulus
I	Light intensity
λ	Wavelength
ν	Lightwave frequency
l_c,	Coherence length
Q	Quality factor
ω_0,	Beam waist of Gaussian beam
Z_R	Rayleigh depth
ϕ_{H+}	Quantum efficiency of proton generation
G_s	Shear modulus

1 Introduction

The last decade has witnessed rapid progress in high-performance ultraviolet (UV)-curable systems [1–5], which have resulted in a growing number of industrial applications, including paints, optical adhesives, medicine, coatings, graphic arts, microelectronics, optics, manufacturing, and so forth. It is estimated the world consumption of UV curable products in the year 2000 is around 200,000 tons, which corresponds to a two billion dollar market. Requirements of monomers and oligomers of novel function, active photoinitiators, and more efficient photosensitizers are increasing, which will prompt market growth.

Among the above applications, *computer-aided manufacturing (CAM)* using UV curable resin, generally called *laser rapid prototyping*, is a new and expanding technology [6–9]. It converts three-dimensional (3D) objects of

complex shape, designed via *computer-aided design (CAD)*, from designs into real products. The resin used for fabrication is photocured at the spot exposed to UV laser, a *single-photon photopolymerization* process. By scanning the laser beam, one slice of the 3D structure is first hardened according to the design patterns; and then a thin-layer liquid resin is added and a new patterned slice is polymerized. The entire structure is sequentially created the same way. This technology is suitable for manufacturing devices that are difficult or costly to prepare by conventional mechanical methods.

Commercial laser rapid prototyping machines have a fabrication precision greater than 10 μm. This accuracy cannot fully satisfy the modern requirements for device multifunctionalization and miniaturization that demand sub-micron feature size. The emergence of a new technology in 1997, *two-photon photopolymerization* [10], has brought the light curable resin into the realm of nanofabrication. As indicated by the name, the resins are polymerized not by absorbing one UV photon, but by simultaneously absorbing two photons at longer wavelength, usually in the red-infrared (IR) spectral region. The two-photon process [11–13] has at least two advantages compared to single-photon absorption used in conventional rapid prototyping. First, common polymers have negligible linear absorption in the red-near-infrared (NIR) region, so the laser penetrates deeply into materials and directly induces polymerization from inside without contaminating outside of the focal volume; secondly, the quadratic dependence of polymerization rate on the light intensity enables 3D spatial resolution, and the accuracy is better than that achieved in single photon process. Actually a near 100-nm lateral spatial resolution has been reported [13, 14]. Two-photon polymerization, as currently the only microprocessing approach that has intrinsic 3D fabrication capability, has been successfully applied to production of a variety of photonic and micromechanical devices [15–20]. It accomplishes manufacturing that is otherwise not accessible and brings new scientific possibilities to nano-research.

The current research effort in two-photon photopolymerization is largely devoted to the synthesis of high-efficiency photoinitiators and sensitizers [21–25], about which good reviews have been published in this series. Nevertheless, as a new technology, there is a lot of work that has been done to establish it as a nanoprocessing tool, which is the major content of this review. So, in the next section, we will introduce the general stereolithography concept, which we define as the technology that is utilized to produce stereostructures using lasers, although here we are more concerned with processes that address submicron features using multiphoton processes.

Following that, we will discuss the principles and materials of two-photon photopolymerization, as well as the systems used, and ground-work performed in this area. Then we turn our focus in the next section to the advanced technologies that have been developed, and in the final section we look at some applications of the technique. You should note, however, that

our content selections for the advanced technologies section are quite subjective, since it is difficult to know which approaches will withstand the test of time.

2 General Stereolithography Using Femtosecond Lasers

Stereolithography historically refers to the technology of creating 3D objects from CAD patterns by adding and exposing photopolymerizable resin layer by layer. Nowadays, materials that are useful for 3D laser modeling have extended to gas phase [26, 27], chemical solutions [28], metal powders [29, 30] and transparent glassy or crystalline solids [31, 32]; the lasers used as an irradiation source range from extreme UV (XUV) to NIR wavelengths, operating at continuous wave (CW) to pulsed mode at nanosecond (ns), picosecond (ps) and femtosecond (fs) widths [33–35]; 3D patterns are created using either multi-beam interference [36–39] or direct laser writing, and the writing does not necessarily start from the surface layers but is accomplishable from inside materials via multiphoton pinpoint addressing [13–20]. Correspondingly, the concept of stereolithography has been broadened. Here we focus our topics only on the latest progress that involves the use of femtosecond lasers. These technologies share common features such as the dominant role of nonlinear effects in laser material interactions and the similarity in experimental techniques. An overview of the entire family should facilitate an understanding of the origin, the current status, and future direction of the two-photon photopolymerization technology.

2.1 Material Processing with Femtosecond Lasers

The basis of laser fabrication is laser material processing [40, 41], which started soon after the first demonstration of the ruby laser in 1960. Due to the poor beam quality and reproducibility of lasers, initial works were largely qualitative, mainly devoted to simple research like material evaporation. With the emergence of new-type lasers such as Nd (Nd-doped YAG or glass), CO_2, Ar ion, and excimer lasers, and the improvement of laser performance, the field was expanded to laser annealing, crystallization of amorphous layers, compound synthesis, plasma formation, and laser cutting, hole-drilling, welding, jointing, and so forth. The commercialization of tunable solid ultrashort pulse lasers (for example the Ti:Sapphire laser) in the 1990 s pushed forward these applications and opened new domains such as controlling, manipulation and processing of biological and nanoscale species. Today's commercial laser systems have already been able to provide output power up to 10^{20} W in pulse duration with a good beam quality, and up to several

kilowatts in CW mode, although usually with worse beam quality. Laser pulse duration has reached less than 5 fs, wavelengths cover a region from a few nm in the XUV to the far IR with several tens of μm, and pulse energies reach up to 10^4 J , while frequency stability and resolution better than 10^{-13} is already available. With the excellent laser beam quality, coherence, power and frequency stability, short pulse duration, and high transient power, almost any kinds of material can be processed by lasers in a well-controlled manner.

Nonlinear processes [33, 42, 43], for example, *multiphoton absorption* including *two-photon absorption (TPA)* [11, 12, 25], has come to play a dominant role in nanofabrication. In order to produce a lasting effect on a material, photons must first be absorbed. The energy and momentum are exchanged between the optical fields and molecules through absorption and emission. In such a process, the imaginary part of nonlinear susceptibility represents the energy transfer from the light field to a medium. The light-matter energy change per unit time and unit volume is:

$$\frac{dW}{dt} = \left\langle \vec{E} \cdot \dot{\vec{P}} \right\rangle \tag{1}$$

where $\vec{E}$ is the electric field vector and the brackets denote time average. The value of material polarization $\vec{P}$ is:

$$P = \chi^{(1)}E + \chi^{(2)}E^2 + \chi^{(3)}E^3 + \cdots \tag{2}$$

where the quantities of $\chi^{(1)}$, $\chi^{(2)}$, $\chi^{(3)}$ are second-, third-, and fourth-rank tensors, representing linear, second-order and third-order optical susceptibilities. In resonant processes, there is no contribution from the even-order susceptibilities like $\chi^{(2)}$ and $\chi^{(4)}$. Therefore, the nonlinear absorption is described by the imaginary parts of $\chi^{(3)}$, $\chi^{(5)}$, of which typical effects are two-photon and three-photon absorptions, respectively. Particularly, for degenerate TPA, that is, the process of photons of identical energy are simultaneously absorbed, the energy absorption rate is:

$$\frac{dW}{dt} = \frac{8\pi^2\omega}{c^2n^2} I^2 \operatorname{Im}\left[\chi^{(3)}\right] \tag{3}$$

It is seen that the TPA rate quadratically depends on the light intensity, which is an important mechanism to improve the spatial resolution in two-photon fabrication. A high capability of materials to absorb photons via TPA is desired, which is described by *TPA cross-section*, δ, defined by

$$\frac{dn_{\mathrm{p}}}{dt} = \delta N F^2 \tag{4}$$

where N and n_p are the number density of absorbing molecules and number of absorbed photons, respectively, and $F=I/h\nu$ denotes photon flux. According to Eq. 4), the TPA cross-section is:

$$\delta = \frac{8\pi^2 h\nu^2}{c^2 n^2 N} I^2 \mathrm{Im}\left[\chi^{(3)}\right] \tag{5}$$

The design of molecules that have a large TPA cross-section is an important task of stereolithography using two-photon photopolymerization. We will discuss work related to this in Sect. 3.1.3.

In order to take advantage of nonlinear effects, the use of ultrashort laser excitation is essential. In the early 1990 s, it was recognized that laser-matter interactions for femtosecond pulses were fundamentally different from interactions resulting from longer pulses or CW lasers [44–46]. First, a femtosecond laser carries much greater peak power. With conventional light sources the strength of the light field is in the range of 1 V/cm and the resulting elongation of dipole is smaller than 10^{-16} m, much smaller than atomic or molecular diameters (10^{-10}~10^{-7} m). With femtosecond laser irradiation, the field strength could be as intense as 10^8 V/cm, sufficient to induce direct bond breaking. Various nonlinear effects could be easily launched, among which (the most important for laser fabrication) is multiphoton absorption. Multiphoton absorption has an extremely small cross-section; it is confined to occur only in a small 3D volume around the close vicinity of the laser focus, less than the cubic wavelength (λ^3). Hence, a quite high 3D spatial resolution can be achieved in the pinpoint exposure. Secondly, when materials are irradiated with a femtosecond laser pulse, the photon energy is deposited much faster than electrons could transfer it to the lattice, or molecule/atom oscillations through phonon emission, meaning that the excitation is a heat insulation process [47–49]. This provides an ideal optical excitation means for many photochemical or photophysical reactions where thermal effects, a process difficult to localize, are not desired. In addition, for many dielectric materials, there is a transparent window in the red-NIR spectral region, which is covered neither by electronic band-band absorption nor by atomic/molecular oscillation absorption. It happens that the fundamental wavelength of general femtosecond lasers is located in this regime, for example, 680–1000 nm for Ti:Sapphire laser. Therefore a femtosecond laser can penetrate into and tailor desired structures from inside transparent materials, giving an intrinsic 3D processing capability.

2.2 Femtosecond Laser 3D Micro-Nanofabrication

Although multiphoton absorption was predicted as early as 1931 [50] and experimentally observed immediately after the invention of lasers [51], the technology found limited application, for example, solely as a spectroscopic

tool [52], due to the extremely small absorption cross-section of most materials. With the advent of convenient femtosecond lasers the utility of multiphoton excitation processes has undergone a rebirth in the past decade. Fluorescent imaging of biological molecules is one of the most important uses [24, 25, 53–55]. Additional usage includes fluorescence up-conversion [56], power limiting [57], photodynamic therapy [58], two-photon lasing [59], cell surgery [60], ultrasonic generation [61], and certainly micro-nanofabrication. As a stereolithographic approach, the femtosecond laser has found considerable use in optical memory, micro optical components, photonic crystals and complicated 3D patterning.

2.2.1 3D Optical Memory

Conventional optical recording media like compact disks (CDs) and magneto-optical (MO) disks register binary bits, spots with optically modified phase status or refractive index, in an active layer of the disk, by which information of about $10^8/cm^2$ is recordable using visible light at the diffraction limit. The information capacity in a disk volume can be expanded by means of multi-layer recording [11, 62, 63]. A simple scheme is to focus the laser at a series of different depths in an optically thick active media, and at each depth, a bit plane is recorded. Estimated from the diffraction-limit-defined volume, a storage density as high as 10^{12} bits/cm^3 is possible. However, in linear recording-reading (single-photon absorption for both processes), the same amount of photon energy is absorbed in each plane transverse to the optical axis since nearly the same amount of photon flux crosses them. This strongly contaminates the planes above and below the particular focal plane to be addressed, causing the issue of crosstalk. Therefore it is quite difficult to realize the multilayer recording strategy by a single photon process.

This problem was solved by using multiphoton absorption. First the intrinsic nature of deep penetration allows a laser to address a certain depth inside materials without power dissipation; and secondly, the excitation depends roughly on n-order of the intensity so that net excitation per distant plane falls off sharply, where "n" means n-photon absorption. This enables recordings in well-separated layers and minimizes the crosstalk. Compared to other approaches to 3D optical data storage, like holographic recording on photorefractive media [64], hole burning [65], photon echo [66], and encoded thin disc stacking, the multiphoton method has the merits of highest storage capacity (up to terabits/cm^3), random access, fast write-read times, possibility of erasing and rewriting, and low cost.

Multi-photon-induced modification of optical properties of materials including refractive index, absorbance, polarization and fluorescence appearance or wavelength shifting could be utilized for 3D optical memory in various media, including polymers, inorganic crystals, or glasses.

2.2.1.1 Isomerization of Photochromic Materials

Photochromic molecules [11, 67] exist in two chemically stable isomer forms, and the two isomers are inter-switchable by photochemical reactions after absorbing light of different wavelengths. This implies that they can be used for rewritable optical memory. The two isomers differ in their absorption, refractive index, fluorescence wavelength, and even molecular orientation-induced polarizations, permitting recorded binary bits of one isomer status embedded in a matrix of the other isomer status. To be a good 3D storage medium, the material should have high sensitivity and fast response to excitation, stable isomers at both two states, and high resistance to fatigue during cyclic writing and erasing. Three classes of molecules, spirobenzopyran [11], diarylethene [68] and azobenzene [63, 69] and their derivatives are found to be promising for this purpose. Particularly, diarylethene derivatives with heterocyclic rings exhibit no thermochromicity up to 200 °C; their colored close-ring forms are stable for more than three months at 80 °C; and no significant fatigue has been observed even after 10^4 cyclization/ring open

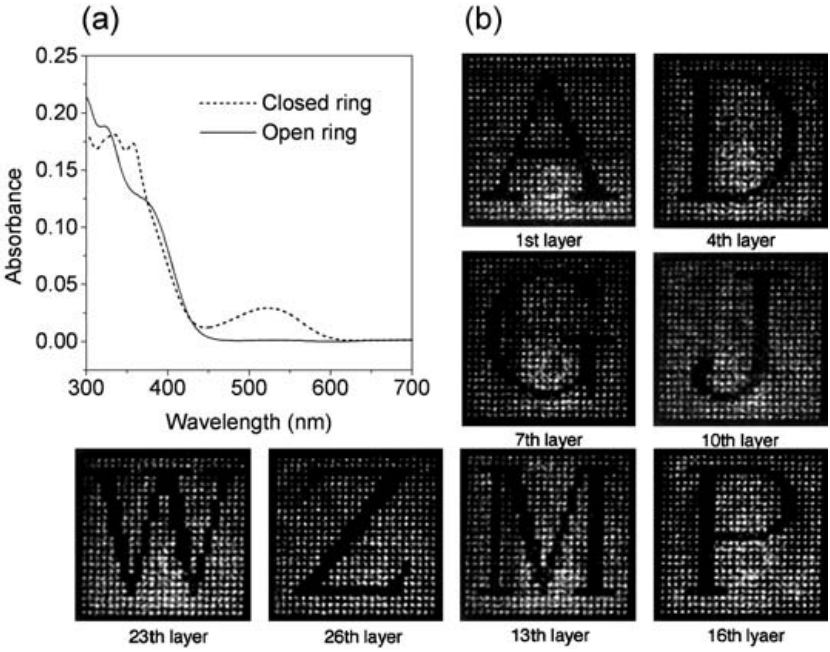

Fig. 1 Photochromic materials for 3D optical memory. **a** Absorption spectra of open-ring and closed-ring diarylethene derivative B1536. **b** Bit patterns written by femtosecond two-photon absorption and readout using a reflection confocal microscope. Refer to Fig. 60b for ring close-open reactions

reaction cycles [67]. As an example of multilayer writing and reading, Fig. 1 shows absorption spectra of two-form 1,2-dicyano-1,2-bis(2,4,5-trimethyl-3-thienyl)ethane (B1536) (Fig. 1a) and several two-photon recorded bit patterns out of 26 sequential bit planes (Fig. 1b) [63, 70]. Bits were recorded by exciting the 380-nm absorption of open-ring isomers (red color) using a 760-nm femtosecond laser. The bits consist mostly in the form of close-ring isomers (yellow). The recording layer and bit intervals are 5 μm and 2 μm, respectively. The refractive index change around 10^{-4} was distinguished and readout by a reflection confocal microscope.

The current major issue in photochromatic memory is that, although isomers are stable in respective single-phase bulk form, when the bits are embedded in the matrix with opposite isomer status, they are liable to relax, losing contrast. Further work on material stability is apparently needed.

2.2.1.2 Photorefraction, Photopolymerization, Photobleaching and Photoreduction Effects

The photorefraction effect [64, 34] has been utilized for holographic memory for many years. The mechanism is that, when a photorefractive material such as $BaTiO_3$, $Bi_{12}SiO_{20}$, $LiNbO_3$, $KNbO_3$, GaAs, SBN or nonlinear functional polymers is exposed to light, free charge carriers (electrons or holes) are generated by excitation, in most cases from impurity energy levels, and these diffuse, leaving behind fixed charges of opposite sign. This charge distribution creates an internal electric field that causes local refractive index change by virtue of Pockel's effect. Since photoinduced spatial charges (and therefore the refractive index) depend on only on the irradiation history of a local site, it is possible to induce refractive index change either by frame (holographic) or on a bit basis. Then single bit and single frame addressing that is not possible in holographic memory becomes natural in the bit recording scheme. Bit-orientated two-photon memory in inorganic $LiNbO_3$ crystal [71], poly(vinyl carbazole (PVK) [72] and poly(methyl methacrylate) (PMMA)-based [73] polymeric photorefractive materials has been realized using this technique. The attribute of charge distribution implies, on one hand, the possibility of erasing and rewriting, on the other hand, the bit information is easy to lose by uniform illumination or by heating.

The refractive index change in photorefractive materials is generally small, of the order of $\Delta n/n<10^{-3}$. Large change of n can be achieved in a different scheme, photopolymerization [62]. The mass density increases after polymerization gives rise to $\Delta n/n\sim1\%$. In this case, two-photon solidified small volume elements (voxels) that are suspended in unpolymerized matrix are treated as binary bits. However, the gel status and light sensitivity of the recording media make the technology impractical.

Different from the need to sensitively detect the refractive index change, bits recorded as points of emergence or disappearance of a certain fluorescence band make for easier reading. Fluorescent dye can be photobleached by strong excitation, generally by long pulses or CW laser [74]. The bleached volumes do not produce fluorescence. As a consequence, the places that have been bleached show up as darker areas than their surroundings when the recorded information is read out in a fluorescence microscope.

A direct use of the fluorescence approach is the photoreduction of noble [75] (for example Au^{3+} and Ag^{+}) and or rare-earth (for example Sm^{3+} and Eu^{3+}) [76, 77] metals. For instance, Sm^{3+} in glass can be space-selectively photoreduced with an IR femtosecond laser. It is found that after photoreduction from Sm^{3+} to Sm^{2+}, a pronounced fluorescence band appears at 650~775 nm, which has been used as readout signal of 3D memory [77]. Another outstanding characteristic is that photoreduced Sm^{2+}, stable at room temperature, can be converted back to Sm^{3+} by photo-oxidation with a CW laser, such as an argon-ion laser or a semiconductor laser. This enables rewritable optical memory with two stable statuses.

2.2.1.3 Photodensification and Cavitation

Other than the particular photochemical reactions discussed above, there is a universal mechanism that is useful for 3D optical memory. Due to their extremely large transient power, tightly-focused femtosecond laser pulses interact with almost any kinds of materials and pinpoint mark bits inside them, provided that the media are transparent to the laser wavelength. These bits are generally visible under an optical microscope, implying a large variation of the refractive index. Although a detailed mechanism of the photoinduced changes is still an open problem, it is already well-accepted that highly-excited electron-ion plasma is produced at the focal volume during excitation [48, 49]. At relatively lower transient power, the plasma condensation induces local mass densification of materials, in case of amorphous silica up to ~3%, and at higher transient power, the plasma releases energy in an explosive way, leaving a void surrounded by a densified crust [31, 32, 48, 78]. Both the densified and cavititated spots have been utilized as the 3D memory bits in polymers [79], vitreous and active glasses [80–82], and other optical materials like diamond and sapphire. Readout is basically from the refractive index change; for example, in the case of complete cavitation of silica to vacuum, Δn~0.45 [31, 32]. For silica glass, a broad fluorescence band appears at 400~700 nm, which may arise from laser-induced defects (oxygen vacancy, E' center, peroxial bonds [78, 83]). The fluorescence signal was successfully employed for detecting bits [80–82]. The above mechanism is useful only for recordable (not erasable and rewritable) memory.

2.2.2
Micro Optical Components

Optical memory is the simplest application of 3D lithography. One just needs to focus the laser inside a recording media, irradiate it by a single pulse or by multipulses for a short duration, and then a bit is naturally produced at the focal site. More complicated optical elements are created by scanning the laser focus in three dimensions. The merit of using laser fabrication is the potential to integrate components of different dimensions and different functions into one chip, simply by one-step laser writing. For instance, on some occasions, integrating devices of different functions in conventional optoelectronic systems is quite difficult, since they are produced by different technologies and materials, (for example laser diode, LD: GaAs, ~100 μm, by epitaxy; modulator: $LiNbO_3$ ~10 mm, by "diffusion+lithography+deposition"). In contrast, these devices could be written by a laser in a single matrix chip, implying the ease of integration. Although there is a lot of work to do to realize a workable integrated optical system, separated devices have been intensively studied.

2.2.2.1
Waveguides and Couplers

Optical fiber is one of the most useful light guiding devices. However, it is not easy to provide optical connection if the light emitting, detecting, and controlling devices are prepared in-chip. The refractive index difference between the core and cladding layers of a single-mode fiber is generally of the order of $\Delta n/n$~0.1%. It is noteworthy that the ratio can be one order larger in the laser-irradiated region compared to the background in typical polymers or glasses [84]. This large contrast is sufficient to confine light inside a laser irradiated fiber line by total internal reflection, as employed in conventional fibers. Glass is a widely-used material for optical components. To write a fiber or any other structure inside silica, of which the bandgap energy can be as large as >8 eV, it is necessary to use regenerative amplification ($\times 10^4$) of pulse energy to launch multiphoton absorption. By this means, waveguides have been recorded inside various glasses such as fused and synthetic silica, Ge-doped silica, borosilicate, borate, phosphate, fluorophosphate, fluoride, and chalcogenide glasses. It was experimentally observed [84] that 15-mm-long fluoride glass waveguides of diameters 8 μm, 17 μm and 25 μm support 800-nm LP_{01}, LP_{11} and LP_{22} modes, respectively. Sikorski et al. observed a 3dB/cm gain at 1062 nm from an active waveguide inside a neodymium-doped glass substrate, from which it would be possible to produce active laser waveguides like fiber lasers or fiber amplifiers.

With the development of single-mode waveguides, it is possible to fabricate more complicated micro-optical devices such as X [85], Y [86] couplers

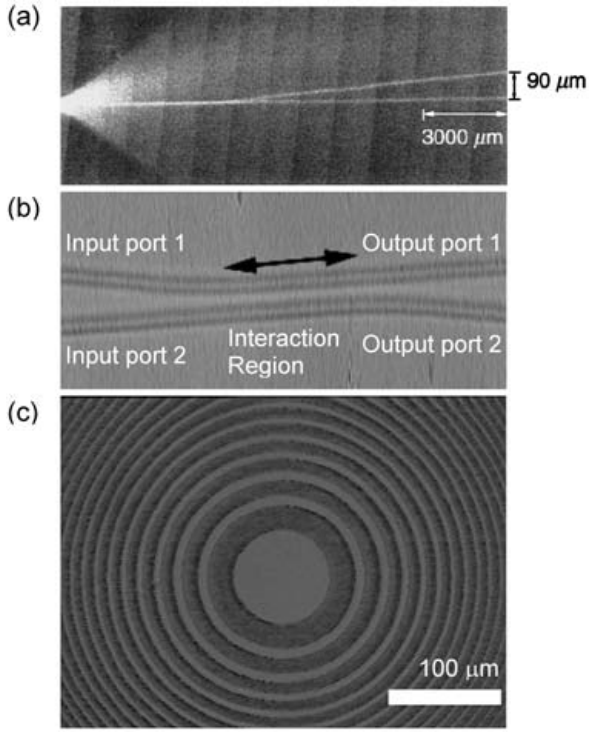

Fig. 2 Laser written micro-optical components. **a** Optical microscopic image of a Y coupler drawn in pure fused silica, which guides 514.5-nm light from an argon-ion laser. The scattered radiation from the coupled argon-ion light is observed in the photograph. The vertical direction is magnified with respect to the horizontal direction for clarity. **b** Phase contrast microscopic image of one of the two X-couplers that make up a Mach-Zehnder interferometer. **c** Optical microscopic image of a Fresnel zone plate

(Fig. 2a). An X coupler was written in glass from two identical waveguides that were crossed with each other by a small angle, α. Experimentally it was found that the individual branches are single mode and at the output the power was split into two output waveguides with ratio of 1:1 for α=1 °and 16:1 for α=4°[4], both at 800-nm wavelength [85].

If the two single-mode waveguides are instead placed parallel with and adjacent to each other at a certain length, they exchange power by mode coupling in this interaction length. This structure is a directional coupler. A directional coupler with splitting ratio of 1.9 dB at 633 nm was written in glass using a 400-nm, 25-femtosecond laser oscillator [87]. An even more complicated photonic device is a Mach-Zehnder interferometer filter. It consists of two X-couplers (Fig. 2b) placed back-to-back. Light coupled into the interferometer is split into two arms at the first X coupler, travel different path lengths, and will either constructively or destructively interfere at the

second X coupler [87]. The unbalanced Mach-Zehnder interferometer could act as a spectral filter.

2.2.2.2 Gratings and Zone Plate

Gratings are useful optical structures that could be written by two-beam interference. For femtosecond laser pulses, the coherence length is short, which needs sensitive adjustment of pulse overlapping at both spatial and temporal domains. Various gratings [88, 89] were produced in a variety of materials either by surface ablation or surface relief mechanisms. Both form phase gratings, but the former arises from mass removal and the latter is caused by mass migration. The grating periods, Λ, are determined by $\Lambda=\lambda/[2\sin(\theta/2)]$, where λ is the laser wavelength and θ the two-beam angle. The smallest grating groove that has ever been reported is 15 nm [90]. Such a fine feature was producible only in amorphous materials, implying the creation mechanism of densification. Due to the deep penetration effect, it is feasible to encode 3D grating structures inside materials [88, 89]. These works are quite similar to those we will introduce in Sect. 4.6. Another interesting micro optical component that was produced by femtosecond laser is the Fresnel zone plate (Fig. 2c). The recording femtosecond laser was focused 300 μm beneath the surface of 3-mm thick glass sample, where the silica was bombarded by regeneratively amplified laser pulses [91]. The refractive index change in the irradiated ring zones provides the phase modulation that is necessary for the plate function. In one fabricated structure, the primary focal spot size has been measured at 6.1 μm, agreeing with design, and diffraction efficiency was 2.0%.

One major problem with femtosecond laser processed micro-optical devices is the large power dissipation due to Rayleigh scatterings from the particle-like fine structures, which is difficult to control in the fabrication process because of an intense laser-matter interaction at the femtosecond time scale. Suitable post-irradiation treatments should be found to improve performance of devices [31].

2.2.3 Photonic Crystals

The *photonic crystal (PhC)* [92. 93], the optical analogue of electronic crystals, consists of two or more kinds of materials. Blocks of materials of different refractive indexes appear alternately, producing a periodic structure. The emergence of photonic bandgap (PBG) is the most important phenomenon that is associated with PhCs. Light with wavelength matching the structural periodicity is rejected in a certain direction incident upon the periodic structure. In the case where the rejection occurs at all directions, the PhC

has a *full bandgap*. To achieve the full bandgap, structures should be optimized in (i) lattice type: in other words how the primitive units repeated in three dimensions, for example, face-centered cubic (FCC), body-centered cubic (BCC), and so on; (ii) filling ratio: what percentage of the volume is occupied, for example, by the high-index material; (iii) refractive index contrast of the two components; and (iv) material connection: in other words either the high or low index material blocks, the repetitive unit, are spatially isolated [94]. A number of technologies have been proposed for PhC fabrication, but the four requirements are very difficult to satisfy simultaneously due to the limitation of each technology. Multiphoton laser processing is very promising because the lattice type, filling ratio and material connection can be arbitrarily designed from computer programs. Sufficient refractive index, at least 2.0 for diamond lattice [95] – the best lattice to achieve the full bandgap – may be accomplished by high refractive index material doping in photopolymers by using a novel mechanism like metallization.

PhCs written in currently-available transparent solids doesn't produce a sufficient contrast of refractive indexes to open a full bandgap. However, the weak bandgap effect is still interesting for PhC physics, like various nonlinear optical phenomena, and for applications that don't need a full bandgap, such as filters or attenuators. In self-organization of colloidal PhCs [96–98], microbeads are arranged in three dimensions with limited lattice type – FCC or hexagonal close packing (HCP) – and the filing ratio of beads is restricted to 74%. Note that in the optical memory work, bits that are recorded as the binary information unit were arranged layer by layer. If voxels were organized in three dimensions the same way as atoms exist in real-world crystals, the voxels would function as photonic atoms and a PhC would be formed. Photonic atoms can be configured to various lattice points, in size scaled-up from 7 systems, 32 classes, and 230 space groups of generic crystals.

The above idea has been realized inside glass with irradiation of 800-nm, 150-fs IR wavelength [31]. It was found that if the deposited energy of laser and focusing conditions were properly chosen, the voxels take the form of a well-defined near-spherical shape. A 3D FCC lattice with a lattice constant of approximately 1.0 μm has been written, from which a pronounced transmission dip that shows a bandgap effect was measured at 3490 cm^{-1}. Figure 3a illustrates the FCC lattice, (b) one fabricated layer of the FCC lattice, (111) plane, and (c) a defected PhC, a waveguide structure.

An alternative way to create microstructures is by continuously scanning the laser focal spot along a line so that a cylinder is produced [32]. If high repetition rate output is selected, the nominal spot spacing can be very small, for example, 10 nm for 1 kHz repetition rate and 10 μm/s scanning speed. Therefore interwalls between bits neighbored in the same line are partly or completely crushed and ejected by the ensuing pulse shocks. Hence a hollow cylinder is produced. The cylinders are arranged to pack

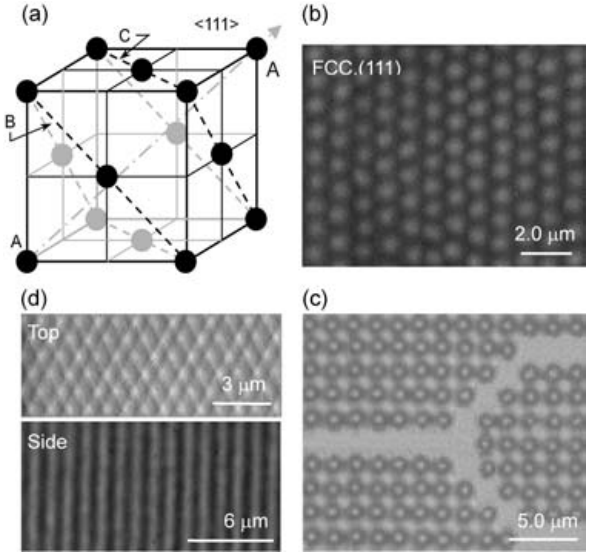

Fig. 3 Femtosecond laser written photonic crystals. **a** a schematic FCC lattice with femtosecond laser-modified material voxel as photonic atoms **b** one (111) photonic atom plane in a FCC lattice written in silica glass **c** a waveguide structure embedded in a simple cubic (SC) photonic lattice, and **d** a 2D triangular lattice photonic crystal consisting of rods continuously scanned inside silica glass

into three dimensions so that logpile-like and triangular lattices were produced. Since the cavititated dot or cylinders were producible in various material matrices, the technology can be widely utilized.

It is noteworthy that no PBG effect is visible from the as-irradiated samples in both dot- and rod-PhCs. After post-irradiation annealing, transmission dips show up, attributed to the smoothing of internal structures which reduced scattering

2.2.4 Use of Complicated Material Recipes

Light, as an energy source, can trigger photochemical reactions, which is the basis of photochemistry. Focused femtosecond laser irradiation confines these reactions into a sub-wavelength tiny volume. Localized photochemical reactions provide a diverse mechanism for fabricating microstructures besides those discussed previously.

It is already known that porous SiO_2 prepared by a sol-gel method has interconnected 3D network structure. At the wet-gel stage of the sample preparation, the internal solution may be exchanged for solutions of various compositions. Actually, the use of solvent exchange to alter the chemistry of

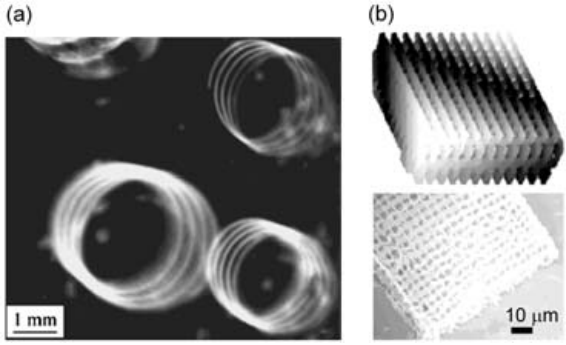

Fig. 4 Femtosecond laser written structures with a complicated material recipe. **a** A 3D spiral structure within silver-doped sol-gel materials. The latent image was produced using multiple exposures with an 800-nm, 120 fs laser. **b** Image of the actual 3D silver structure fabricated in a nanoparticle-seeded polymer nanocomposite by two-photon laser exposure; the upper image was reconstructed from a series of two-photon fluorescence microscopy images obtained at various depths in the sample and the lower SEM image of the free-standing 3D silver structure is the same as the upper one after removal of unexposed material using dichloromethane

the pore liquid is a well-developed method for using sol-gel glass as chemical sensors. Wu et al. [99] incorporated an aqueous solution of silver salt (like $AgNO_3$) into the pores of a SiO_2 matrix of approximately 20-nm diameter, and then wrote 3D structures inside the glass using a 800 nm 120 fs laser beam. Following the trace of focal spot scanning, the silver ion was photoreduced to elemental status by a multiphoton absorption process. After a final developing process that was used to enhance the structure, a 3D metallic structure was produced. Figure 4 shows the optical microscopic image of a spiral coil produced like this with a 3 mm diameter.

Experiments to date using metal ions photoreduced in a matrix have resulted only in patterns of isolated metal particles. Continuous metal structures are desired for better self-support of produced structures, and in order to provide electrical conductivity needed for microcircuits. This target was hampered because crystal nuclei of metals appear and grow into isolated particles in random sites of the irradiated volume. These particles are less easily combined into a bulk due to the limited doping concentration and due to steric resistance to particle movement. Noticing the fact that growth rates are generally much larger than nucleation rate and the former depends on the number of nucleation centers, Stellacci et al. [100] solve this issue by introducing nanoparticle seeds into the composite to be irradiated. The metal seeds are equivalent to high concentrations of ions. Metal ions would be consumed mostly by growth of the existing nanoparticles instead of producing new dispersed nuclei. The growth can be used to fill inter-seed intervals to provide continuous metal structures. Experimentally they used an organic

solvent-soluble silver salt ($AgBF_4$) as a precursor to metal atoms, and to achieve homogeneous dispersion of the nanoparticles and high optical quality film, they used ligand-coated particles to avoid aggregation. The role of the particles was proved by the fabricated results; 3D shelf models of copper and gold were produced the same way as silver (Fig. 4b).

3
Fundamentals of Stereolithography using Two-Photon Photopolymerization

Photopolymerization is one of the most important types of photochemical reactions that have been used for laser fabrication [1–5]. This is because the material resins undergo a significant phase transition after laser irradiation, from liquid to solid, and non-polymerized liquid is easily removed by a developing process so that solidified 3D structures stand out [10, 101–103]. Photopolymerized structures have real physical shape, contrasting with those image-like structures recorded in solid matrixes. Hence, not only optical components, but also micromechanical devices as well as microelectromechanical systems (MEMS) could be produced. By using two-photon-induced photopolymerization, it is possible to polymerize structures with sub-micron features, implying a more diverse use of the technology.

3.1
Two-Photon Photopolymerization

3.1.1
Photoinitiation and Photopolymerization

Photopolymerization refers to the process of using light as an energy source to induce the conversion of small unsaturated molecules in the liquid state to solid macromolecules thorough polymerization reactions. Although other radiations, including x-ray, γ-ray, microwave, and even electron and ion beams can induce similar curing reactions [4], photopolymerization deals with those that are induced by light in the UV, visible to IR spectral region. The basic components of the starting liquid material are monomers and oligomers (or prepolymer). Upon light excitation, the monomers or oligomers may be solidified by two means: polymerization and crosslinking [1–5]. An important feature of polymerization is the chain reaction by which macromolecules are created; while cross-linking is concerned more with the formation of crosslinks with chemical bonds (different from the entangling of polymer chains [19]). An important difference of these two kinds of reaction lies in their quantum yield, which is defined as the ratio of number of polymerized monomer units to the number of photons that are needed to cause

this polymerization. In the case of photocrosslinking, addition of each monomer unit requires absorption of a photon, leading to a quantum yield less than 1. In contrast, photopolymerization is realized via chain reactions as shown in the following equation (Eq. 6), so the quantum yield can reach several thousands [5].

$$M \xrightarrow{M} M_2 \xrightarrow{M} M_3 \cdots M_{n-1} \xrightarrow{M} M_n \tag{6}$$

Here M is the monomer or oligomer unit, and M_n, the macromolecule containing n monomer units.

For practical photopolymer systems, more components are included, most importantly photoinitiators and photosensitizers [1–5]. The quantum yield of general monomers and oligomers is low. In order to increase the initiating efficiency, one or several low-weight molecules that are more sensitive to light irradiation are added. They form initiating species of radicals or cations by absorbing photons. Such small molecules are called *photoinitiators*. The production of active species that attack monomers or oligomers is called *photoinitiation*, the most important step in photopolymerization. Take the radical case for example, with the following initiation step:

$$I \xrightarrow{h\nu} I^* \rightarrow R\cdot \tag{7}$$

where symbols denote photoinitiator (I), radical ($R\cdot$) and I^*, an intermediate state of the photoinitiator after absorbing a photon. Therefore the polymerization process is more precisely described by the following equation:

$$R\cdot + M \rightarrow RM\cdot \xrightarrow{M} RMM\cdot \cdots \rightarrow RM_n\cdot \tag{8}$$

The photoproduced radicals react with monomers or oligomers, producing monomer radicals, which combine with new monomers, and so on; so the monomer radicals expand in a chain reaction, until two radicals meet with each other. This chain propagation stops in either of the following channels:

$$RM_n\cdot + RM_m\cdot \rightarrow RM_{m+n}R \tag{9}$$

$$RM_n\cdot + RM_m\cdot \rightarrow RM_n + RM_m \tag{10}$$

Therefore the polymerization process consists of several steps: (i) photoinitiation (Eq. 7), (ii) chain propagation, (Eq. 8), and (iii) termination, (Eqs. 9, 10). We can see from the above description that a good photoinitiator should be (i) easily reduced to an initiating species upon light irradiation, and (ii) provide photoproduced radicals or cations active enough to react with monomers or oligomers.

In many cases, the energy collection (i) and triggering chain polymerization (ii) are cooperatively accomplished by multi-type molecules. A *photo-*

sensitizer is a molecule that absorbs light and then transfers the energy to a photoinitiator. With such a scheme, the photoinitiation process is expressed as:

$$S \xrightarrow{h\nu} S^* \cdots \xrightarrow{I} I^* \rightarrow R\cdot \tag{11}$$

where *S* is the photosensitizer. A *coinitiator* itself doesn't absorb light, but it is involved in the production of radical species.

The above descriptions of polymerization are based on radical initiators. Actually, photopolymerization reactions are basically classified into two categories: radical polymerization and ionic polymerization. Among these two types of photopolymerization, reactions that are typically used for laser fabrication are [1–5]:

(i) double-bond addition of acrylates (radical-type)

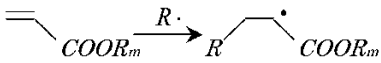

(ii) ring-opening of expoxides (cationic-type)

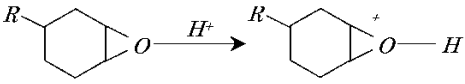

These two types of reactions require triggering by different initiators. For a radical type initiator, benzoyl is the most widely used chromophore since it exhibits good absorption in the UV region.

Although radicals may be produced by various photochemical conversion processes like photoscission, abstraction of intramolecular hydrogen, and electron and proton transfer, the most efficient radical initiators developed so far work via bond cleavage [5], for example:

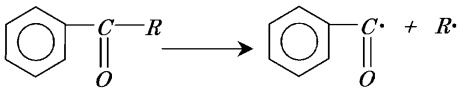

Good reviews of the synthesis, performance, and general research into various radical type photoinitiators can be found in [3, 4, 104].

Cationic photopolymerization is much less used than the radical type. The photoinitiation is generally based on the ring opening of the oxirane group [1–5]:

$$I \xrightarrow{h\nu} C^+ \tag{15}$$

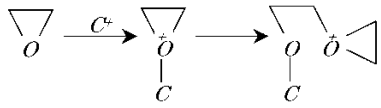

Three classes of molecules are found to be valuable for practical use here: diazonium salts, onium salts and organometallic complexes, about which detailed discussion have been published [4, 105]. Compared to radical type reactions, cationic polymerizations feature (i) low curing speed, (ii) lower viscosity, (iii) small shrinkage after polymerization, and (iv) severe post-irradiation dark polymerization. Sometimes extra thermal processing is needed to increase the conversion of monomers [106]. The above general information is instructive for choosing a suitable material system for laser fabrication.

After polymerization, the oligomer constitutes the backbone of the polymer network. The physical, chemical and mechanical properties of the solidified resin strictly depend on the nature and structure of the oligomer. Oligomers generally contain at least two reactive groups, from which both cross-linking and polymerization could occur. For example, oligomers possessing two acrylate groups may have many different backbones due to different components of R: polyester, polyurethane, polyether, epoxy, and so forth.

Monomers have a much smaller molecular weight and consist of one or several reactive groups [104–106]. They polymerize similarly to oligomers and are an important factor in determining the efficiency of polymerization. In addition, monomers are also useful for diluting resins so that the polymer is easier to handle for a particular use. For 3D micro-nanolithography, a suitable viscosity is of particular importance due to the opposite requirements in different steps of processing: a high viscosity is needed for keeping early produced volumes where they are created; while a low viscosity facilitates removal of unsolidified resin from intervals. Strictly speaking, resin is the oligomers that have a molecular weight ranging from 500 to 3000, and exhibit a viscosity of 5 to 25 Pa·s. However, to keep the convention of word usage, we call the mixture of the starting liquid as resin. In addition to the viscosity, among many, the following bahaviors are preferred for a successful fabrication: (i) high polymerization efficiency upon light irradiation, (ii) lower shrinkage after polymerization, (iii) fast reaction time and low dark polymerization.

3.1.2 Photopolymerization Induced by Two-Photon Absorption

Selection rules for single-photon and two-photon excitation (TPE) are different [42, 107, 108]; however, most resins that polymerize under UV (λ) exposure can undergo similar reactions when two photons (2λ) are absorbed simultaneously (two-photon photopolymerization), provided that the light intensity is large enough.

Electron excitations that need absorbance of two-photon energy can occur stepwise or simultaneously [33] as shown in Fig. 5a,b. The former relies

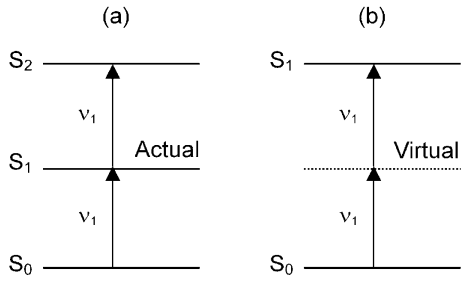

Fig. 5 Illustration of two-photon absorption schemes. **a** stepwise TPA with an actual intermediate energy level, and **b** simultaneous TPA with a virtual energy level. The former could be treated as two sequential single-photon absorption processes. For femtosecond laser micro-nanofabrication, simultaneous TPA is more relevant. All works discussed in this review are based on simultaneous TPA

on the existence of a real intermediate state, from which an excited population is further pumped to a higher energy level by absorbing photons of the same energy as the ground state (excited state absorption). Such a process, although on some occasions also called TPA, is better termed as stepwise absorption, or stepwise TPA to avoid confusion. Compared to simultaneous TPA, stepwise TPA doesn't require coherence of the incident light, and may be considered as two sequential single photon absorptions. The excitation efficiency can be high enough to provide intense up-conversion fluorescence, which is one of the important mechanisms of IR sensor cards.

Simultaneous TPA, most generally referred to TPA, is a quantum mechanical three-body process, where an electron absorbs two photons simultaneously to transcend the energy gap in one excitation event [42, 43]. An intuitive physical scenario is, as light passes through a molecule, a virtual state is formed when the first photon is absorbed. It persists for a very short duration (of the order of several femtoseconds as prescribed by Heisenberg's Uncertainty Principle), which contrasts with the long lifetime of the actual intermediate energy level in stepwise absorption. TPA can result if the second photon arrives before the decay of this virtual state. If the energy of the two photons are identical, the process is referred as *degenerate TPA*, otherwise, the process is a non-degenerate one. TPA was theoretically predicted as early as 1931 [50] and was experimentally observed for the first time in 1961 [51]. For a long time, a practical use for it was not known except as a spectroscopic tool for determining the positions of energy levels that are not connected to the ground state by single photon absorption [108, 109].

TPA can be utilized for inducing photopolymerization. The difference between one-photon [101–103] and two-photon induced photopolymerization lies in how the energy for activating initiators is provided. In the case of TPA photopolymerization, initiators are excited to triplet states by absorb-

ing combined two-photon energy,so correspondingly Eqs. 7 and 11 should be re-written as:

$$I \xrightarrow{2\hbar\nu'} I^* \rightarrow R\cdot \tag{17}$$

$$S \xrightarrow{2\hbar\nu'} S^* \cdots \xrightarrow{I} I^* \rightarrow R\cdot \tag{18}$$

where $\nu' \sim \nu/2$ denotes photon frequency in the two-photon excitation beam. From our experience, resins that have been developed to polymerize at UV or visible wavelengths, ca. λ, were generally polymerizable under 2λ irradiation only if the photon flux density is sufficiently large. However, the usability, TPA efficiency, thresholds of polymerization and laser-induced breakdown, tolerance to exposure dose variation, and so on depend on the natures of the specific materials.

Two-photon photopolymerization was experimentally reported for the first time in 1965 by Pao and Rentzepis [110] as the first example of multiphoton excitation-induced photochemical reactions. They focused 694-nm laser from a pulsed Ruby laser into a sample of styrene that was cooled to 77 K. After developing in methanol, solid precipitate was extracted and confirmed to be polystyrene through IR absorption. In the particular experiment, no photosensitizer was used and the author tried to increase the two-photon absorbance by using monomers with added functional groups, such as para-isopropylstyrene and chlorine-substituted derivatives of styrene. As a result, much enhanced two-photon polymerization was observed. After this work, although there were some ensuing researches that were scattered among the literature [111–113] , no particular efforts were devoted to two-photon photopolymerization until this technology found value as a microfabrication tool.

3.1.3 High Efficiency Two-Photon Materials

Molecules of large TPA cross-section [21–25, 114–116] are very important for the broad application of two-photon photopolymerization technology. They would enable the use of inexpensive CW laser or nanosecond lasers, or multi-beam simultaneous polymerization for batch production by beam splitting. Also, the large TPA cross-section would open up a large dynamic power range for tailoring microstructure dimensions by power control. Polar molecules were found to have a large change of dipole moment ($\Delta\mu$>10D) upon excitation from ground state to excited state [24, 117]. Since both the ground and excited state can participate in the formation of the virtual energy level, the transition probability is proportional to $(\Delta\mu)^4$ [24]. Correspondingly, the TPA cross-section can be larger than $\delta \sim 100\times10^{-50}$cm ^{4}s photon^{-1}.

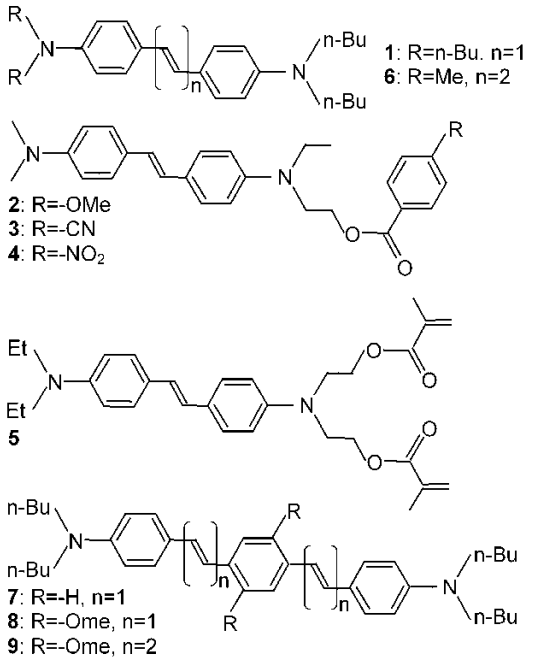

Fig. 6 Molecular structures of high-efficiency two-photon photochromophores

One important effort in the molecular design of large δ is searching for a molecular structure that potentially has larger $\Delta\mu$. It was found that π-conjugated systems such as those with phenylethenyl [21], fluorenyl [117], or polyenyl constructs [118] were good candidates. In these molecules, electron-donating (D) and/or electron-withdrawing (A) moieties were separated by a conjugated π-electron system (A-π-A, D-π-D, D-π–A–π-D and A-π-D-π-A). These chromophores function on the basis of symmetric charge transfer, from the ends of a conjugated system to the middle or vice versa. It is theoretically predicated and experimentally found [22] that δ can be enhanced by increasing the conjugation length and the donor and acceptor strengths. Efficient electron transfer from excited 4,4'-bis(*N*,*N*-di-n-butylamino)-E-stilbene (**1**, Fig. 6) was confirmed by a large biomolecular quenching rate and by reduction of fluorescence lifetime in covalently-linked chromophore-acceptor systems wherein one or more of the amine-bound alkyl groups of **1** was replaced with an electron acceptor (**2**–**5**, Fig. 6). The radicals produced by electron transfer from photoexcited **1** to an acrylate or subsequent radical products were found to initiate the polymerization of the acrylate with a much higher efficiency; for example, photopolymerization of a commercial resin SR9008 initiated by **1** and **6** has a threshold 30% that of most conventional sensitive UV initiators. In a further experi-

ment, Marder et al. demonstrated for the above systems that δ was increased by extending the conjugation length (**7–9**, Fig. 6). δ as high as ~1250×10^{-50}cm^{4}s photon^{-1} was obtained from **9**. These initiators were successfully utilized for 3D microfabrication [22].

Another concern in two-photon molecule design is wavelength sensitivity [117, 119]. This arises from the fact that the most suitable femtosecond laser is solid wavelength-tunable Ti:Sapphire laser, of which the wavelength ranges from 680 ~ 840 nm (extendable to around 1 μm but subject to a low output power). Belfield et al. [24, 117, 119, 120] synthesized a series of fluorene derivatives with varying electronic characteristics. The UV-visible absorption peaks at the ideal wavelength of near 400 nm, and some of them possess δ~1300×10^{-50}cm^{4}s photon^{-1}.

In addition to increasing TPA cross-section of chromophores, there is another route to enhancing TPA: by increasing the chromophore number density without causing aggregation. Dendrimers functionalized with TPA chromophores at their periphery have been explored [121, 122]. It is found [123] that by attaching a soluble two-photon absorbing chromophore with a functional group to a dendritic backbone, the molecular TPA cross-sections could be doubled from one dendrimer generation to next. The dendrimers were chosen as highly soluble in common organic solvents. The linear correlation between the end chromophore number and TPA cross-section implies that neither cooperative nor deleterious effects due to the high local chromophore concentration occur.

3.2 Microfabrication Systems

3.2.1 Design Consideration of Optical Systems

The current laser micro-nanofabrication systems stem from the conventional laser prototyping method [6]. Figure 7a illustrates its concept, and for reference, three other layered manufacturing technologies are also shown (Fig. 7b–d) [6].

Laser rapid prototyping [6–9] involves the formation of a 3D object additively, in a layer-by-layer way. It couples the power of computer designs, through laser-initiated photopolymerization, to the formation of a unique, real plastic form. Figure 8 illustrates a practical prototyping system. In fabrication, 3D CAD patterns were first extracted into a series of two-dimensional (2D) slices corresponding to profiles at different height levels (Fig. 7a). Starting from the first layer, the lateral dimension is controlled by scanning a laser beam over the surface of the polymer film at a rate sufficiently low to form a gelled layer of polymer with desired and fixed depth. After the formation of the first layer that was affixed to the substrate, a new

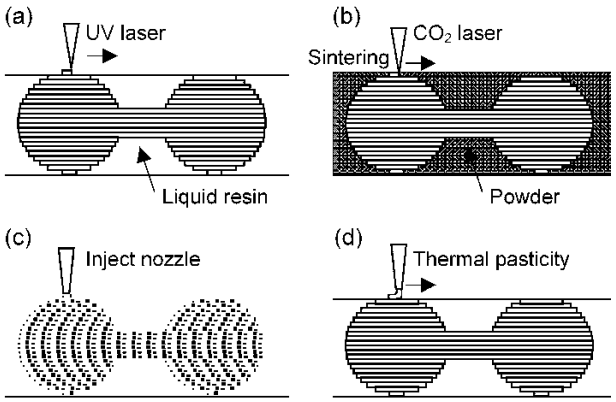

Fig. 7 Illustration of several types of layered manufacturing technologies. **a** Laser rapid prototyping using photopolymerizable resin, **b** powder sintering, **c** ink injecting and writing and **d** resin squeezing and writing

thin layer of polymer was added by casting (Fig. 8a), by immersing the platform (Fig. 8b), or by releasing the liquid surface (Fig. 8c) and then solidifying. This process is continued in an additive modeling fashion until the desired object is formed [6].

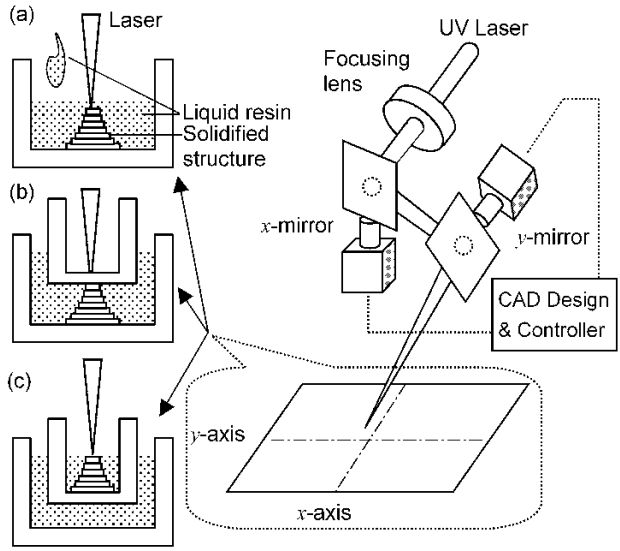

Fig. 8 A laser rapid prototyping system. The writing could be accomplished either by mirror angle scanning or by moving sample stages. The former mechanism is shown here. Three major approaches were utilized to control the longitudinal resolution, **a** film casting, **b** surface regulation, and **c** open surface methods

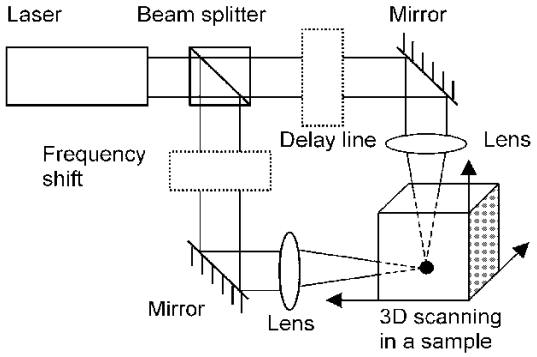

Fig. 9 A crossbeam two-photon two-color scanning laser microscopic system. Pulses from two beams split from an identical laser output should overlap in both time and temporal domains so that a TPA process could be launched by simultaneously absorbing two photons. Removal of the frequency shifter gives rise to a degenerative two-photon fabrication system

In the above system, patterning in the two horizontal dimensions is realized from a series of CAD slices, and the longitudinal spatial resolution is controlled by the thickness of newly-added resin film. There are two disadvantages that hinder applying the mechanism for micro-nanosize fabrication. First, it would be difficult to form film of thickness 1 μm or less due to the viscosity and surface tension of the resin, and second the layer-by-layer scanning method sometimes restricts the achievable geometry.

To solve this problem, Maruo et al. [10] proposed a two-photon laser rapid prototyping technology, now known as *two-photon photopolymerization*. In this scheme the laser was directly focused inside a liquid resin droplet and it polymerized the focal point volume by TPA. This technology firstly eliminates the requirement of thin additive liquid film and controls the longitudinal spatial resolution by focal spot size itself, and secondly, it provides the capability of writing arbitrary 3D patterns within the droplet volume, as can be done in 3D laser writing in solid matrix only if the resin viscosity is reasonably high. From this sense, the laser focus functions as a real 3D laser pen.

For two-photon excitation, crossbeam geometry was originally considered [11, 124] as shown in Fig. 9. Actually in the first proposal on 3D optical memory by Parthenopoulos and Rentzepis, the crossbeam two-color two-photon excitation was employed [11]. The system is difficult to handle in arranging optical components and in synchronizing laser pulses in the time domain, although it may be possible to reach a relatively better longitudinal spatial resolution. Afterwards, Denk et al. [12] applied two-photon excitation to laser scanning microscopes. They tightly focused a laser beam with a single lens to start degenerate TPA, by which high quality living cell images

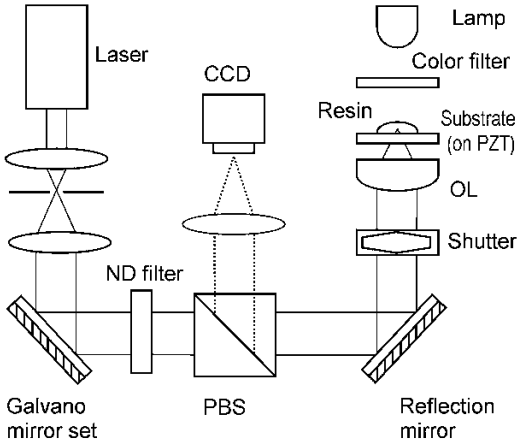

Fig. 10 Two-photon direct writing laser microfabrication system. The Galvano mirror set is used for scanning the laser beam in the two horizontal dimensions, and along the longitudinal direction a PZT stage is used. The laser power was continuously adjusted by a neutral density (ND) filter. The polarization beam splitter (PBS) lets the laser beam pass but reflects the illumination light to the CCD monitor for in-situ monitoring of the fabrication process. OL: objective lens

were obtained. This configuration was widespread due to its simplicity and has been taken as the standard for two-photon fluorescence microscopy. Now most two-photon photopolymerization systems take the form of a laser scanning microscope with enhanced 3D scanning capability.

Figure 10 shows a typical setup of a two-photon photopolymerization CAD-CAM system. It consists of three parts, fulfilling functions of (i) CAD and scanning control, (ii) laser output and beam control, (iii) two-photon exposure and in-situ monitoring.

Laser beam focusing, realized by a microscopic objective lens, is of primary importance to the entire fabrication system. Large magnification is advantageous for in-situ monitoring of the fabrication process. Comparatively speaking, a high resolution is more meaningful to fabrication. The resolution of a given objective is governed by the laser wavelength and its numerical aperture, NA [125, 126]. Shorter wavelength will proportionally reduce the diffraction-limit focal spot size. In addition, TPA efficiency is generally large at short wavelengths. For example, it has been experimentally found [127] that the two-photon photopolymerization threshold of a commercially-available resin was decreased from 3.2 TW/cm^2 (800 nm) to around 0.6 TW/cm^2 (660 nm). However, the use of short wavelength is limited by the availability of laser source and attention should be paid to avoid resin degrading due to monomer or oligomer bond cleavage. *NA* is an expression related to the maximum angle that light rays are collected from the object

plane (for imaging) or the maximum angle that a laser is converged onto the focal spot (for excitation). For example, the 1.4-NA oil-immersion (n~1.512) objective lens has a beam convergence angle of 67.2 °. In 3D fabrication, the size of excited volume, *voxel*, depends on $1/(\mathrm{NA})^4$. Therefore choosing large NA optics is essential for realizing a high fabrication resolution.

In imaging optics, the lens aberration is an important issue to address [125, 126]. Among basic aberrations, coma, astigmatism, curvature of field and distortion influence off-axis points. Therefore they don't take effect in the sample stage scanning system, but restrict the scanning range in the mirror-scanning configuration. The other two kinds of aberration, spherical and chromatic, affect the whole field. In a bandwidth-limited laser system, the shorter the laser pulse, the wider the spectrum. The *chromatic effect* (focal length changes versus wavelength) is well corrected with modern apochromatics to a negligible level. *Spherical aberration* (light rays passing through objective lens from different radial zone is focused at different depths) is a serious problem in high-NA objective lenses. This problem was partly solved: (i) many dry lenses were already corrected by considering beam focusing through a coverslip of a certain thickness; (ii) oil immersion is generally adopted in high NA lens design to improve the optical homogeneity between objective front and the coverslip. However, in both cases, if a laser is focused deep (for example, >20 μm) into samples having refractive indexes significantly different from the cover glass (for example, Δn>0.1), measures should be taken to reduce spherical aberration. Recently Sun et al. (results to be published) solved this problem by using a deformable mirror to pre-compensate the aberration.

After the laser focal spot is focused into resin, it should be scanned relative to the sample. This is accomplished using two possible means: (i) along horizontal dimensions by beam scanning by Galvano mirror, plus vertical sample or objective lens movement by lead zirconate titanate (PZT) piezoelectronic stage [13, 14, 18–20] and (ii) sample movement in all three dimensions by PZT [15–17, 101]. The former features high scanning speed because there is no need to reserve time for stage stabilization, but the scanning range is limited by spherical aberration, (to e.g. ~ 20-μm lateral dimensions for general 1.4-NA objectives). In the 3D PZT scheme, the object dimensions are determined by the scanning range of stage to hundreds of microns (range decreases if higher accuracy is needed). In both cases, the vertical dimension is restricted by the working distance of the objective lens, for example to 100~200 μm in a general 1.4-NA oil-immersion objective lens. All-PZT configuration has the shortcoming that a residing time has to be reserved between individual voxel's exposure for stage stabilizing, which can occupy a large percentage of working time, for instance 50% in the case of 1 ms exposure and 1 ms residing.

3.2.2
A Comparison with Other Microfabrication Technologies

It is projected that miniaturization [128], particularly MEMS [129], will bring a societal revolution, so development of new manufacturing technologies has attracted intense research efforts.

3.2.2.1
Photolithography

In addition to its indispensable role in microelectronics and optoelectronics, photolithography has been widely utilized for versatile fields including MEMS, micro sensors and actuators, micro-chemical reactions and analytical systems, and micro-optical systems [128, 129]. Currently UV lithography has feature sizes down to 250 nm, and it is expected to be reduced to ~100 nm in the near future by use of a combination of deep UV light (for example 193 nm ArF excimer laser or 157 nm F_2 excimer laser) and improved photoresists.

To push the resolution of conventional lithography into the sub-100 nm regime, new irradiation sources with short wavelengths have been utilized, including: XUV lithography, soft X-ray lithography, e-beam writing, atom beams, focused ion beam (FIB) writing, and proximal-probe lithography [128-131]. Better resolution, up to several nanometers has been achieved by some of these technologies. However, substantial efforts are needed to improve the development of reflective optics and/or new types of masks, and arrays of beams. In addition, all of these systems need to operate in vacuum, which causes high costs, difficult maintenance, and low fabrication efficiency.

3.2.2.2
Soft Lithography

Soft lithography [132, 133], including microcontact printing (μCP) [134], embossing [135], microtransfer molding [136], cast molding [137], injection molding [138], and replica molding [139], have a common feature. They all use elastomer, typically PDMS or thiol, patterned from a master plate created by lithography, as the stamp, mold, or mask to generate micropatterns and microstructures. This technology circumvents the limit of optical diffraction and achieves resolution up to 20 nm [132, 133]. Different from lithography, that is intrinsically suitable for use on planar structures, soft lithography can be feasibly used to produce surface structures of different heights (2.5 dimensions).

3.2.2.3 Two-Photon Photopolymerization

Compared with the above micro-nanofabrication schemes, two-photon photopolymerization has unique merits:

- First of all, it has intrinsic ability to produce 3D structures. In addition, the long wavelength chosen for TPA has less absorption and less scattering, which gives rise to the deep penetration of light; use of ultrashort pulses can start intense nonlinear processes at relatively low average power, without thermally damaging the samples.
- The two-photon photopolymerization system resembles a laser scanning microscope, which doesn't need vacuum condition for operation. The system is easy to operate and maintain.
- No mask, mold, or stamp is needed for fabrication. It directly converts computer-designed patterns into matter structure. The rapid turnaround time for fabrication allows one to quickly iterate and modify design.

3.3 Early Works in Microfabrication

3.3.1 Initial Proposals

The first reported real 3D microstructure [10] is a 7 μm-diameter and 50 μm-long spiral coil with a line cross-section of 1.3 μm×2.2 μm (Fig. 11). Due to the use of a relatively low NA (0.85) objective, the feature size is larger than the potential limit provided by the technology. However, it confirmed the feasibility of two-photon photopolymerization in three dimen-

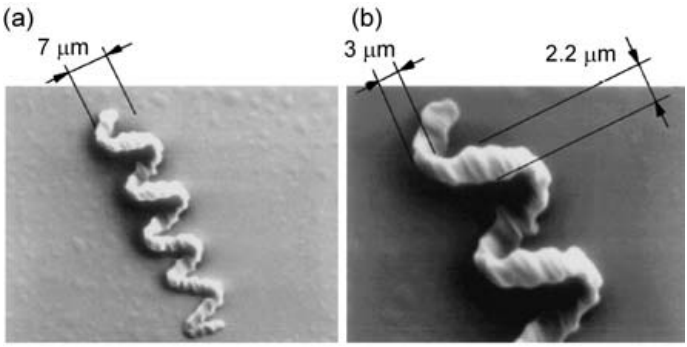

Fig. 11 Scanning electron microscopic (SEM) image of a spiral coil structure made by two-photon photopolymerization after removal of unsolidified resin. **a** A view of the entire structure and **b** the manified top end

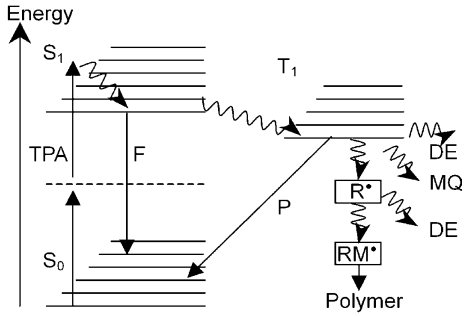

Fig. 12 Energy diagram for two-photon excitation and processes occurring in the excited states. Valence electrons of an initiator are excited from the ground (S_0) to the first excited (S_1) singlet state by simultaneously absorbing two photons. The excited electrons then relax by transition to the triplet state (T_1) via intersystem crossing, where the initiator is liable to undergo bond cleavages, producing radicals for photopolymerization. The excited states can also be relaxed by radiative processes: fluorescence emission from singlet states (F) or phosphorescence emission from triplet states (P). Both the triplet state and photoproduced radicals can be deactivated (DE), for example by monomer quenching (MQ) for the former, and by radical quenching (RQ) for the latter. Efficient photopolymerization generally needs these competing processes (F, P, DE) minimized but there are a few cases, for instance RQ, which find use for it in reducing voxel sizes. The dashed line denotes a virtual energy level for TPA

sions. In this experiment, a 790 nm, 200 fs laser was focused into SCR 500 [Japan Synthesis Rubber Company, JSR], a commercial urethane acrylate resin that is often used in the group.

Figure 12 shows the scheme of TPA and processes occurring in the excited states. Due to a long excited-state lifetime, the triplet state (where the sum of electronic spin in a molecule is $2s+1=3$, where $s=\pm 1/2$ is the quantum number of the electronic spin) is the major transient state that is responsible for the generation of radicals.

The carbonyl group contained in the initiators that were used, a mixture of benzoyl cyclohexanol and morpholino phenyl amino ketones (inset of Fig. 13a), exhibits two kinds of triplet states: $\pi\pi^*$ and $n\pi^*$. However, according to selection rules of electronic transition, $n\rightarrow\pi^*$ transitions are symmetry forbidden and $\pi\rightarrow\pi^*$ transition are symmetry allowed. Therefore the molar extinction coefficient of the $n\rightarrow\pi^*$ transition is much smaller than that of the $\pi\rightarrow\pi^*$ transition. Figure 13a shows the absorption spectrum of the resin, which consists of urethane acrylate oligomers with different molecular weights (480 and 1200), urethane acrylate monomer as a dilutor, and the initiators mentioned above.

Actually, in earlier research, Wu et al. [140] already proposed exposing thick photoresist film using TPA by substituting UV light with lasers of longer wavelength, and scanning the laser focal spot in three dimensions in-

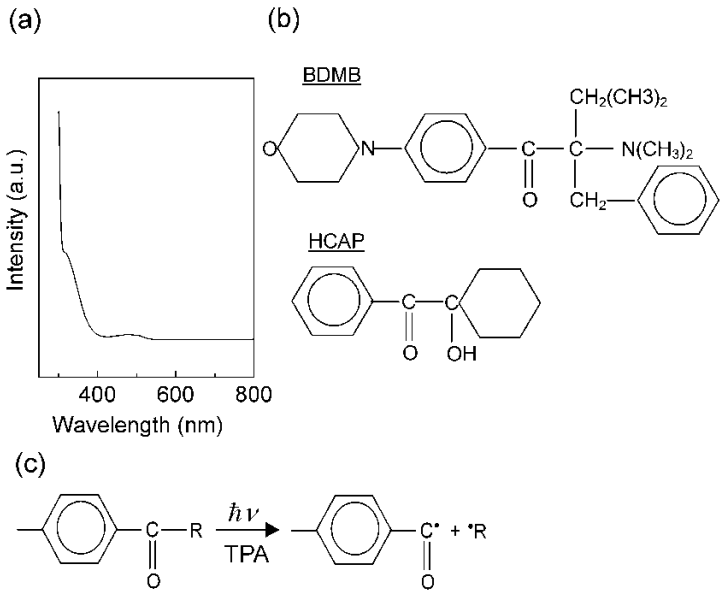

Fig. 13 **a** Absorption spectrum of SCR 500 resin, which was major precursor material for two-photon photopolymerization in the work of Sun et al. [13, 14, 18–20] **b** Molecular structures of two kinds of benzoyl initiators: BDMM and HCPA. **c** Typical reaction of radical production via an α-cleavage process. Radicals are produced in HCAP entirely by, and in BDMB mostly by, this mechanism. Note negligible single photon absorption at the working wavelength of 780 nm

stead of illuminating a photomask with parallel beam. Experimentally the photoresist was spin-coated on a cover glass to form a 3~4 μm film and then baked at about 80 °C. After 3D scanning with 100 fs, 620 nm laser light, a trench structure with an aspect ratio of eight and trenches with undercut profile (for example 0.3 μm at the top and 0.8 μm at the bottom) were obtained. Although this research was different from laser prototyping due to the use of conventional solid film, it is already quite similar to the current two-photon polymerization technology.

3.3.2 Evidence of the Two-Photon Process

The absorption of UV curable resin due to valence electron transition is situated in the UV or the blue side of the visible. Generally it is safe to attribute polymerization reactions, when exposed to IR, to a two-photon process from the transmission or absorption spectra of the starting materials. However, it is still helpful to obtain direct evidence of the occurrence of TPA. A simple test could be conducted using a general mode-locked femtosecond

laser. Linear exposure needs a certain photon flux, D_{th} (photon/cm^2), expressed by the product of irradiation duration (Δt) and photon flux intensity (photon/s cm^2) that is proportional to light intensity (W/cm^2). D_{th} is reachable either by intense irradiation for short time or weak irradiation for long time. However, experimentally there is no polymerization observed when lasers work in CW mode, where the power is uniformly delivered over time [141]. On the other hand, polymerization occurs with the same irradiation dose under pulsed mode. When switched to pulsed mode, a 82 MHz, 100 fs and 1 mW mean power at diffraction limit focal spot has a photon flux density of 10^{29} photons/s cm^2 in the pulse duration, 1.2×10^5 times larger than that in CW mode. Since single-photon polymerization relies only on photon flux, while both photon flux and photon flux density are critical for two-photon photopolymerization, the above simple test provides solid proof of the TPA process.

Wu et al. [142] studied two-photon exposure using photographic films based on silver halides. An 800 nm, 120 fs laser was slightly focused with the waist crossing the film. By extrapolating the polymerization thresholds at 350 nm (2.8×10^{-6} J/cm^2) and at 470 nm (3.8×10^{-4} J/cm^2) to 800 nm, it is predicted that the single photon exposure at 800 nm needs 10^9 J/cm^2. This value is larger than the actually used value (~ 0.4 J/cm^2) by many orders, excluding the possibility of single-photon process at 800 nm wavelength. In further experiments, it was observed that the photon flux that was needed to induce a diffraction-limit spot using 120 fs pulses was four times smaller that needed by 240 fs pulse. This result, consistent with the CW/mode-lock polymerization test, supports the theory that the excitation is by a two-photon process.

3.3.3 Pulse Energy Issues, Laser Oscillator and Regenerative Amplification

The immergence of two-photon photopolymerization is a direct outcome of the progress of laser technology. For example, pulse regeneration technology can increase energy of single pulses by more than four orders of magnitude, by which polymerization thresholds of almost any kinds of resin become accessible. Take Spectra Physics Ti:Sapphire laser amplifier (Spitfire) as an example. The single pulse energy of a 80 MHz, 1 W average input power laser beam is 12.5 nJ, while after regenerating amplification, the repetition rate become 1 KHz with the average power unchanged, giving rising to a single pulse energy of 1 mJ. Increase of single photon energy multiplies photon flux density by the same order (>10^4), and TPA probability is squared (10^8). With such huge single pulse energy, almost any UV curable resins can be polymerized by TPA. That is a major advantage of the pulse regenerative amplification system.

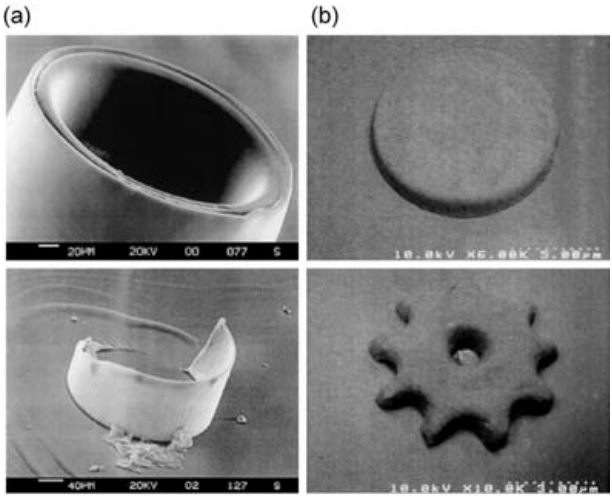

Fig. 14 Microstructures produced using regeneratively magnified laser pulses, where voxels are created by single-shot pulse irradiation. **a** a tube (top) and a spiral tube (bottom), showing the large longitudinal fabrication resolution in the case of low-NA focusing (25-mm focal length), and **b** a micro-disk (top) and a micro-gearwheel (bottom)

The difference in laser pulse energy slightly influences the fabrication processes. First, the average power needed to induce photopolymerization is much smaller for a pulse-amplified beam than for an oscillator beam. Second, large pulse energy enables formation of voxels by single pulses. Witzgall et al. [127] used SU-8, developed for high aspect ratio MEMS fabrication. 4-μm diameter and 80 μm height voxels were created by focusing with a lens of 25-mm focal length (very low NA). Consecutive single-shot laser irradiation produced a spiral structure by fast axial translation and simultaneous sample rotation (Fig. 14a). Also by single shot laser irradiation enabled by pulse regeneration, Sun et al. [15–17] fabricated various micromechanical and PhC structures; as an example, a micro gearwheel is shown in Fig. 14b.

If the photopolymerization threshold could be reached, a voxel could be produced either by exposing an 82 MHz pulse for 1 ms, that is 82,000 shots, or by 1 kHz single-shot (1 shot/ms) irradiation. Therefore, the fabrication speed is not much increased by use of currently available regeneration systems. Another point that should be mentioned is that in this review we don't compare laser power or laser pulse energies that were reported from different groups and different works because of a lack of a standard method to precisely measure the focal spot power, particularly when the laser is tightly focused. The difficulty arises from the fact that the average power at a focal spot is generally small (hundreds of nanowatts) and quite divergent (67.2 ° for 1.4 NA). Calculation from lens transmission is less accurate because the power loss in objective lenses arises largely from the rejection at the en-

trance pinhole and the pinhole used to tune NA, and therefore the net output power is related to the incident beam shape and size.

3.3.4 Dynamic Power Range

The polymerized voxel size increases with the increase of the irradiation duration (Δt) and the square of light intensity, SLI, (I^2), implying the possibility of tuning voxel dimensions by controlling Δt and I. However, the tuning range or *dynamic power range* is defined by the window between the two-photon polymerization threshold and the laser-induced breakdown threshold [49]. This range is quite small for general resins, several times the polymerization threshold [16, 127], leaving little room for power tuning.

The photopolymerization threshold is determined by the production efficiency of initiating species from excited triplet states, which is characterized by the quantum yield of polymerization. The reactions that produce radicals should compete with monomer quenching, oxygen quenching and other pathways of deactivation of the excited states like phosphorescence emission. The threshold is also determined by the reactivity of radicals and monomers.

When laser irradiation is greater than a particular value, intense damage is induced in materials. This phenomenon is called *laser-induced breakdown*. The breakdown is dominated by a thermal process when pulse width is long (e.g. >10 ps for most transparent materials [49, 143]). This was evidenced by observations that the breakdown threshold scales approximately with pulsewidth by $\tau^{1/2}$ for τ >10 ps [143, 144]. For shorter wavelength (<1 ps), it is believed that the breakdown occurs in various materials via plasma generation [145]. Plasma can be produced via an avalanche process whereby free electrons are accelerated by the incident light field, causing an explosive cascade growth in electron density. The generated plasma can, in turn, absorb and defocus the remaining incident light field. The breakdown causes the ablation process at sample surface and micro-explosion inside bulk, both accompanied by vaporization and atomization of the sample constituents. Laser induced breakdown spectroscopy is a useful tool for semi-quantitative elemental analysis of surface components in completely unknown samples. However, it is detrimental to photopolymerization because breakdown-induced resin bubbling damages existing structures and prevents further reactions.

The laser-induced breakdown is not necessarily related to the multiphoton absorption process [145] while photopolymerization depends on it strictly [24, 25]. Therefore, measures could be taken to increase the quantum yield of polymerization, and therefore the dynamic power range. A simple and effective method is choosing laser wavelength so that radicals are produced more efficiently. It was experimentally observed [127] that the two-

photon exposure threshold at 660 nm is roughly half of that at 700 nm, and approximately five times lower than that at 800 nm, while the breakdown threshold didn't vary significantly. The most efficient method is use of high TPA cross-section initiators. By using photoinitiator 8 in Fig. 6, the dynamic power range of radical initiated polymerization of acrylate resin reached 50 [22]; and by using an isopropylthioxanthone/diarylidonium salt initiating system, the polymerization of epoxides was increased to more than 100 [146]. With such a large dynamic power range, the voxel size could be tailored by almost two orders.

3.3.5 Viscosity of Resins

In two-photon polymerization scanning should start from the substrate surface so that polymerized structures can be fixed. If the structure/substrate contact area is small, the adhesion may not be strong enough against post-fabrication washing. This issue was largely alleviated by pre-casting a thin layer of resin to be used, and then fully polymerizing it by single photon or thermal processes, since the polymer-polymer adhesion is better than that from polymer-glass connection. During the course of fabrication of real 3D structures, earlier-produced structures may move from where they were created, or even float away due to the flow of resin itself caused by resin spreading on the substrate surface or by ambient vibration. This is an intrinsic shortcoming of using liquid droplets.

This problem was solved by choosing resins of relatively high viscosity [1–5], which offer a clamp function to the isolated components that were temporarily not yet connected to the main body. The high viscosity is attainable by reducing the concentration of monomers in the resin. For some commercial resins with ready ingredients, it was found effective to use a pre-polymerization method [16]. That is, partly exposing the resin via single-photon absorption before TPA fabrication to induce short-chain photopolymerization, which equivalently increased the viscosity of resins. Since photons can't penetrate the surface to a significant depth, a strenuous stirring of resist was utilized to afford better uniformity.

To test this idea, Sun et al. [16] pre-exposed NOA-800 (Norland Products Inc.) resin under a 150 W xenon lamp for 60 seconds with a quick stirring. With this partly exposed resin, they fabricated a micro-gearwheel affixed to a shaft (Fig. 15). First the shaft on the hemispherical base was constructed, and then the gearwheel was co-axially polymerized at a level of the top end of the shaft. Due to the high viscosity of resin, the gearwheel didn't move even if it was not connected to any part of the shaft that was adhered to the substrate surface. The gearwheel gradually fell in an in-situ developing, and was finally trapped by the axle.

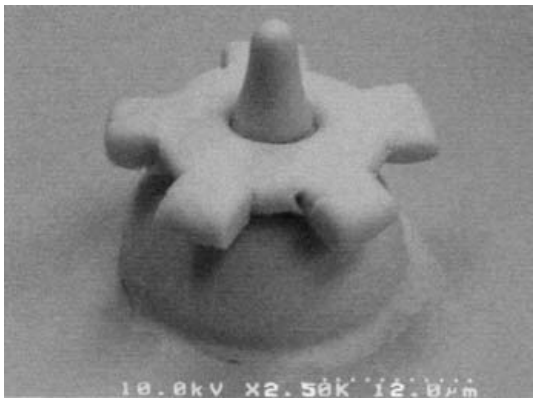

Fig. 15 SEM image of a real 3D device, a microgear wheel affixed to a shaft, which was produced using the pre-photopolymerized resin to increase its viscosity. The gearwheel was observed to be rotatable during the developing process

3.3.6 Two-Photon Fluorescence-Induced Photopolymerization

Novel polymer systems with much enhanced TPA initiators have been synthesized. However, it is still attractive to use well-known systems that were developed for conventional UV polymerization due to their excellent chemical, physical, and mechanical properties. Initiators in these resins generally have small TPA cross-sections, which require very high laser pulse energy for two-photon use. A strategy for circumventing this situation is to induce photopolymerization not by direct TPA of initiators, but by TPA-induced up-conversion fluorescence. An efficient fluorophore that emits at blue or shorter wavelengths was doped into resin. By TPA, the excited fluorescence polymerizes the resin by a single photon process. Since the fluorescence was three-dimensionally confined at the focal spot, the polymerization was also restrained to occur at this volume.

This technology uses well-developed UV polymers and takes advantage of TPA. Joshi et al. [147] applied this method to NOA 72 resin, a well-known urethane acrylate oligomer that was cured by absorption light of 315~450 nm. The resin was doped with AF183 dye by 2 wt%. The fluorophore AF183 has a very strong TPA at near IR, and emits blue up-converted fluorescence peaking at ~465 nm, with the blue side covering the absorption of NOA 72. By exciting an 800 nm, 100 fs laser, they wrote a splitter-type channel waveguide (Fig. 16), and succeeded in coupling a He-Ne laser into the waveguide. Similar experiments [148] were conducted using AF 380 dye doped NOA 72, producing two-beam interfered gratings.

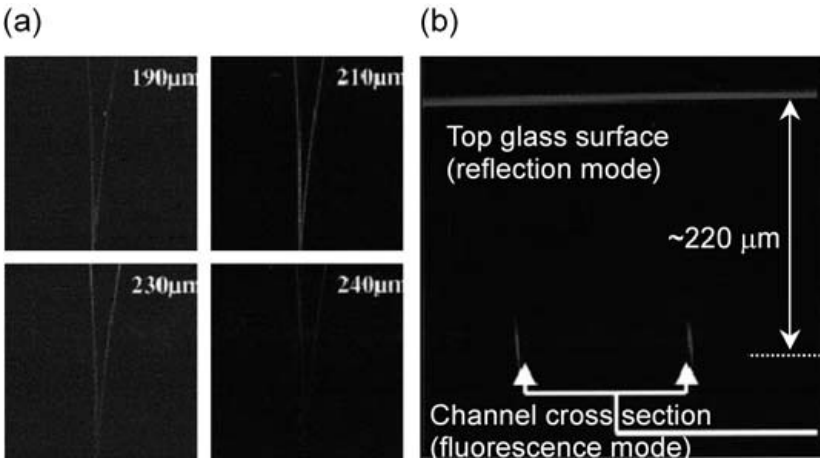

Fig. 16 **a** Different confocal images of a splitter-type channel waveguide polymerized inside a polymer gel by two-photon-induced up-conversion fluorescence. **b** Vertical cross-section of the channel waveguide imaged using both the fluorescence and reflection modes in a confocal microscope

3.3.7 Cationic Photoinitiated Polymerization

Although less used, cationic photoinitiated polymerization of epoxides have some merits in microfabrication [1–5, 104–106]: for example, less shrinkage after polymerization, which may facilitate high fidelity 3D writing; low viscosity, which is important for developing complicated internal structures; and high stiffness. These resins may be useful in fabricating 3D PhCs which have sufficient self-supporting due to the 3D periodicity but impose high requirements in washing away unsolidified liquid monomers and oligomers.

Commercially-available diaryliodonium (CD-1012, Sartomer) and triarylsulfonium (CD-1010, Sartomer) salts were found to initiate polymerization of multifunctional epoxide and vinyl ether monomers [24]. Figure 17a shows a line structure achieved by polymerization of a mixture of poly(bisphenol A-co-epichlorohydrin) glycidyl end-capped and 3,4-epoxycyclohexylmethyl 3,4-epoxylcyclohexanecarboxylate (K126, Sartomer) initiated by CD-1012. To check the potential spatial resolution, we focused the laser using high-NA optics to polymerize commercial resin SCR701 (JSR) and a lateral spatial resolution of 100 nm was obtained (Fig. 17b).

The refractive index increases with the increase of degree of photopolymerization. Therefore a monitoring light beam passing through the center of a voxel would undergo a phase shift relative to that through the periphery of the voxel due to the high central light intensity in a Gaussian field. Interference patterns formed due to different portions of the monitoring beam

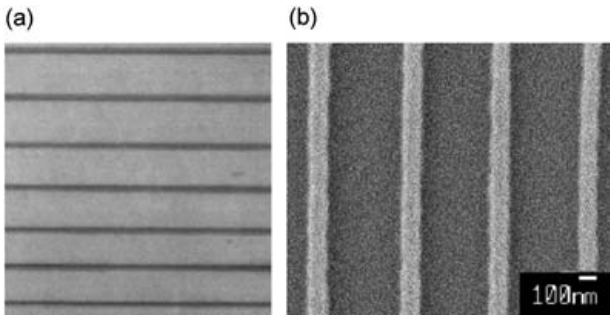

Fig. 17 Line structures produced by cationic photoinitiated polymerization. **a** by polymerization of a mixture of poly(bisphenol A-co-epichlorohydrin) glycidyl end-capped and 3,4-epoxycyclohexylmethyl 3,4-epoxylcyclohexanecarboxylate (K126, Sartomer) initiated by CD-1012, and **b** by commercial resin SCR 701. Note the 100-nm lateral spatial resolution in (b)

would vary with the progress of polymerization [146]. This effect was implemented for studying the polymerization threshold (I_{th}), the polymerization rate (R) and its dependence on various parameters of the optical system and resin components. By using this technology. Boiko et al. [146] found that R of an isopropylthioxanthone/diarylidonium salt initiated epoxide polymerization is proportional to $m = 1.7$ power of the intensity:

$$R = [\mathrm{C}(I - I_{\mathrm{th}})]^m \tag{19}$$

where C is a constant and I the light intensity. This is different from radical polymerization, where the dependence is much more complicated. The difference is possibly related to the different termination mechanism in the two types of polymerizations.

4 Advanced Techniques in Two-Photon Micro-Nanofabrication

The progress of femtosecond laser technology and exploration of high efficiency photoinitiators and photosensitizers have fueled the progress of two-photon polymerization lithography. Its basic principle and potential applications have been demonstrated. However, to establish this technology as a nano-processing tool, a lot of work on optics, materials and electronic controlling has been done to reduce the writing laser power, evaluate and improve the fabrication accuracy and efficiency, and launch new applications.

4.1 Circumventing the Diffraction Limit

Compared with projection lithography (photo, x-ray and electron beam) and soft lithography technologies, two-photon photopolymerization is unique in its 3D processing capability. However, the use of relatively long wavelength worsens the spatial resolution, for which the bottleneck is set by the optical diffraction limit [125, 126]. This is a limiting factor for the wide application of this technology. In this section, we will introduce how to circumvent the restraint and achieve SDL accuracy in 3D fabrication.

4.1.1 The Diffraction Limit

Optical diffraction plays an essential role in the resolving power of a focusing light microscope, which was revealed by Abbe's work on image formation [126]. His insight initiated imaging approaches such as electron and scanning tip microscopes. Spatial resolutions in these techniques were improved either by decreasing probe beam wavelengths using atom, electron or ion waves, or by using a sharp tip-end to reduce the probe-specimen interaction area as done in scanning tunneling microscopes (STMs) [149], atomic force microscopes (AFMs) [150] and near-field scanning optical microscopes (NSOMs) [151]. The resolution reported for these systems range from hundreds of nanometers down to the remarkable value of less than one nanometer. However, almost all of these methods abandon the use of light (STM, AFM) or the propagating modes of light (NSOM) and are therefore applicable only to surface imaging and fabrication.

In two-photon 3D lithography, the nominal Gaussian output of the laser underwent beam expansion and focusing, and was spatially filtered, producing a relatively flat wave front. Light distribution at the focal plane arises essentially from Fraunhoffer diffraction on the aperture of an objective lens [126], of which the diffraction pattern is shown by the inset of Fig. 18.

For TPA, the SLI, I^2, is directly related to the photopolymerization rate. A near-focus SLI distribution is shown in Fig. 18. The light intensity in the focal plane was assumed to follow a formula due to Airy [126]:

$$I(x) = (2J_1(x)/x)^2 I_0 \tag{20}$$

where $x=2\pi\alpha\omega/\lambda$, w is the coordinate in the diffraction pattern, and $I_0=ED/\lambda^2R^2$ is the intensity at the center of the pattern, E is the total energy incident upon the aperture and $D=\pi a^2$ is area of the aperture with an effective radius a. For imaging, the resolving power was limited by Rayleigh's criterion, $\delta r=k_1\lambda/NA$, due to the signal overlapping from neighboring object points, where $k_1=0.4\sim0.6$ is a constant depending on the laser linewidth and projection geometry. The spatial resolution could be improved by utilizing either

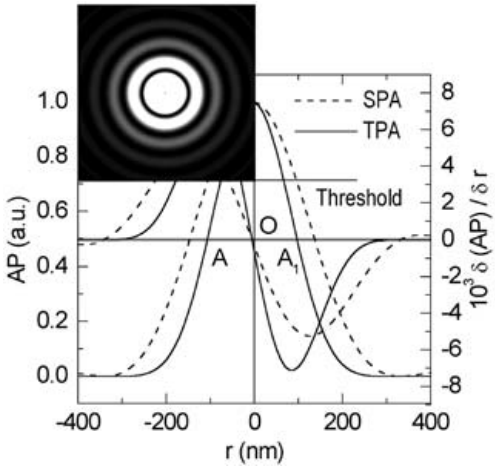

Fig. 18 Light intensity analysis for understanding the achievement of sub-diffraction-limit spatial resolution. Focal plane light intensity (dashed line) and the square of light intensity (solid line) distribution are associated with single-photon and two-photon excitation, respectively. Their derivative distribution is also shown. The inset is the diffraction pattern at the focal plane

shorter wavelengths or larger NA focusing, but the diffraction limit cannot be circumvented. For direct laser writing, a single focused beam is employed, producing an Airy pattern. The issue of light intensity overlapping is eliminated and the light intensity at the focal point was continuously adjustable. Therefore, even if the focal spot size is fixed for a given optical system (wavelength and objective lens), the diffraction limit can be circumvented, provided that the photochemical processes responsible for the formation of voxels have a threshold response to light excitation. Here the *threshold* was a level of light intensity (Fig. 18), above which the photochemical reactions become irreversible (for example, photopolymerized). In this case, the diffraction limit becomes just a measure of the focal spot size; it does not put any actual restraint on voxel sizes.

4.1.2 A Thresholding Mechanism: Radical Quenching Effects

Thresholding performance depends on the individual mechanism of photochemical reactions. In radical type photopolymerization, the oxygen molecules play an important role in the reaction process [5, 152] as described by Fig. 19. Oxygen quenches polymerization via two possible routes. The first is triplet state quenching (T-quenching), where the triplet state of the initiator molecules can be directly consumed by reacting with oxygen molecules without generating any radicals. This is a relatively weak effect. For example,

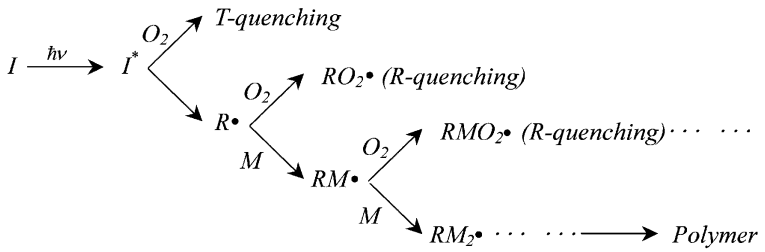

Fig. 19 Photopolymerization quenching by oxygen molecules under two mechanisms: triplet state quenching (T-quenching) and radical quenching (R-quenching). The latter is the major factor that works in the sub-diffraction-limit fabrication

given an oxygen concentration $[O_2]\sim10^{-3}$ M^{-1} and a typical rate constant of bimolecular quenching in fluid solution of 10^9 $M^{-1}s^{-1}$, the reaction rate is of the order of 10^6 s^{-1}. A triplet state shorter than 100 ns would not be significantly influenced by the presence of oxygen. In resins, particularly acrylate resins, the high viscosity makes the rate constants even smaller. Therefore triplet quenching doesn't play a significant role. The second effect is radical quenching (R-quenching), where radicals combine with oxygen molecules, producing much less active peroxial radicals. This phenomenon, common in radical type polymerization, is the origin of the reaction induction period and it reduces polymerization efficiency [153]. The two-photon photopolymerization threshold is closely related to the radical quenching effect.

Due to the quenching effect, the existence of oxygen is generally considered as detrimental factor in polymerization. Measures were taken to prevent it, including N_2 gas blowing, addition of O_2 barriers like paraffin waxes [154], addition of oxygen scavengers [155]: thiols, phosphines [156], and acrylate amines [4]. However, as a competing process of polymerization, the quenching effect may be utilized as the thresholding effect to confine the polymerized voxel size [13, 14, 102]. By tailoring the light intensity at the focal volume, it is possible to reach a state where TPA-induced radicals survive and initiate polymerization only at the region where exposure energy is larger than the threshold. The intensity of high-order diffraction features (see the subsidiary maxima in the inset of Fig. 18) was low, and therefore easily controlled under the TPA threshold. It is interesting to study the region A_1A in Fig. 18. Judging from the derivative distribution of absorption probability, the voxel size more sensitively depends on variation of the light intensity for TPA than for single-photon absorption, implying that the former possesses a more pronounced threshold effect, although both benefit from it. For the same reason, TPA provides an important mechanism for optical power limiting and power stabilization.

4.1.3 Realization of Sub-Diffraction-Limit Features

The above physical scenario was experimentally evidenced [13, 14]. Figure 20a shows the SEM image of voxels formed under different exposure durations and laser pulse energies. Voxel sizes are quite reproducible, fluctuating within less than 8%. This was firstly due to the high stability of the output laser pulse energy, and secondly aided by the utilization of a diaphragm that served as a spatial filter, allowing a relatively flat field. A lateral spatial resolution down to 120 nm (the inset of Fig. 20a) has been achieved, which is much better than that attained by conventional TPA photopolymerization and that by laser rapid prototyping. A logarithmic dependence of voxel size on exposure time was obtained (Fig. 20b), which is a natural result of the exponential decay of the oligomer/monomer concentration versus exposure [152]. By linearly fitting the experimental data using the least-squares method and extrapolating the curve to zero diameter, threshold exposure times

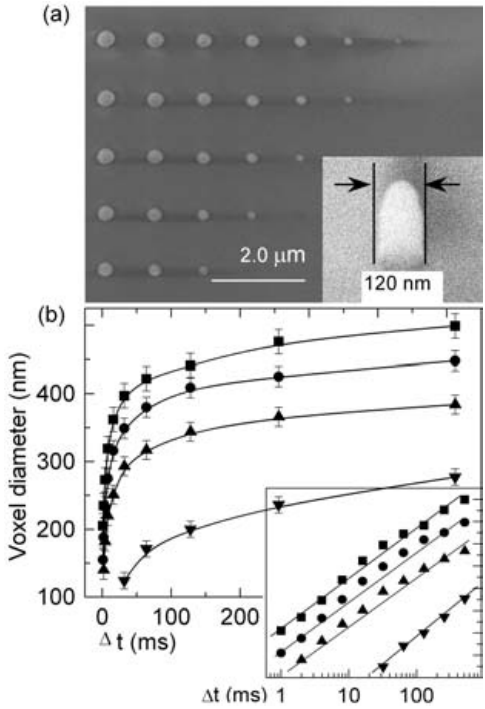

Fig. 20 Achievement of sub-diffraction-limit voxels. **a** SEM image of voxels formed under different exposure durations, and **b** an exposure time-dependent lateral spatial resolution. The right-lower inset represents the dependence in half-logarithm coordinates. For different curves, the laser pulse energies are 163 pJ (filled squares), 137 pJ (filled circles), 111 pJ (filled triangles) and 70 pJ (up-side-down filled triangles), respectively

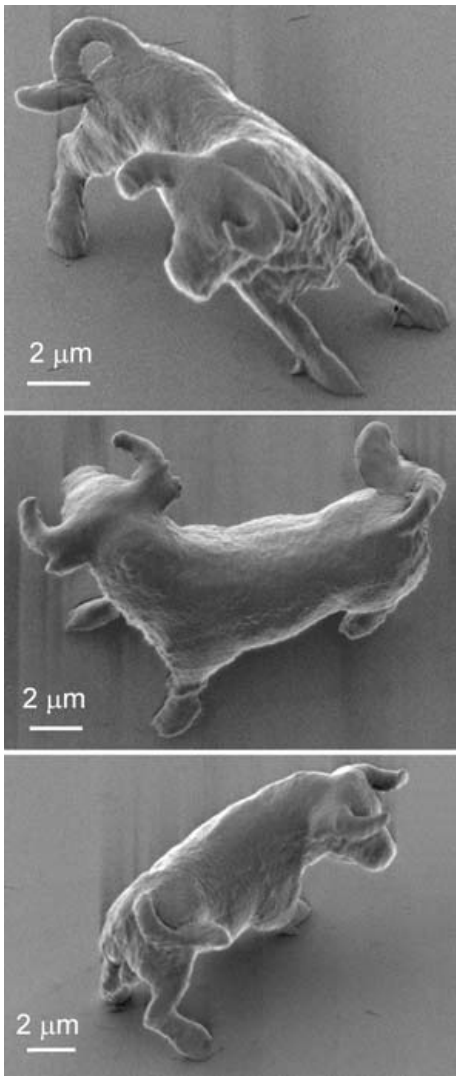

Fig. 21 Different view-angle SEM images of a micro-bull sculpture that was two-photon photopolymerized with sub-diffraction-limit accuracy. The 10-μm long and 7-μm high bull is believed the smallest animal sculpture that was ever fabricated

were determined to 0.1, 0.23, 0.6 and 18 ms for laser pulse energy of 163, 137, 111 and 70 pJ, respectively.

With the sub-diffraction-limit fabrication accuracy, it is possible to fabricate devices of nanoscale size or with nano-features. Figure 21 is the SEM image of a micro-bull sculpture, which consists of smooth and rough surfaces, curvatures and sharp horns. It is good proof of the feasibility of creat-

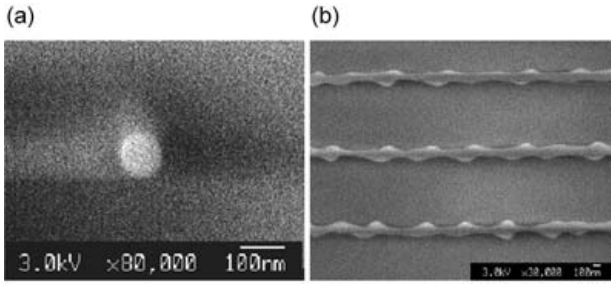

Fig. 22 Achievement of 100-nm lateral spatial resolution achieved after adding quenchers into SCR 500 resin. SEM images of a single voxel **a** and a line-dot structure **b**

ing sub-diffraction-limit features by two-photon photopolymerization. The 10 μm long and 7 μm high bulls are the smallest animal sculptures ever made artificially, and are as small as a red blood cell. Their volume allows us to send them, or actually micromachines of this size, to any location inside the human body through blood micro-vessels to make clinical treatments.

Any chemical species that tends to prohibit photopolymerization reactions, even in small concentrations, is called quencher. Oxygen is just one of many choices of quencher [154–156]. By attentively adding prescribed quenchers into resin solution, it is much easier to control polymerization than use of dissolved oxygen. Figure 22 shows line structures of 100 nm width that were two-photon photopolymerized with the same resin, SCR 500, except for an additional quencher. It is believed that by properly choosing quencher species and optimizing their concentration, a further decrease of polymerized voxel size is possible.

4.1.4 Point Spread Function Engineering

Besides the utilization of specific material properties like the thresholding effect, another promising route to tailoring voxels is by designing the point spread function (PSF) at laser focus using adaptive optics. Dry optics is inevitable if long work distance lenses are needed, and high refractive index resins, either intrinsic or doped, are important for realizing full-PBG PhC. Each case suffers from aberrations, which are induced because of the refractive index mismatch between the objective immersion medium (air or oil) and a cover glass, or between a cover glass and the resins [157]. The induced aberrations, consisting primarily of spherical aberration, increase linearly with focusing depth and cause a lateral broadening of the focal spot and, more importantly, a lengthening in the axial direction [158]. The larger size of the focal spot means a worse spatial resolution.

Aberration can be compensated by pre-shaping the light beam with an equal but opposite aberration using adaptive optics, ensuring an aberration-free focal spot [159]. An adaptive optics system consists primarily of a wavefront sensor for measuring aberrations, a wavefront correction element and a control system to interface the wavefront sensing and correction. A number of existing wavefront sensing technologies can be used for this purpose. Typical wavefront correction elements include pixellated spatial light modulators (SLMs), pixellated and deformable mirrors. A ferro-electric liquid-crystal SLM can be configured as an arbitrary wavefront generator, however, its low throughput (~1% at 800 nm) makes it impractical to provide sufficient energy for voxel polymerization. We utilized deformable membrane mirrors, which are micromachined aluminized silicon nitride membranes suspended above an array of electrodes. Voltage applied between the electrodes and the membrane allows control of the mirror shape. These mirrors are particularly convenient for the correction of low order aberrations such as those predominate in two-photon polymerization fabrication.

4.2 Characterization of 3D Focal Spots

A focal point was originally defined in ray optics as a geometrical point at which parallel light rays, incident on a lens (or mirror), are focused after refracting or reflecting. Further treatment involved diffractions at an aperture, on which primary imaging theories were established [126]. 3D lithography including two-photon photopolymerization is pursuing sub-diffraction-limit accuracy, and a spatial resolution 20% of the diffraction limit has been achieved (Figs. 20 and 22). Apparently, it is not appropriate to consider the focal spot as a geometric point any more, but we should be concerned with its internal structure, most importantly, the shape and size of a focal spot that is related to two-multiphoton absorption.

4.2.1 Two-Photon Excitation Related Focal Spots

The linear light intensity distribution near focus had been theoretically investigated by Lommel and Struve [126]. Their method can be approximately applied to two-multiphoton processes. For simplicity, we discuss hereafter only two-photon excitation without loss of generality. To study two-photon excitation-related focal spots, one is interested in the SLI at the focal volume. To experimentally investigate a two-photon focal spot in 3D, one needs (i) a medium that responds proportionally to the SLI; and (ii) a technique that is capable of revealing 3D features of focal spots. Direct observation of two-photon fluorescent spots with a CCD camera tends to give less accurate and distorted images due to insufficient resolving power and sometimes due to

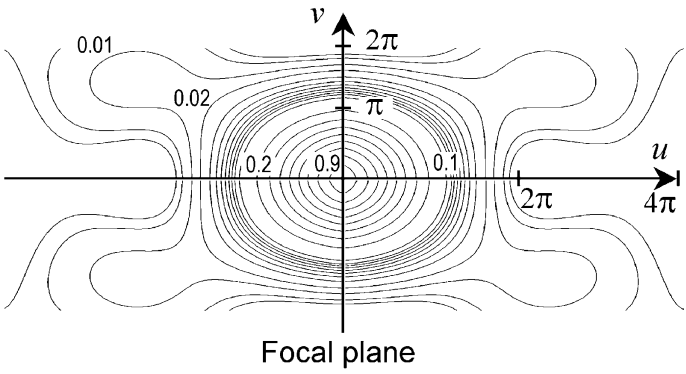

Fig. 23 The SLI isophotes of a focused laser beam. Unitless parameters, *u* and *v* are normalized axial (*z*) and lateral (*r*) coordinates. For details, see [126]

CCD pixel size limitation and possible fluorescence saturation. A femtosecond time-resolved optical polarigraphy method for visualizing laser pulse propagation was recently demonstrated by Fujimoto et al. [160], from which, however, pure information on the focal spots is difficult to extract.

Starting from the work by Lommel [126], it is easy to calculate the near-focus SLI contour. A complicated SLI distribution was found near the focal region, but a tubular structure of high light intensity (Fig. 23) exists in the central portion of the diffraction pattern. Generally only this regularly formed volume is useful for microfabrication and imaging. This two-photon excited tubular volume can be several times larger than the diffraction limit, and theoretically could be as small as several tens of nanometers, limited by the polymer molecular size. Since diffraction occurs at circular apertures imposed by lenses, in the neighborhood of the focus the intensity distribution, and therefore SLI, is rotationally symmetrical about the optical axis (*u* axis in Fig. 23), and mirror-symmetrical about the geometrical focal plane. The inflence of beam polarization will be discussed below in Sect. 4.3.2.

To experimentally investigate TPA focal spots, one needs a direct two-photon responsive medium. When IR ultrashort laser pulses were tightly focused in a resin, initiators were decomposed into radicals by simultaneously absorbing two photons. The number of photons absorbed per molecule per unit time by means of TPA is proportional to the TPA cross-section, δ and to SLI. The total number of photons absorbed per unit time is also a function of initiator concentration, *C*, and the excited sample volume, *V*. In the absence of saturation and photobleaching, the number of radicals generated per unit time, *N*, is given by:

$$N = C\delta\phi I_0^2 \int_V S^2(r,\theta,z)dV \tag{21}$$

where I_0 is the light intensity at the geometrical focal point, $S(r,\theta,z)$ is a unitless function used to describe the spatial distribution of the incident light, and φ is the quantum efficiency of radical yield. The shape of the TPE focal spot is determined by $S^2(r,\theta,z)$. The radical distribution would represent the SLI distribution. Mathematically, radicals play a role of "$k\sqrt{}$"*operator*, converting the squared light intensity to linear concentration, where k is a constant that can be deduced from Eq. 21. Physically, the oligomer and monomers act as a *3D "film"* to fix the distribution of the radical where its concentration is higher than the threshold of a solid voxel.

4.2.2 Ascending Scan Method

To practically realize the idea formulated above, a Ti: Sapphire mode-locked laser system that was operated at 76 MHz and delivered 780 nm, 150 fs laser pulses was employed. The laser beam was focused by a high NA (~1.4) objective lens. The SCR 500 resin was dropped on a microscopic cover-glass substrate. The sample stage was moved up and down along the optical axis using a piezo stage (Fig. 20a). An important issue for obtaining isolated, complete 3D voxels is substrate truncating, which caused a lot of observa-

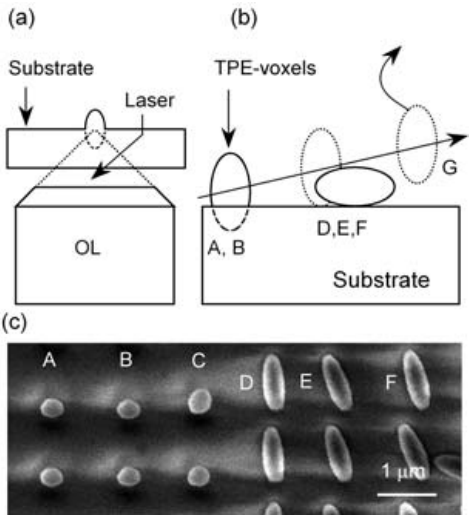

Fig. 24 Schematic ascending scan method for achieving isolated and complete 3D voxels. **a** laser beam focusing that illustrates the substrate truncation effect, **b** voxels formed at different focusing level, and **c** SEM image of voxels produced by scanning the laser focal spot from inside to above the substrate

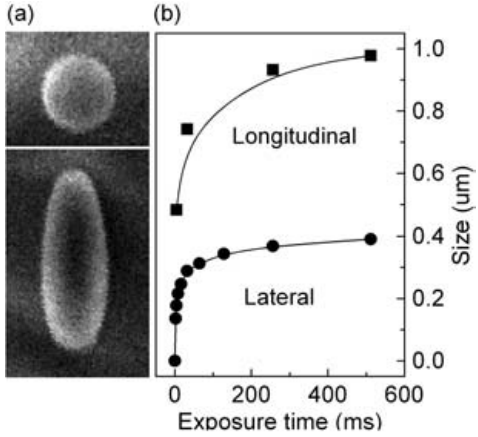

Fig. 25 **a** An isolated and complete voxel, the 3D image of two-photon excitation related focal spot, and **b** exposure time-dependent lateral and longitudinal voxel size

tion errors as discussed later. Truncation happens when the laser is focused too near the substrate surface (Fig. 24b); on the other hand, floating voxels would be formed which would be flushed away during developing if the laser was focused too far above the substrate.

To solve this problem, an ascending scan method was proposed by Sun et al. [20]. The laser focus was scanned along a slant line (the arrowed straight line in Fig. 24b). The arrow denotes the scanning direction from below to above the substrate surface, residing at a series of positions. At each position, the shutter in the light path was switched on and kept for a short term, the exposure time, to get voxels at an identical exposure condition. Figure 24c shows SEM images of the produced voxels. The left voxels (**a**, **b**, **c**) were truncated voxels. They stuck to and erected on the substrate, revealing only their lateral size information. The rightmost voxels were floated away (not shown). A transition state always existed between these two regions: the edge of voxels bordered at and weakly adhered to the substrate surface, and they were overturned during developing. That is the case for **d**, **e**, **f**, from which both lateral, and most importantly, longitudinal information could be attained.

Figure 25a shows top- and side-view SEM images of a voxel. It resembles a spinning ellipsoid with axis length of 2a=3.4 μm and 2b=1.4 μm. Therefore an axial ratio can be defined as $\mu = \frac{a}{b} = 2.4$. The theoretical value for a voxel of the same lateral size is, however, μ=2.8 according to Fig. 1. The deviation may be due to the over-simplification of the model. However, a near-circular cross-section $(\mu = 1)$ of rods could be achieved, for example, by adaptive optics [157–159] or by multiple line-scannings [15, 17], where the scan positions were laterally offset.

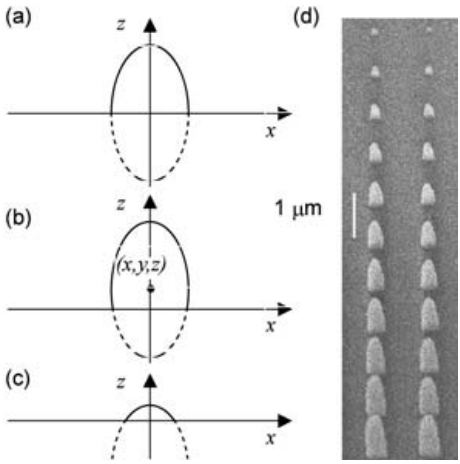

Fig. 26 Focusing depth dependent vertical and longitudinal voxel size, which is the origin of most observation errors. The laser was focused at different positions to produce **a** exactly half, **b** over half, and **c** less than half voxels. **d** SEM image of voxels corresponding to the situation of (a), (b) and (c)

Here the focal spot was defined as an energy-concentrated 3D volume demarcated by a series of intensity isophotes, while the voxel is the primary fabricating unit. Focal spots are sometimes not truly reflected by voxels: for example, when the laser pulse energy is so high as to induce breakdown [143]. In particular, in the case of micro-explosion [49], the shape of voxels was significantly different from that of the focal spot. In the current 3D photographing method, for a fixed optical system at a certain laser pulse energy, one can use the ascending scan method to map the focal spot layer-by-layer from the core center ($a,b \rightarrow 0$) to any large size that is limited by breakdown by changing exposure time (Δt). Figure 25b shows an example of Δt-dependent voxel sizes. Since only the appearance of voxels contributes to its dimensions, even if photobleaching or excitation saturation occurs at the central portion, where the intensity maximum exists, the imaging accuracy is not affected. It was observed at different laser pulse energy levels until breakdown that the longitudinal size of voxels was always proportionally related to its lateral size, but the axis ratio increases with the increase of exposure.

Now we can analyze how the conventional observation error of spatial resolutions originated. The situation of lateral size is slightly complicated. A critical case is that the geometrical center of the focal spot (x, y, z) falls exactly on the substrate surface (z=0, Fig. 26a), where the potential voxel is half cut. Focusing at this and positions higher than this level ($0<z<a$, Fig. 26b), the top observation would give rise to an identical lateral voxel size, $2b$. This is the case of voxels **a**, **b**, **c** in Fig. 24c. If less hemisphere is ex-

posed ($-a<z<0$), any values ranging from zero to $2b$ would be possible depending on how large a percentage of the focal spot volume comes out of the substrate.

The above analysis was experimentally tested using the ascending scan technology. The exposure started when the entire focal spot was immersed in the glass substrate, then the focusing height level was increased step by step. Although the exposure time and laser pulse energy were the same for all voxels, many different lateral and longitudinal sizes were obtained (Fig. 26d). For longitudinal resolutions, the situation is simple; any measurement of erected voxels gave a value less than the real one. We believe that most of the reported resolution measurements were performed without properly considering the truncation effect. Therefore, measured values are more or less smaller than the actual size, $2a$. It is the substrate truncation that causes most measurement errors, sometimes leading a the confusing conclusion.

4.2.3 Suspending Bridge Method

It is technically challenging to observe voxels of lateral dimensions of 100 nm or less using the ascending scan method because, first, the voxels themselves have difficulty surviving developing, for which special care has to be taken; and second, when size reaches this scale, voxels adhered to the substrate surface position themselves in random orientations instead of overturning. DeVoe et al. [161] proposed a suspended bridge method. Instead of producing a single voxel, a line suspended between two bridges was polymerized. The line width and height denote lateral and longitudinal resolution, respectively. In the test structure shown in Fig. 27, polymer lines were held between solidified polymer supports and suspended 15~20 μm above the substrate. The lines were written at scan velocity from 1.25 mm/min to 113 mm/min, and increased by $\sqrt{2}$ for each line, under constant average power. The supports were formed at lower speed scanning so that they were solid enough. The line width was designed to be quite long, ~100 μm, to avoid artifacts arising from stage acceleration and deceleration at the ends of lines.

The method was found effective for different types of photopolymers, cationic (SU-8 2025, MicroChem Corp.) and a radical resin. In the case of the PMMA/acrylate resin system, they obtained a resolution of 140 nm×200 nm. Although the technology is less effective than the ascending scan method for revealing more information about the focal spot, it may play a promising role in characterization of sub-100 nm spatial resolution. It is worth mentioning that, in this work, strong two-photon absorbers were added to diaryliodonium salts to yield a highly sensitive system for both cationic and

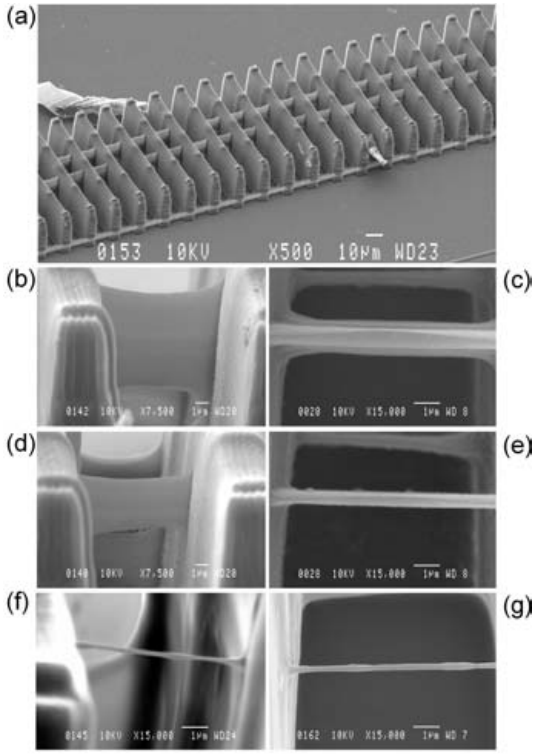

Fig. 27 SEM images of suspended crossbar structure in PMMA/acrylate resin for voxel shape determination. Note scale bars in each photo. **a** overview of entire structure. **b** and **c**, top and side views at 2.58 mW, 0. 12 mm/s; **d** and **e**, top and side views at 2.58 mW, 1.9 mm/s; **f** and **g** top and side views 1.07 mW, 1.9 mm/s

radical polymerization, which expanded the dynamic power range tby two orders and permitted voxel size tailoring of the same order.

Similar to the case of two-photon excitation, for multiphoton absorption the initiators would perform an operation of "$k\sqrt{[n]}$" with a much smaller coefficient k for n-photon absorption. The above two methods and knowledge acquired about the focal spot related to two or multiphoton excitation is essential for not only photopolymerization fabrication, but also important for understanding excitation behavior for various laser microfabrications.

4.3 Understanding the Role of Laser Parameters

Laser beams are described by their spatial, temporal, spectral and polarization distributions in addition to coherence properties [33–35]. At fundamental limits, the beams can be diffraction and bandwidth limited, linearly

polarized and coherent. A Gaussian beam, the 3D solution of the wavefunction derived from the Maxwell function, represents the highest possible beam quality and satisfies the above requirements, and near-Gaussian output is already available from many commercial lasers. For example, a 780 nm wavelength laser with a 100 fs pulse width at a repetition rate of 80 MHz possesses a spectral full width at half maximum (FWHM) of approximately 10 nm, implying a time-bandwidth product of $\Delta t\ \Delta\omega$=0.493, near the transform limit of 0.441 of a Gaussian pulse shape. The beams can almost be utilized as they are, although sometimes beam expanding and spatial filtering is used to form a far-field pattern with a high symmetry of energy distribution. A short pulse width (<1 ps) is essential to provide a high transient power in order to launch nonlinear optical processes and exclude thermal effects, which are difficult to localize. The broad laser spectrum associated with the ultrashort pulse width brings about chromatic aberration, which is overcome by usage of apochromats.

4.3.1 Numerical Aperture

Compared with the roles of temporal, spectral and coherence performances discussed above, laser energy distribution and beam polarization directly determine the spatial resolution of fabrication. After spatial filtering and beam expanding, only the central portion of the laser beam is induced into an objective lens. It is already known that the focal spot size is estimated using the Rayleigh criteria, $Z_R=n\pi\omega_0/\lambda_0$ along the optical axis, where n is the refractive index of the medium into which the laser is focused, λ_0 is the vacuum wavelength, and $\omega_0=1.22\lambda/(n\text{NA})$ is the lateral diffraction limit. It is clear that the objective lens strongly redistributes the beam energy, and the laser intensity distribution at the focal region sensitively depends on NA. For a better understanding of the role of NA in two-photon nanofabrication, a theoretical simulation was conducted, for which the vectorial Debye theory was utilized since the paraxial approximation does not hold any more when focusing using high-NA optics (NA>0.7). Figure 28 shows two-photon PSF of different NAs in both x and y directions (Fig. 28a), and along the optical axis, the z direction (Fig. 28b). The refractive indices of the cover glass and the resin were adopted as experimental values, 1.518 and 1.52, respectively, and the laser is assumed to polarize along the x direction. The incident power before the aperture, which has variable size, is assumed to be identical in each case.

The peak power increase with NA is natural, due to the increase of convergence angle. Spatial resolution is improved at high NAs. For example, using the FWHM as the criterion of resolution, NAs of 1.4, 1.2, 1.0 and 0.8 give rise to FWHMs of 252 nm (450 nm), 269 nm (525 nm), 304 nm (629 nm) and 343 nm (787 nm) in the x direction and 542 nm (1860 nm), 765 nm

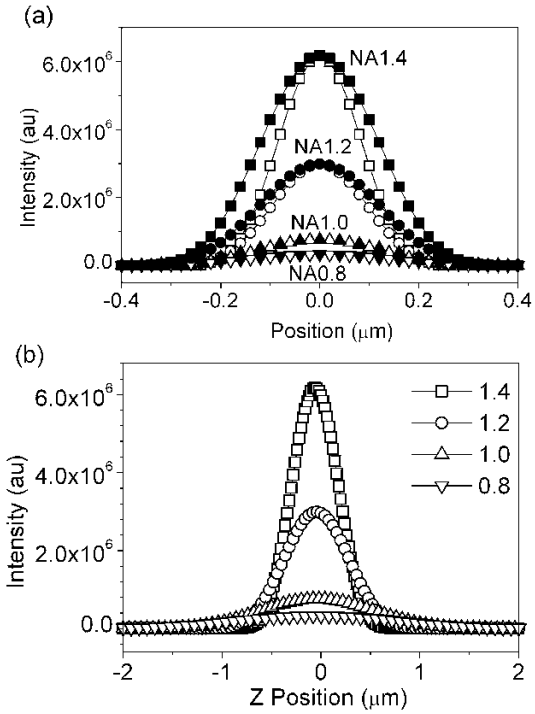

Fig. 28 Theoretical two-photon point spread function of different NA focusing calculated using vectorial Debye method. An identical incident power was assumed before the aperture. **a** Functions along x axis (solid symbols) and along y axis (open symbols). **b** The function in the longitudinal direction (z axis). Laser beam was assumed to be incident from the bottom and focused 10 μm above the glass substrate

(2525 nm), 1327 nm (3640 nm) and 1848 nm (5710 nm) in the *z* direction, respectively (the diffraction limits are listed in the parentheses, indicating the size of the central Airy pattern). It is seen from the figure that regardless of the absolute intensity level, low NA tends to give larger feature sizes in both lateral and longitudinal directions.

The above result is consistent with that predicted in imaging theories [162, 163]. It is interesting to know whether a similar rule holds true when a femtosecond laser interacts with a typical nonlinear material in a two-photon nanofabrication processes. The ascending scan method [20] was used to explore this, making it possible to intuitively discriminate how the focal spot size and shape are influenced by NA and other laser parameters. Shown in Fig. 29a are the side-view SEM images of voxels formed with objectives of NA 0.88, 1.12 and 1.4, respectively. In order to get comparable data, the exposure power measured at the objective output was kept identical and the

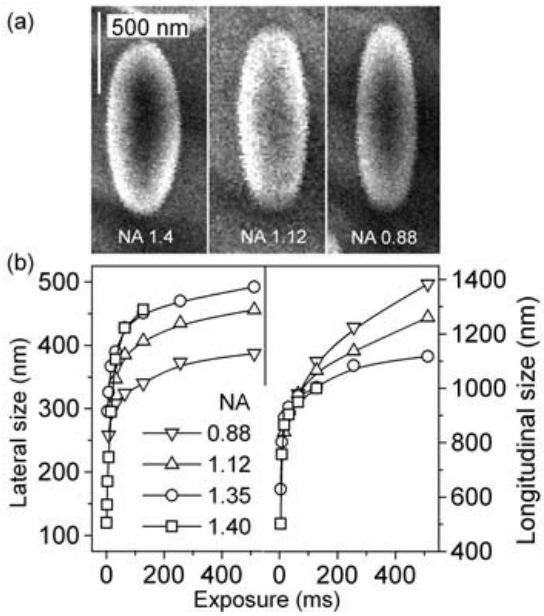

Fig. 29 NA-dependent voxels. **a** Side-view SEM images of voxels formed by focusing objectives of different NAs, 1.4, 1.12 and 0.88, where the power output from the objective lens was kept identical. **b** Exposure time-dependent voxel size in both lateral and longitudinal directions under different NAs

exposure time was chosen to be relatively long, 250 ms per voxel, so that the voxel size is reasonably large.

From Fig. 29a it is found that the axial ratio increases as NA decreases, as expected, from 2.3 (NA~1.4) to 2.7 (NA~1.12) and 3.3 (NA~0.88). This relationship is similar to that obtained from the theoretical FWHMs (Fig. 28): 2.2, 3.5 and 4.9 for 1.4, 1.12 and 0.88 NAs, respectively. In Fig. 28, it is implied that not only the longitudinal but also the lateral axis lengths of voxels obtained at low NAs are larger than those obtained from high NAs. However, it is seen from Fig. 29a that the low-NA voxels are smaller in lateral dimension. This contradiction, essential in choosing appropriate optics for laser nanofabrication, apparently needs clarification.

Various exposure conditions were tested and it was found that although at a medium irradiation level low-NA focusing gave rise to smaller lateral voxel size (350 nm at 0.88 NA versus 460 nm at 1.4 NA in Fig. 29a), the smallest visible voxels achieved with 0.88 and 1.4 NA optics were 260 nm and 120 nm, respectively. This phenomenon was interpreted by the threshold effect [13, 14]. In the case of low-NA focusing, the laser power is distributed to a larger volume, and then the solidified front demarcated by the threshold camber is vertically expanded and laterally shrunken. Therefore

low-NA gives laterally smaller voxel size. The gradient of light intensity distribution in a high-NA focused light field is steeper and energy is more concentrated in the center of focal spots, which causes photopolymerization at smaller volume. Therefore, for pursuing high-accuracy nanofabrication, a high-NA objective is still preferable.

4.3.2 Polarization

In the above discussion and in reports published up to now, it is always considered that the appearance of a voxel resembles a spinning ellipsoid with axis lengths $a=b<c$. However, this is experimentally found to be not true if a general linearly-polarized laser beam is employed. Shown in Fig. 30a is the lateral SEM image of a voxel formed using 1.4 NA optics when the Ti: Sapphire laser output was utilized as it was. The voxel axis lengths are $2a$=325 nm (x direction) and $2b$ = 295 nm (y direction), giving rise to a lateral axis ratio $\mu_{\|}=a/b$=1.1.

This phenomenon can be understood by considering the depolarization effect predicted by electromagnetic focusing theory [163, 164]. It is already known that when the beam incident angle α is small, the focal field (E_x, E_y, E_z) is sufficiently described by a cylindrically symmetric function [$E(r)$, 0,0]

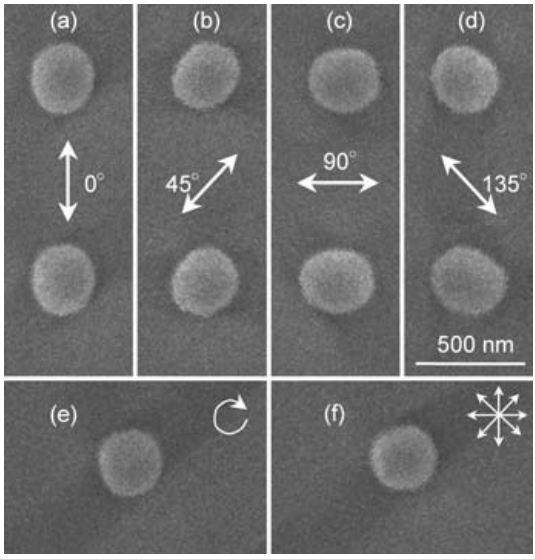

Fig. 30 Polarization effect. The laser was focused by oil-immersion 1.4-NA objectives. **a**, **b**, **c** and **d** are top-view SEM images of voxels formed with laser of different linear polarizations, from which a nearly 10% lateral axis ratio was observed. **e** Voxels produced at the same incident power but with circularly polarized laser and **f** nonpolarized laser

with $r = \sqrt{(x^2 + y^2)}$, where the input beam is assumed to be along the x direction. Nevertheless, when α>40° (NA>0.7), the symmetry is broken and a field with significant E_y and E_z components appears. More precisely, the electric field can be expressed as:

$$E(r_2, \phi, z_2) = \frac{\pi i}{\lambda}\{[I_0 + \cos(2\phi)I_2]\mathbf{i} + \sin(2\phi)I_2\mathbf{j} + 2i\cos\phi I_1\mathbf{k}\} \quad (22)$$

where **i**, **j** and **k** are the unit vectors in the x, y and z directions, respectively, and variables r_2, z_2 and φ are cylindrical coordinates of an observation point. I_0, I_1 and I_2 are not constant-zero variables (see definitions in [163]). Hence, it is clear that the electric field at the focal region is depolarized. The calculation result is shown in Fig. 28, from which the lateral axis ratio is deduced to around 1.30, estimated using FWHMs.

The experimental lateral axis ratio is smaller than the theoretical expectation and depolarization can also be caused by lens imperfection or tension. To confirm the origin of a non-unit lateral axis ratio, the beam polarization direction was adjusted relative to the objective. As a result, the voxel orientation was found to be correspondingly rotated while the size and shape were kept unchanged (Fig. 30b,c,d). Similar experiments were conducted with low-NA optics and it is found that when NA is smaller than 1.0, the lateral eccentricity was not discernible.

With the depolarization effect experimentally confirmed, some technical issues could be clarified. For example, it had been previously observed that when scanning linearly-polarized laser in resin, the widths of photopolymerized lines along different directions are slightly different. This deviation can now be attributed to asymmetrical light field distribution due to the depolarization effect if the scanning speed of stage is equal in different directions.

A round-shape lateral cross-section of voxels is preferable in most fabrications. We tried to eliminate the non-unit lateral axis ratio by polarization modification. Circularly- and non-polarized beams were realized by inserting a 780 nm antireflection-coated c-axis-cut quartz $\lambda/4$ retardation plate and a visible-range double-plate-type quartz depolarizer into the light path, respectively. In both cases, there is no preferential direction of light intensity distribution at the focal spot. Experimentally a nearly perfect round shape was achieved for both cases, as shown in Fig. 30e,f.

4.4 Raster Scan versus Vector Scan

Laser scanning is the step needed to convert pre-designed CAD patterns into real structures. Two basic modes for direct laser scanning can be utilized, raster-scan mode and vector-scan mode, of which the concepts are illustrated in Figs. 31a, b.

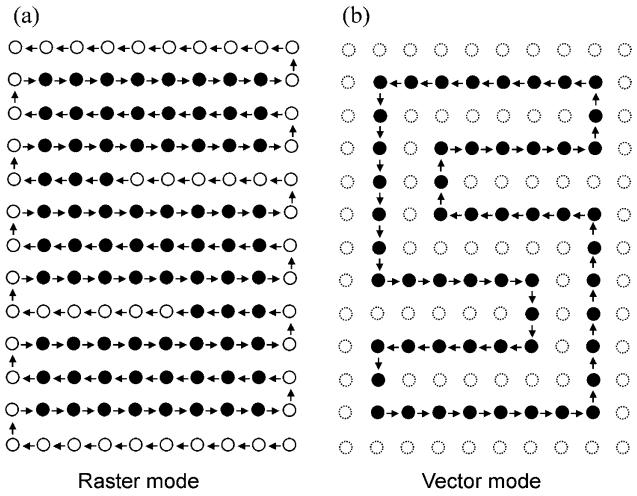

Fig. 31 Two basic scanning modes for two-photon photopolymerization microfabrication. Conceptive illustration of how the two scan modes could be utilized for writing a character "s". **a** raster scan and **b** vector scan. The solid and open circles denote exposed and unexposed dots, respectively, all scanned by the laser focal point. The dashed open circles in the right part means the dots that aren't scanned

In the raster mode, all voxels in a cubic volume that contains the microstructure are scanned by the actual/virtual laser focal spot, depending on having the shutter ON (actual)/OFF (virtual). In the vector mode, the laser focus directly traces the profile to be defined. Figure 31a and b respectively illustrate how a character "s" could be scanned with the two modes. Apparently the vector mode requires a smaller number of voxels. Depending on the structures, variations and combinations of these two basic modes could be used.

Experimentally the same object was fabricated using the two modes. The micro-bull in Fig. 21 was produced using a layer-by-layer raster-scanning scheme; all voxels that made up the bull were exposed point-by-point, line-by-line, and layer-by-layer by the two-photon process. As a result, it took three hours to complete the manufacturing. If we make a detailed analysis of the bull structure, it is found that the entire bull consists of 2×10^6 voxels. However, the bull profile can be well defined using only 5% of them. As a test, the bull was written once more using vector scanning as shown in Fig. 32. Astonishingly, we found it possible to depict the same structure within 13 minutes. In both cases the scanning step in three dimensions was 50 nm. However, the fabrication time in vector scan was reduced by more than 90%.

The TPA-produced bull crust was self-supported, standing on glass substrate either in liquid or air. To avoid possible distortion, we further solidi-

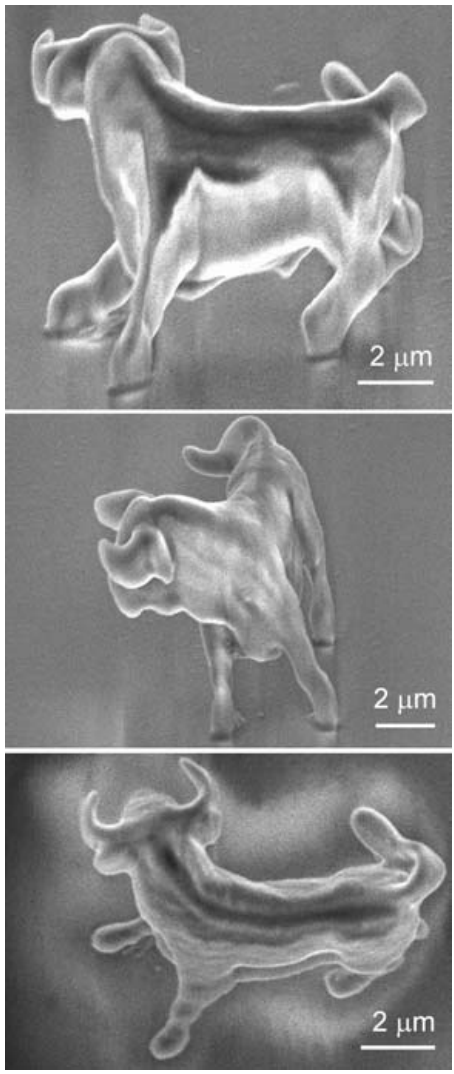

Fig. 32 A micro-bull scupture produced by vector scanning. Only the crust was defined by the two-photon process; the inside was solidified by illumination under an mercury lamp. In this particular structure, the two-photon scanning time was reduced by 90% due to the use of a vector scanning mode

fied the structure under a mercury lamp, which is a single-photon exposure process. This is an additional step but technically quite simple.

In the vector scanning method, voxels were actually classified into two categories: those on the surface layers are the least necessary points to define a structure and those inside the structure solely have the supporting

function. Discriminating between these two kinds of points and rendering a separate exposure is critical for vector scanning to improve the fabrication efficiency. Vector scanning uses less exposure time, but the stage movement controlling is a little more complicated. In addition, this method is not suitable for resins that have a large volume change in the liquid-solid phase transition, since the volume variation-induced tension can't be released in the fabrication process as it can in a raster scanning. Comparatively speaking, raster scanning is more suitable for producing structures with complicated shape, at a higher accuracy, and with a greater percentage of the least necessary points.

4.5 Three-Dimensional Micro-Diagnosis

An important issue in two-photon photopolymerization micro-nanofabrication is how to evaluate the internal structure of devices. 3D functional micromechanical systems and micromachines need proper positioning, shaping and jointing. A pre-operation evaluation is critical for judging and optimizing designs and fabrications. Shown in Fig. 33 is a tube structure, which should be hollow according to design. However, it is not an easy task to confirm the internal status even if it is a quite simple device. A normal optical microscope doesn't have sufficient resolving power to distinguish details in three dimensions, particularly in the longitudinal directions [165]. Electronic microscopes have a higher spatial resolution and higher imaging quality, but they are only useful for observing the appearance of objects. A two-photon confocal microscope possesses 3D imaging capability with resolution better than conventional transmission or reflection optical microscopes [165]. To attain a high signal-to-noise ratio, fluorescence readout is preferable and so the structure is required to emit reasonably intense fluorescence, which is not available in general resins that are used for microfabrication.

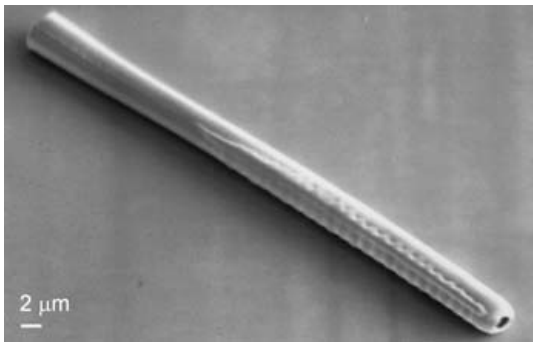

Fig. 33 A micro-tube structure, which is hollow according to design. However, it is difficult to confirm its internal status by conventional characterization technologies

4.5.1 Fluorescent Dye Doping

In order to use two-photon confocal 3D imaging, the fluorescence dye-labeling technology is found to be very useful. To induce fluorescence in photopolymerized structures, the laser dye of LD490 (Exciton Inc.), of which the major component is Rhodamine B, a fluorescent small molecule that is quite stable even under strong laser irradiation, was doped into resin before polymerization. The dye was introduced by dissolving SCR500 resin in an ethanol solution of LD490 until saturation. It absorbs and emits light with peaks at 396 nm and 474 nm, respectively (Fig. 34).

It is seen from Fig. 34 that the fluorescence wavelength of the dye was situated at the red end of the SPA absorbance curve, which may lead to fluorescence-induced polymerization. This problem can be solved by optimizing the fabrication-laser-pulse energy and the concentration of Rhodamine B so that local radical concentrations initiated by the TPA fluorescence are lower than the polymerization threshold, and then the radicals are quenched by dissolved oxygen.

A test structure was photopolymerized using the dye-doped resin following the normal procedure. For two-photon confocal readout, the system as used for fabrication was configured by adding a confocal pinhole and a CCD detector at the reading area. The laser pulse energy for reading was chosen to 1.5 pJ, two-orders smaller than that for fabrication, 130 pJ, in order to avoid optical damage. For minimizing imaging aberration arising from the mismatch of refractive indexes, structures were immersed in oil during the confocal scanning.

Figure 35 shows the two-photon confocal fluorescence images of a 5.4 μm×5.4 μm×5.4 μm cubic cage. From the design (the top illustration of Fig. 35), it is seen that different heights of the structure correspond to various cross-sections. This was clearly shown by the sliced fluorescent images

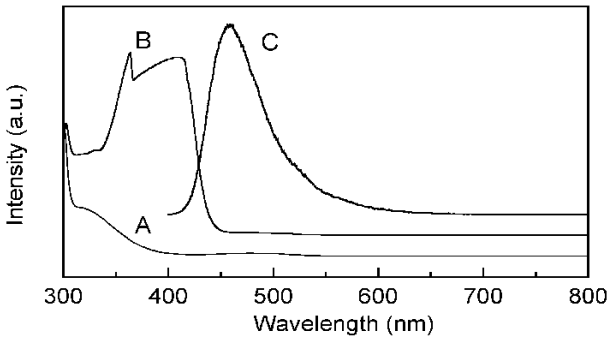

Fig. 34 Absorbance (**a**, **b**) and photoluminescence (**c**) spectra of undoped (**a**) and dye-doped (**b**, **c**) SCR500 resin

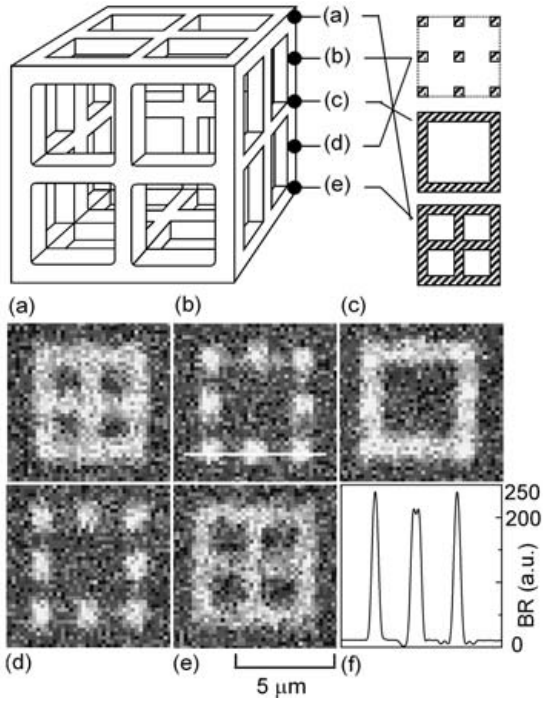

Fig. 35 Design (the top line drawing) and fluorescence images of a cubic cage fabricated by two-photon photopolymerization of dye-doped resin (**a**-**e**). The heights are **a**0.0, **b**1.35, **c**2.7, **d**4.05 and **e**5.4 μm, respectively. A fluorescence intensity distribution was extracted from **b** and given by **f**

(Fig. 35a–e). The fluorescence signal is more intense than that needed for reading. A signal/noise ratio of more than 20 (Fig. 35f, extracted from Fig. 35b) was obtained. In contrast, features of an identical cage solidified from unadulterated SCR resin can't be resolved due to a low signal-to-noise ratio.

Two conclusions can be reached from the above results. First, the fluorescence activity of the doped dye remained after a strong writing laser irradiation; and second, the fabrication spatial resolution was not much degraded after the dye doping. The seemingly poorer quality of the cage in Fig. 35 is due to the weaker resolving power of the optical microscope than SEM. Actually fabrication was not found to be degraded up to a Rhodamine B concentration of 1.0×10^{-4} M, and the cage was as smooth as those produced from non-doped resins under SEM.

4.5.2
Micro-Diagnosis in Three Dimensions

The above results indicate that the dye may act as a fluorescence label and dye-stained polymers will show themselves under laser irradiation, resulting in an effective fluorescence diagnosis technique with high spatial resolutions. In a confocal detecting scheme, the effective PSF, as a good approximation, is given by the square of the focal illumination intensity distribution in the objective lens so that, in a simplistic photon picture, only photons from the closest vicinity of the diffraction-limited spot contribute to the signal [165]. Aided by the intrinsic deep penetration capability of the TPA process, the effective focus acts as a 3D probe, and details of structures were shown by the distribution of fluorescence. Figure 36 shows confocal fluorescence images of axial and radial cross-sections of a tube similar to that shown in Fig. 33. The absence of internal fluorescence confirms its hollowness. The 1.6 μm internal diameter agrees well with the designed value.

The 3D confocal probe can be used not only for optical sectioning (Figs. 35 and 36) but also for reconstructing an entire 3D image of objects. Shown in Fig. 37 are reconstructed confocal fluorescence images of **a** a gear and **b** an icosahedron.

It is noteworthy that resin and dye were not optimized. If initiators with larger TPA cross-sections (10^3 larger or $1{,}250\times10^{-50}$ cm^{4}s/photon [22]) were utilized, the laser power necessary to launch photopolymerization would be decreased by the same order. This would effectively reduce the influence of

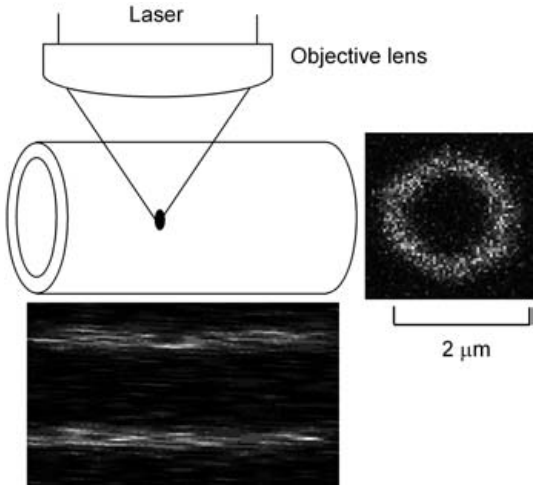

Fig. 36 Internal micro-diagnosis of a 3D micro-tube. Schematic (top) as well as axial (bottom) and radial (right) cross-sectional fluorescence images. The absence of the fluorescence inside the cross-sections indicates that there is no resin inside the tube

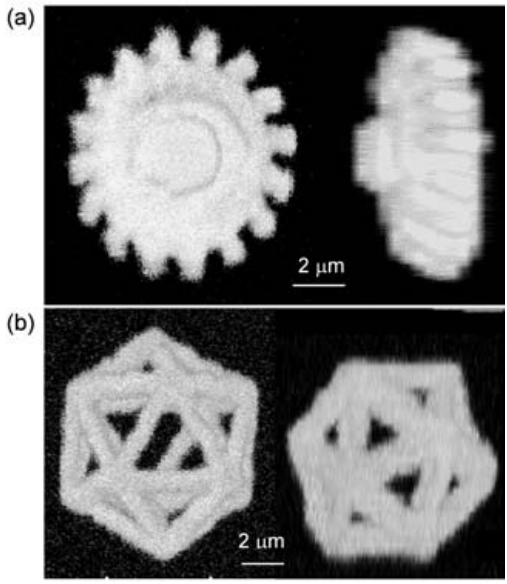

Fig. 37 Reconstructed 3D two-photon fluorescence images of **a** a gearwheel and **b** an icosahedron

two-photon fluorescence on polymerization, or equivalently, allow for dye doping at a much higher concentration without loss of spatial resolutions. The intense fluorescence emission, aided by a suitable positive-feedback, for example a PhC-based microcavity, would enable polymer devices like lasers or amplifiers. In fabrications, we could routinely dope (or co-dope with a dye for device functions) with a trace dye for 3D micro-diagnosis.

4.6 Multi-Beam Interference

As we will discuss in Sect. 5, one of the most important applications of two-photon photopolymerization is the fabrication of PhCs. By direct laser writing, PhCs with arbitrarily designed lattices could be created, which would facilitate the deep understanding of PhC physics and stimulate its broad applications in photonics and optoelectronics. For several particular types of lattices, PhCs may be created more conveniently by means of multi-beam interference.

4.6.1 Photonic Crystal Hologram

It is already known that when two or more coherent laser beams interfere with each other, a stable spatial pattern with periodically distributed light

intensity maxima and minima is formed. If the light intensity pattern is created inside a photopolymerizable material, and if the light intensities of each beam are properly chosen, it is possible that material at the maxima sites will be solidified, following the same interference pattern, while at volumes corresponding to light minima, the unpolymerized or less polymerized material can be removed during post exposure developing. As result, solidified interference patterns consisting of polymer skeleton and air voids function as 3D PhCs. This method has the following merits: (i) rapid production and relatively high accuracy due to the elimination of a scanning process; (ii) ease of batch production; (iii) suitability for large-volume samples up to a size of several millimeters; and (iv) system simplicity and low cost.

Both PhCs and holograms have periodical 3D dielectric functions and perform the complete reconstruction of the electromagnetic fields. It is reasonable to consider a PhC as a particular class of holograms [166, 167]. As a consequence of the periodicity of PhCs, the Fourier transform of the refractive index distribution function was well approximated by a small number of Dirac functions, implying that PhC holograms can be recorded by a small set of plane waves. The Fourier transformation manifests the relation of PhC lattices and the laser wavevectors that were involved in the interference: the wavevectors are the vectors of the reciprocal lattices. Therefore, PhC lattices can be designed by choosing a suitable number of beams, their geometrical arrangement, and their polarizations [166–169]. An SC lattice can be obtained by the interference of six beams, collinear or perpendicular to each other; a BCC lattice is realizable by four beams that are aligned along the axes of a standard tetrahedron; an FCC lattice, an ideal candidate for a large PBG effect, can also be realized by elaborately arranging four beams [39], about which we will give a detailed introduction shortly.

4.6.2 Layered Planar Hexagonal and Simple Square Lattices

The idea of constructing 3D PhC using multi-beam interference was proposed by Mei et al. in 1995 [36]. Berger et al. utilized this technology for 2D photoresist patterning [166–167]. 3D interference patterning in photopolymers was first reported independently by Shoji et al. [38] and Campbell et al. [37] in 2000.

Figure 38 shows the experimental scheme [40]. In the first step of the fabrication, Shoji et al. arranged three beams (442 nm, He-Cd laser) symmetrical to the sample surface normal, producing a structure with rods of uniform shapes arranged in a 2D triangular lattice. In the top-view SEM image (Fig. 39a), the bright spots correspond to the tip end of the micro-rods. The planar lattice constant is 1.0 μm, which can be adjusted by the incident angles of the beams. The rods were grown from the bottom to the top of the sample cell, and were 150 μm in length (Fig. 39b), distributed in an area of 500 μm diameter.

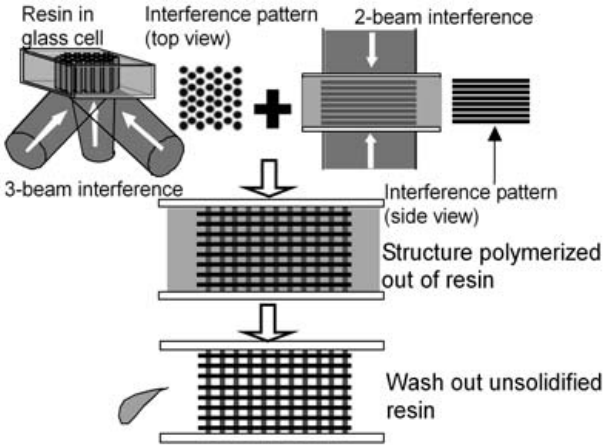

Fig. 38 The procedure of fabricating photonic crystals using two-step multi-beam interference technology. In the first step, a 2D planar triangular rod array was created by 3 symmetrical beam interference, and then the array was intersected by a series of polymerized planes that were produced by the second step two-beam interference

The above structure had translation symmetry along the rod axis, and there is no periodicity in this direction. For fabricating 3D PhC, two coherent beams were introduced from the cell top and bottom in the second step of the fabrication, where the rods were vertically intersected by 150 cross-sectional layers (Fig. 39c). So, by a combination of sequential three-beam and two-beam interferences, a 3D periodic structure was produced.

The two-step interference method, although technically a little complicated, has the freedom to design arbitrary lattice constants of different lattices. This is its significant merit compared with the single-step four beam interference by Campbell et al., which will be introduced in 4.6.3.

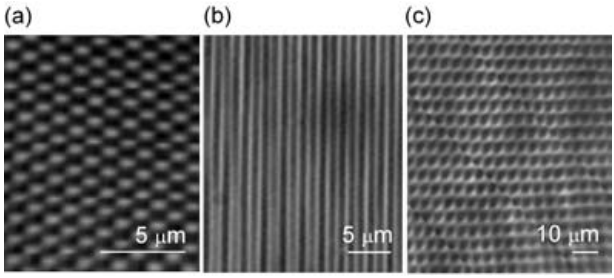

Fig. 39 SEM images of two-step multi-beam interference-produced PhCs. **a** top-view of the rod ends; **b** side view of the rods; and **c** side view after the intersecting layers were introduced

A similar rod array was produced by interference of four beams that were arranged with 90 °substrate-projection angles (120 ° for three beam as discussed above). In this case, rods were arranged with four-fold symmetry, so the cross-section has a simple square lattice with 700 nm periodicity [39]. With the additional fifth central beam, it is possible to induce cross-sectional layers. However, light distribution at the surface normal direction is not steep enough to give a sharp polymerized plane unless very tight focusing is employed. It is worth mentioning that, in this four-beam interference work, Kondo et al. [39] utilized a diffractive beam splitter for generating the four noncoplanar coherent beams. These beams are split and pass an identical light path, and were finally focused with an objective lens, undergoing no phase shift between each other. Therefore there is no need to induce any delay line to overlap the pulses in the time domain, and also the issue of pulse overlapping in the spatial domain was much simplified [168].

4.6.3 FCC Structure Realized with Four-Beam Interference

In principle, by increasing the beam number, even complicated 3D lattices can be produced. However, this not only brings about difficulties in arranging and aligning optical components, but also challenges the material properties. In order to completely remove the less polymerized resin, it is desired that the light intensity contrast in the interfering field should be as large as possible. The sub maxima caused by many beams would be problematic in developing. Campbell et al. [37, 169] design FCC lattices by elaborately arranging four beams. Figure 40 shows the calculated FCC lattice pattern. In Fig. 40(b) the four equal intensity beams propagate along (i) [2,0,1], (ii) [$\bar{2}$, 0,1], (iii) [0, 2, $\bar{1}$,] and (iv) [0, $\bar{2}$, $\bar{1}$] directions respectively. An intuitive description is that two beams are incident from the bottom of the substrate in the same incident plane, each of which has an incident angle of 63.4°; the other two beams are from the substrate top with their incident plane perpendicular to that of the bottom beams and each has the same incident angle. Adoption of a low-index reciprocal lattice vector allows close packing of the primitive units, giving rise to a lattice constant of $\sqrt{5}\lambda/2$.

If a suitable set of high-index wavevectors are used, relative large lattices are possible. For example, an FCC with a lattice constant of $3\sqrt{3}\lambda/2$ is generated (Fig. 40a) by introducing four beams from (i) [1,1,1], (ii) [5,1,1], (iii) [1,5,1], and [1,1,5] directions, or in another word, four beams are introduced from and convergent to a single side of substrate, three of them with interangle of 65 ° and three-fold symmetrically surrounding the central beam. The plane containing two of the three side beams forms a 13.3° dihedral angle with the substrate. As expected from the theoretical calculation, lattices corresponding to the above two beam configurations were success-

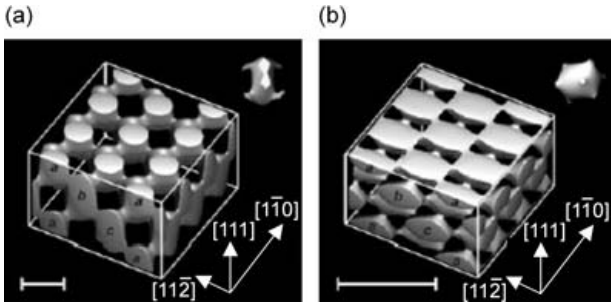

Fig. 40 Calculated constant-intensity surface in 4-beam laser interference patterns. The primitive units (contents of Wigner-Seitz unit cell) is shown inset in each case. **a** Scheme-1, high-index beam vectors interference, producing pattern of 922-nm lattice constant. **b** Scheme-2, low-index beam vectors interference, producing FCC pattern with 397-nm lattice constant. In both case, the use of 355-nm YAG laser was assumed. Scale bars: 500 nm

fully photopolymerized into a SU-8 photoresist using the third harmonic of a YAG laser, 355 nm.

Laser polarization is essential for designing interference patterns [169]. The lattice in Fig. 41a is created by interfering four beams with identical polarization so that all of them interact with each other. However, if the polarizations of the beams are (i)$\perp$(ii) and (iii)$\perp$(iv), and (i)$_{\parallel}$(iii) or (i)$_{\parallel}$(iv), light of perpendicular polarizations don't interact with each other, so that the interference pattern is a simple addition of two sets of two-beam interference planes (Fig. 41b). In both cases, the Scheme 1 beam geometry in Fig. 40 was utilized.

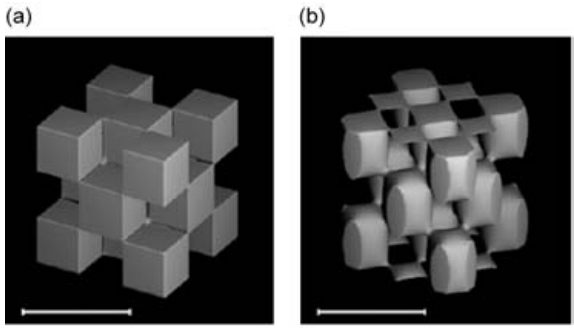

Fig. 41 Calculated interference patterns with FCC symmetry produced by four beams with different polarizations. The 500 nm scale bars correspond to a laser wavelength 355 nm; the lattice constant is 397 nm. **a** all 4 beams have identical linear polarization, and **b** beam arrangement corresponds to those in Scheme 1, but with polarizations (i)$\perp$(ii) and (iii)$\perp$(iv), and (i)//(iii) or (i)//(iv)

4.6.4
Application to Two-Photon Photopolymerization

All of the fabrication examples [39–41, 170–172] given above are from single photon photopolymerization. The same process is applicable to two-photon fabrication, which is, however, hindered by two issues intrinsic to TPA. First, TPA generally needs ultrashort laser pulses, typically femtosecond lasers. The short pulse width is always accompanied by a broad emission spectrum due to the frequency-time uncertainty. The wider spectral width sharply reduces the coherence length (l_c). A transform-limited 100 fs pulse possesses only around 40 μm l_c, as estimated by $l_c=0.624\lambda^2/(\Delta\lambda_{FWHM})$. This sharply contrasts with a nanosecond laser, which has a coherence length of centimeters, and a CW laser where it is even longer. In single photon multi-beam interference, the limiting factor of the achievable thickness is the power attenuation due to the linear absorption of resins. TPA can record deeper due to its penetration capability, but this merit is counteracted by the short coherence length. A solution is the use of picosecond lasers, which should have coherence lengths of the order of millimeters, and their transient high power may be still sufficient to launch TPA.

The second issue is that TPA uses a wavelength double that needed for linear absorption. TPA is helpful in reducing holographic linewidth, but the doubled wavelength becomes a detrimental factor in reducing the structure periodicity. We noted in 4.6.3 that the PhC lattice constant is proportional to the interference laser wavelength, $\sqrt{5}\lambda/2$ and $3\sqrt{3}\lambda/2$ for Schemes 2 and 1 respectively. Recording with a 355 nm laser gives rise to lattice constants of 397 nm (Scheme 2) and 922 nm (Scheme 1), while the corresponding two-photon writing produces lattice constants of 794 nm (Scheme 2) and 1844 nm (Scheme 1).

The spatial distribution of the square of light intensity is steeper than that for the light intensity itself. Therefore two-photon polymerized structures are relatively easy to develop due to a sharper contrast between the maximum and minimum of polymerization. To use this advantage, a picosecond pulse at visible wavelength range may be a good choice for two-photon lithographic recording.

4.7
Protein and Biomaterials

In principle, two-photon laser nanofabrication technology is applicable to any photopolymerizable material for structure fabrication, as long as the material's mechanical properties permit and if the light intensity is sufficient to launch TPA. Proteins or other biomaterials are important possible choices [172], considering the promising prospect of biocompatible micromachine or MEMS applications used in, for example, drug delivery, local treatment of

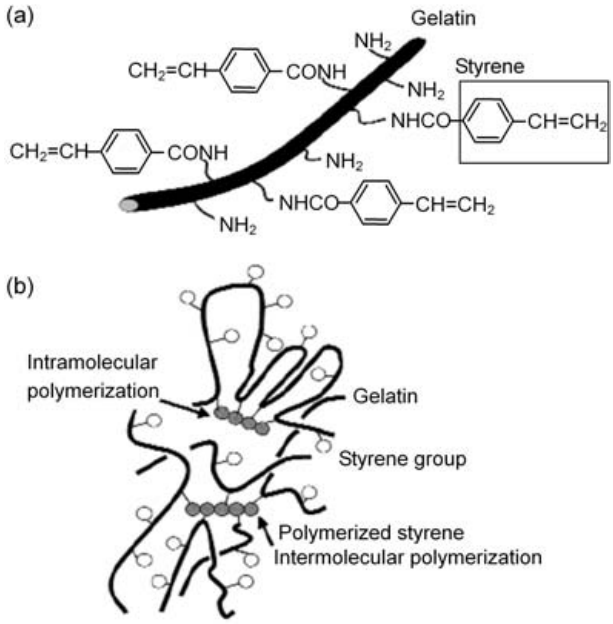

Fig. 42 Photocurable gelatin for application to femtosecond laser microfabrication. **a** Chemical structures of styrene-derived gelatin. **b** photogelation mechanism by formation of cross-linked gelatin networks via intermolecular crosslinking and intramolecular polymerization

tissue or cell, cell positioning, and biosensors. Therefore, in this section we introduce work related to this field.

Figure 42a is a multifunctional styrene-derivative gelatin, in which styrene groups are multiply attached via the amino groups of lysine residues of gelatin. It was developed [173] for photocurable tissue, and the photocuration occurs under visible light irradiation. We also succeeded in writing sub-micron-structures using two-photon-induced photogelation, for which water-soluble carboxyl camphorquinone was utilized as a photoinitiator. Upon two-photon excitation, photo produced radicals lead to the formation of a crosslinked gelatin network through intramolecular polymerization and intramolecule photocrosslinking of styrene groups in gelatin molecules (Fig. 42b).

Pitts et al. [175] explored photocuring of two different size proteins, bovin serum albumin (BSA, molecular weight MW=66 Kg/mol) and fibrinogen (MW= 340 Kg/mol). Rose Bengal (RB) was used as an initiator, whose fundamental absorption was at 550 nm. The photocrosslinking was attributed to one of the two possible photooxidation mechanisms: (i) the two-photon excited photoinitiator is excited to triplet state, and then energy transfer oc-

curs to the ground state triplet molecular oxygen, generating singlet molecular oxygen; or (ii) abstraction of hydrogen directly from a protein molecule. In the former case, the oxygen reacts with an oxidizable amino acid residue of the protein. This irreversible mechanism generates an electron-deficient protein that may react with another protein's amino acid residue at or near the protein surface. In the latter case, direct hydrogen abstraction from the protein molecule by the photoexcited initiator allows for direct protein cross-linking. A further experiment shows that at low RB concentration, the fibrinogen grows 2~10 times faster than for BSA, which was interpreted as being because the fibrinogen has a relatively larger molecular weight, so fewer cross-linking reactions are needed to reach optically detectable dimensions. However, this effect doesn't hold true when the RB concentration is sufficiently high to negate the effects of photo activator diffusion or fewer protein reactive sites. The existence of a marked dependence on the RB concentration for both BSA and fibrinogen implies that no dye is produced during the photocuring. This supports the hydrogen abstraction mechanism because in the first mechanism, the dye is recoiled by subsequent optical pumping.

Both of the above two researches targeted the drug delivery devices or sustained release devices. It is believed that the ability to fabricate with both hydrogel materials and proteins at milli-, micro- and nanoscales would expand the utility of such devices that are currently millimeter-sized. Critical to creating useful release devices is the entrapment of target molecules. For two-photon curing, the task was simplified to include only the molecules of the fabrication solution. Pitts et al. find that alkaline phosphatase maintains bioactivity after entrapment in the protein structure. As sustained release devices, it is found the rates of diffusion of fluorescently labeled dextrans (10 and 40 kDa) from a two-photon fabricated BSA matrix vary with molecular weight and are linearly correlated with cross-link density. The release half-life of 10 kDa dextran-TMR from a BSA microstructure is equal to or less than 6 minutes while that for 40 kDa dextran-TMR is 25 minutes.

4.8 A High Efficiency Photoacid Generator and its Application to Positive-Tone Microfabrication

4.8.1 Large-δ and High Quantum Yield Photoacid Generators

We introduced the application of conventional UV photoacid generators (PAGs) such as diaryliodonium and triaylsulfonium cations to two-photon microfabrications in 3.3.7. However, the TPA cross-sections for these initiators are generally small, of order $\delta \sim 10 \times 10^{-50}$ s cm^4/photon. As for radical polymerization, a high-efficiency 3D fabrication would benefit from large δ

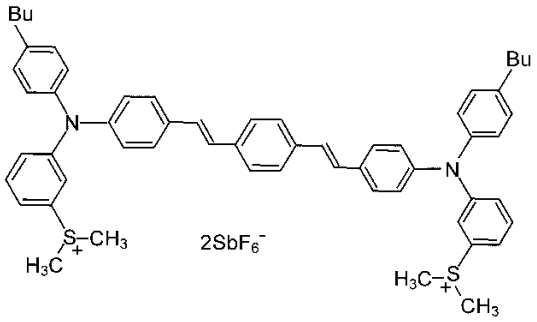

Fig. 43 Chemical structure of BSB-S_2

and large photochemical quantum yield, ϕ_{H+}[1–5, 104–106]. The problem in designing a large-δ molecule is that most of them have excited states of relatively low energy due to extended conjugation, which is insufficient to afford the energy for direct bond cleavage. Zhou et al. [176] use the strategy of photoinduced electron transfer from TPA dyes to covalently linked sulfonium groups. They realized [177] that (i) two-photon-excited bis(diphenylamino)-substituted bis(styryl)benzene dyes (δ~800×10^{-50} s cm^4/photon) should have ample reducing power to transfer an electron to the S-C σ^* orbital of a dimethylaryl sulfoium cation, which would cleave the S-C bond and generate acid; and that (ii) triacrylamine dialkylsulfonium salts are photosensitive in the near-UV region and generate protons with a photochemical quantum yield ~0.5. A compound, BSB-S_2, was synthesized and characterized (Fig. 43) [177].

A solution of BSB-S_2 in acetonitrile become acidic after irradiation into the lowest energy absorption band, and the quantum efficiency of proton generation was determined to be ϕ_{H+}~0.5±0.05. Measured from the two-photon excitation spectrum, the TPA cross-section of BSB-S_2 was significantly larger than conventional PAGs, and was determined at δ>100± 10^{-50} s cm^4/photon for 705–850 nm, with a peak at 710 nm, where δ~690± 10^{-50} s cm^4/photon. BSB-S_2 was proved to be a high efficiency initiator for photopolymerization of epoxide monomers. In addition to its use in negative type 3D fabrication similar to radical photopolymerization, another merit of photoacid generation is that it permits positive tone microfabrication based on polymer degradation.

4.8.2 Positive Tone Microfabrication

In mechanical manufacturing, components can be produced either by means of additive or subtractive processing. Microfabrication follows the

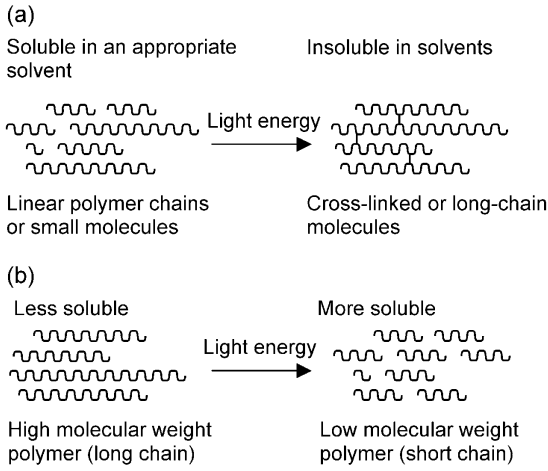

Fig. 44 Microfabrication using negative and postive photopolymers. **a** photopolymerization, and **b** photo-depolymerization

same logic, and negative and positive photopolymers are useful for each technical route. Photopolymerization is a typical additive-type fabrication method, where exposed volume becomes insoluble in post-exposure development. In a positive type fabrication, the precursory photopolymer is insoluble to a developing solvent but the exposure volume become soluble and removable from the matrix. Figure 44 shows the two schemes.

Zhou et al. [177] use a random copolymer of tetrahydropyranyl methacrylate (THPMA) and methyl methacrylate (MMA) polymer doped with BSB-S_2 as the PAG for microfabrication. At the laser focal spot, the THPMA groups were converted to carboxylic acid groups due to photogenerated acid-induced ester cleavage reactions, and were therefore rendered soluble in aqueous base developer. Figure 45 shows the 3D microstructure produced by this method. By two-photon fluorescence imaging, it was found that the buried channels are open and a continuous connection was made between the two cavities.

Different from two-photon photopolymerization, fabrication based on positive polymers should be called two-photon depolymerization. It could be an important complementary technology in 3D microfabrication, particularly those with many buried structures like those in a micro fluid system.

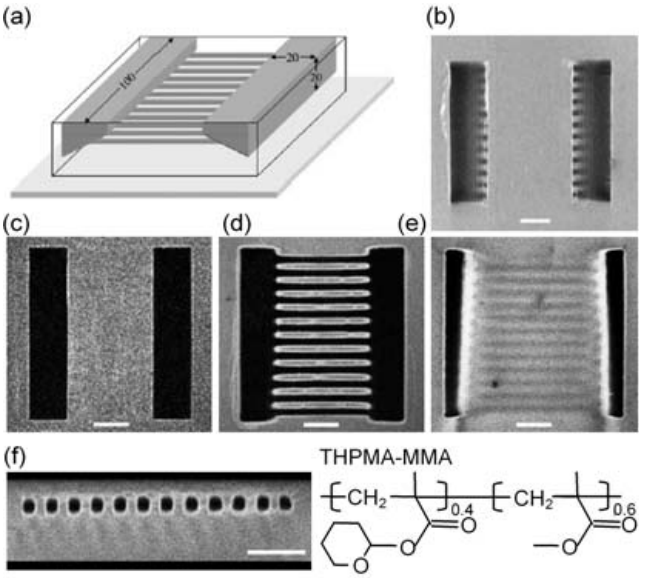

Fig. 45 A 3D microchannel structure produced by two-photon exposure of BSB-S_2 in THPMA-MMA. A 50-μm-thick film of 4 wt % BSB-S_2 in THPMA-MMA was exposed in the pattern of the target structure at 745 nm with tightly focused (1.4 N.A.) 82-MHz, 80-fs pulses from a Ti:sapphire laser at an average power of 40 mW and a linear scan speed of 50 μm/s. After irradiation, the film was baked for 1 min at 90°C. The target structure was then obtained by dissolving the exposed resin in aqueous 0.26 M tetramethylammonium hydroxide. **a** Target structure consisting of two rectangular cavities (width, 100 μm; length, 20 μm; depth, 20 μm) with sloped side walls that are connected by 12 channels (length, 50 μm; cross-section, 4 μm by 4 μm) lying 10 μm below the surface and spaced apart by 8 μm (center to center). **b** Scanning electron micrograph of the final structure, viewed normal to the substrate. (**c** to **e**) Two photon fluorescence images of the final structure (viewed normal to the substrate) **c** at the surface of the film, **d** 10 μm below the surface, and **e** 19 μm below the surface. **f** Two-photon fluorescence cross-sectional image of the buried channels. The scale bar in **b** through **f** corresponds to 20 μm. [177]

5 Applications

Two-photon photopolymerization, a micro-nanotechnology still in its infancy and a subject of active research, has potential use in fields such as photonics, optoelectronics, biology, micromachines and MEMS, and so forth. Among many, here we introduce applications that already have proof of concept.

5.1 Photonic Crystals and PhC-Based Optoelectronic Devices

Photonic crystals (PhCs) [92–94] are microstructures with a periodical distribution of refractive indexes. They are the optical analogue of semiconductors, where a bandgap is open due to the electron wave modulation by periodic Coulombic potential. In a PhC, the multiple interference among waves scattered from each primitive unit may lead to a frequency region, called a *photonic bandgap* (PBG), where light propagation in all directions is forbidden. Incident from outside, PhC is highly reflective at the bandgap wavelength; and inside the structure, light emission will be suppressed or forbidden. These features provide a novel scheme for high-efficiency optoelectronic devices such as waveguides with sharp bends and low-threshold lasers, for new nonlinear optical applications such as superprisms, and for the enhancement of nonlinear processes like harmonic generation.

The period of PhCs should match the wavelength of interest. For application in the visible and NIR communication wave range, the lattice constant is expected to be several hundreds of nanometers. This length scale is not large enough to use mechanical processing like hole drilling, and it is not small enough that well-developed semiconductor expitaxial growth technologies like MOCVD or MBE are applicable. Although excellent performances have been theoretically predicted [92–94], realization of well-defined 3D lattices is technically challenging. Up to now, a number of technologies have been explored. Self-organizing colloidal particles [96–98], and filling the interval to form a reverse opal [178] have been conducted using various materials; hole drilling has been carried out using lithography with an ensuing wet etching, as has electrochemical etching of porous silicon [179], and electron beam lithography plus dry etching [180]; log pile structures were implemented by sequentially stacking micromachined 2D grids of silicon or gallium arsenide [181], and by repeatedly deposition and etching of silicon [182]. None of the above technologies are ideal. The self-organization technology tends to give close-packing lattices, and therefore leaves little room to tailor the lattice type; almost no satisfactory 3D lattices have been created from hole drilling technologies due to the restraint of the small depth-to-width ratio; semiconductor processing methods are expensive and complicated, and haven't produced structures with more than a few periods. Compared with above technologies, two-photon photopolymerization has the intrinsic capability to tailor 3D structures of arbitrary lattices, which will open the door to PhC-based polymer optoelectronic devices.

5.1.1 Two-Photon Polymerized PhC Structures and Bandgap Effects

There are at least two advantages to fabricating PhCs using two-photon photopolymerization technology. First of all is the potential to produce PhCs of arbitrarily designed lattices. PhCs of varied lattice types, lattice constant, and filling factors are realizable just by scanning different CAD patterns. This simplicity in fabrication permits a systematic study of PhC physics and suits various requirements for a practical system. Secondly, there is the diversity of usable materials and functions. The progress of molecular material engineering has made it possible to synthesize polymers with performances similar to or better than their inorganic counterparts. By introducing functional groups to unsaturated monomer or oligomer units in a molecular structure, or just by doping the functional polymers into known photopolymerizable materials, optical, electronic, magnetic, and mechanical functions can be imparted to devices.

Sun et al. [15] were first to propose using two-photon photopolymerization technology for creating 3D PhCs, and they observed a pronounced PBG effect. They used a commercially available resin, Nopcocure 800 (San Nopco), consisting of a radical photoinitiator and acrylic acid ester. The linear absorption of the resin extends from the UV to around 370 nm. Due to a low TPA cross-section, 10^{-56}cm^{4}s photon^{-1}, the fabrication was conducted using regeneratively amplified laser pulses. Shown in Fig. 46a is a schematic illustration of the log-pile structure [183]. It consists of parallel rod layers with a stacking sequence that repeats every fourth layer with a period Λ. Within each layer, the rods are arranged in a simple 2D array with rod spacing a. The rods in the next layers are rotated by an angle α with respect to rods in the previous layer. The array in the second neighboring layer is shifted by half the spacing a relative to rods in the first plane in a direction perpendicular to the rods. Different variations of logpile structures were realized by parameter assignment of a, c (period along the packing direction) and α (60~90°). The general logpile structure has the symmetry of a face centered tetragonal (FCT). When $\frac{c}{a} = \sqrt{2}$, the lattice can be derived from an *FCC* unit cell with a basis of two rods.

Since the generally used resins are just optical adhesives, organic solvents like acetone or methanol work quite well for developing. However, compared with the micromechnical structures as described previously, photonic crystals consist of holes of high aspect ratio. Therefore a much longer soaking duration is needed for complete removal of unsolidified components. Figure 46b is the top view optical microscope image of a fabricated logpile structure. The same structure, after being cleaved and coated with a thin-layer of Au film, was observed under SEM (Fig. 46c). It is shown that a well-defined 3D spatial structure had been achieved, and the rods were arranged

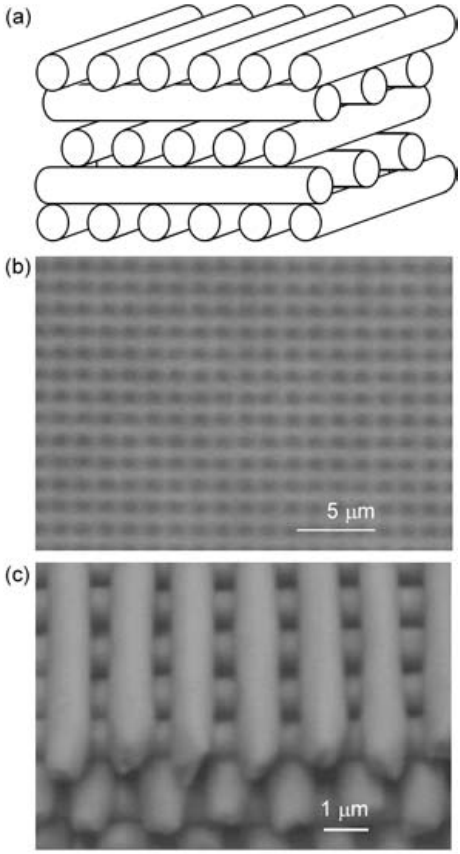

Fig. 46 Logpile PhC structure. **a** an illustration, and **b** a structure fabricated using two-photon photopolymerization of resin, top-view optical microscopic image, and **c** side-view SEM image

regularly in the same plane with half a period offset to the nearest layers with the same orientation.

To reveal signatures of PBG, transmission spectra of the PhC samples were measured using a Fourier-transform infrared (FTIR) spectrometer combined with a microscope imaging system. Plotted in Fig. 47 are the transmission characteristics of 20-layer logpile structures with different in-plane rod spacing: 1.2 μm, 1.3 μm, and 1.4 μm. Each sample has a dimension of 40 μm×40 μm, all fabricated under the same laser pulse energy, 90 nJ/pulse, giving rise to a lateral rod diameter of 1.0 μm. All spectra were normalized to the transmission of the uniformly solidified bulk resin.

The transmittance dips under normal incidence occur at wave numbers of 2550, 2510, and 2450 cm^{-1}, respectively. The increase of the wavelength of

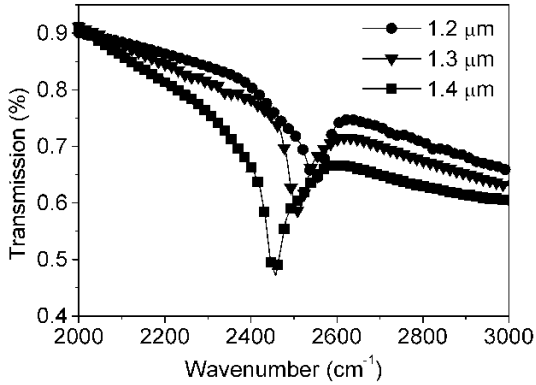

Fig. 47 Transmission spectra of two-photon polymerized logpile PhC structures with different in-plane lattice constants

transmission minima versus lattice constants is an expected feature since the frequency scales as $1/n$ in a medium of refractive index n. The mean dielectric constant increases with the filling ratio of resin and the latter is roughly estimated according to $f=\pi r/4d$, where r and d are the rod radii and the inter-rod spacing. An average attenuation of 1.3 dB per unit cell was not satisfactory. Several factors should be responsible for this: fluctuation of rod diameter arising from the shrinkage of polymerized resin and from ambient

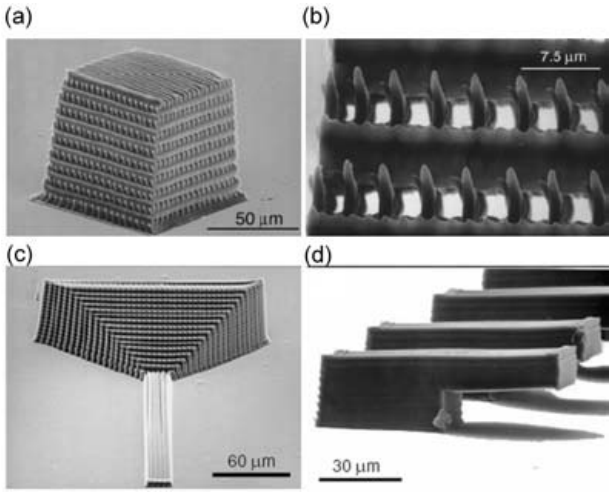

Fig. 48 PhC structures produced by photopolymerizing a resin with high-efficiency radical initiators. **a** SEM image of the entire structure, **b** magnified top view, **c** tapered PhC waveguide, and **d** array of cantilevers, as example micromechanical devices

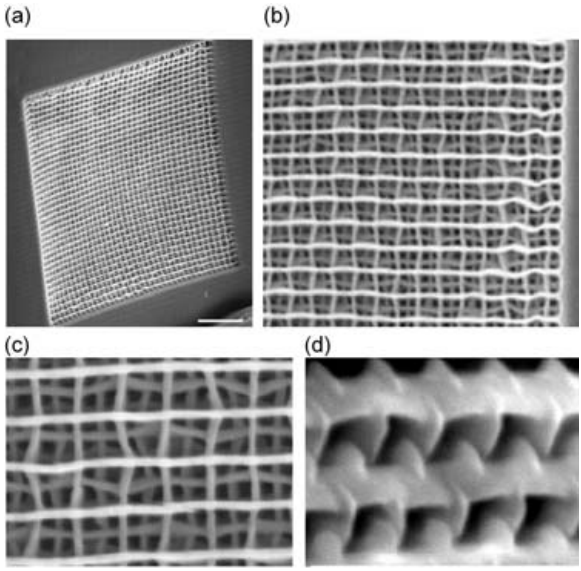

Fig. 49 SEM image of logpile structure with 500-nm layer spacing and 1.5 μm in-plane rod spacing. **a** Entire view of the 60 μm×60 μm structure, scale bar 10 μm. **b**, **c**, and **d** magnified top views

vibrations, and most importantly, the incomplete removal of unsolidified or low-degree polymerized resin at the bottom layers.

A similar logpile structure (Fig. 48a) was reported by Cumpston et al. [22] soon after the first demonstration of working photopolymerized PhCs. Although there is no observed bandgap effect, this work is known for use of highly efficient two-photon photoinitiators as introduced in 3.3. The resin they adopted consisted of a polymer binder, a crosslinkable acrylate monomer, and D-π-D chromophore **8** or **9** (Fig. 6) as the photoinitiator. They tuned laser pulses of 150 fs duration at a repetition frequency of 76 MHz to wavelengths near the TPA peak of the initiator. Figure 48a and b are views of the logpile structure they fabricated. Figure 48c shows a tapered optical waveguide, of which the cross-section varies along the length from a 100 μm×100 μm square aperture to a 2 μm×10 μm rectangular aperture. Tapered optical waveguides have the potential to reduce optical loss in the coupling of waveguide components with disparate cross-sections.

In the work of Sun et al. [15, 17], the PBG appears at around 4 μm, which is mainly determined by the periodicity along the light propagation direction. By reducing the lattice constant, it is possible to move the bandgap center to shorter wavelengths. Straub et al. [184] observed a bandgap effect at 1.5 μm ~ 2.3 μm from logpile structures of layer spacing ranging from 350 nm to 500 nm. Figure 49 shows SEM images of a 40-layer 60 μm×60 μm

structure scanned with 60 μm/s of 540 nm, 140 fs, 76 MHz and 1.0 mW laser pulses. Subsequent layers were stacked at intervals of 500 nm and with an in-plane rod spacing of 1.5 μm. Because the rods were produced by single scanning, instead of multi-lateral scanning [15, 17], their cross-section was measured at 860 nm×280 nm, reflecting the shape of two-photon PSF.

5.1.2 Defects for PhC Functions

Up to now most successful unadulterated and defect-contained PhCs have been fabricated in semiconductors [185, 186]. To mention just a few examples, line, air-bridge, and bent waveguides, as well as low-threshold lasing have been reported. Recent progress in functional molecular synthesis stimulates the development of organic photonics. Organic structures employing various geometries, such as microdisk, microring, sphere, vertical-cavity surface-emitting, distributed Bragg reflection (DBR), distributed feedback (DFB), and fiber grating, have been used in lasers and amplifiers [187]. One problem that was encountered in designing organic LD and light emitting diode (LED) structures is the inherent absence of mirrors that provide positive feedback for lasing. In semiconductor structures cleaved facets play this role. Although this problem can be partly solved using DFB and DBR structures, the emission efficiency is still unsatisfactory. Therefore it is interesting to investigate whether the use of PhCs provides a novel mechanism to circumvent this issue.

Like the role of impurities in semiconductors, defects could be essential for tailoring PhC properties. For instance, PhC-based waveguides can guide light through sharp turns with negligible power loss, which would enable photonic integrated circuits. Embedding an optically active medium into a PhC structure inhibits light emission into undesirable modes, and allows the realization of highly efficient optical emitters, such LEDs and thresholdless LDs. The essential requirement to reach this end is the possibility of forming waveguide channels and microcavities by introducing defects into periodic structures. In the two-photon photopolymerization method, 3D structures are written on the voxel basis. This gives rise to the feasibility of individual addressing, that is, that each voxel could be produced in the desired way, implying that not only complete periodic structures, but also defects – either missing rods or extra portions – could be created.

PBG effects have been observed in two-photon polymerized PhCs [15]. The research was naturally extended towards the formation of planar microcavities by introducing defects into the logpile PhC (Fig. 50a). The fabricated structure [17] consisted of 20 layers of rods. The planar defect was introduced by skipping the exposure of every other rod in the tenth layer, located in the middle of the PhC structure. This was simply accomplished by closing the laser beam while drawing the particular lines.

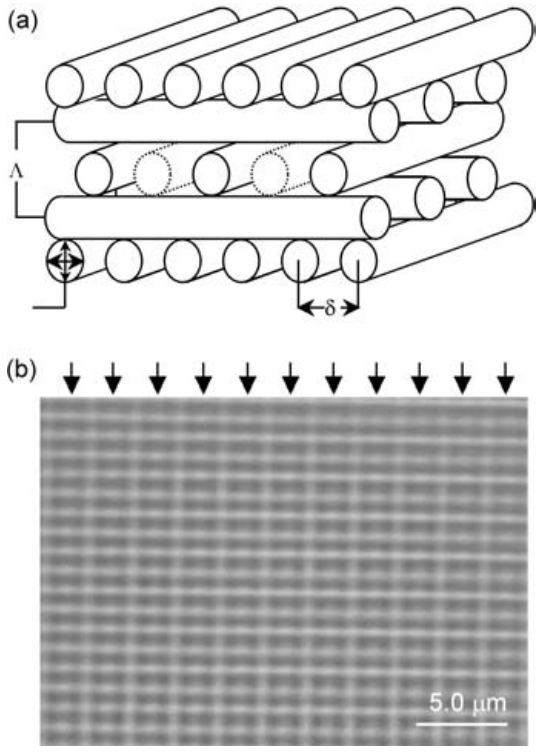

Fig. 50 Logpile PhC structure containing planar defects. **a** an illustration of the concept, and **b** optical microscopic image of the fabricated structure. The arrows indicate where no rods exist due to exposure skipping

Figure 50b shows an optical micrograph of the defected layer. The positions of the missing rods are indicated by the arrows. The structure has a rod diameter of $2r$~0.8 μm (assuming a cylindrical rod shape), in-plane period δ~1.3 μm, and rod length L~40 μm. For the PBG midgap wavelength $\lambda_M \approx 4.0$ μm, so the geometric thickness of the defected layer $2r$~0.8 μm is somewhat smaller than $\lambda_M/2$, indicating that localized modes penetrated significantly into the PhC mirrors.

Figure 51 shows the transmission spectra of the investigated sample (solid line), and the reference sample without defect (dashed line) for unpolarized light along the stacking direction <001>, as indicated schematically in the top inset. In the reference sample, a pronounced transmission dip at 3.98 μm with a spectral width of approximately 91 nm (FWHM) is seen. The dip magnitude also implies the existence of a photonic pseudogap rather than full PBG in this structure, as can be expected in the case of a relatively low refractive index contrast. This assumption is also confirmed by our numerical simulations (see description below). In spite of incomplete PBG, sig-

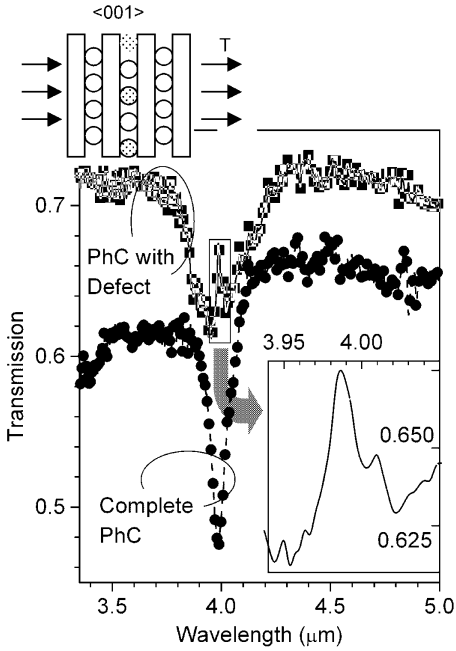

Fig. 51 Transmission spectra of the defect-free and defect-contained PhC logpile structures. The appearance of a sharp peak was assigned due to PhC microcavity resonance

natures of evolving defect modes can be nevertheless seen in the defected sample. The transmission spectrum of this sample reveals a similar, but slightly broader PBG transmission dip at the same spectral position, and a pronounced transmission peak within it.

The physical origin of the peak can be sketched in terms of multiple reflections of light between two PBG mirrors surrounding the defected layer, forming a planar microcavity. Hence, the peak marks the formation of the microcavity resonance. Light trapping by the cavity is usually characterized by the quality factor $Q=\omega_0 E/P$, where E is the energy stored in the cavity, ω_0 is the resonant frequency, and $P=dE/dt$ is the dissipated power. The transmission data allows us to estimate the quality factor using the expression $Q=\lambda_R/\Delta\lambda\approx 130$, where λ_R and $\Delta\lambda$ are the peak center wavelength and width, respectively, assuming the measured values of $\Delta\lambda=29.8$ nm (FWHM) and $\lambda_R=4.01$ μm. It is helpful to note here that semiconductor microcavities formed from high refractive index materials may have quality factors as high as 1600. In our case, relatively low Q value means that the planar defect exerts a localizing perturbation on the light modes at the midgap, but their spatial spreading and escape from the defected region is also significant. As a result, the effective mode volume exceeds the geometric volume of the de-

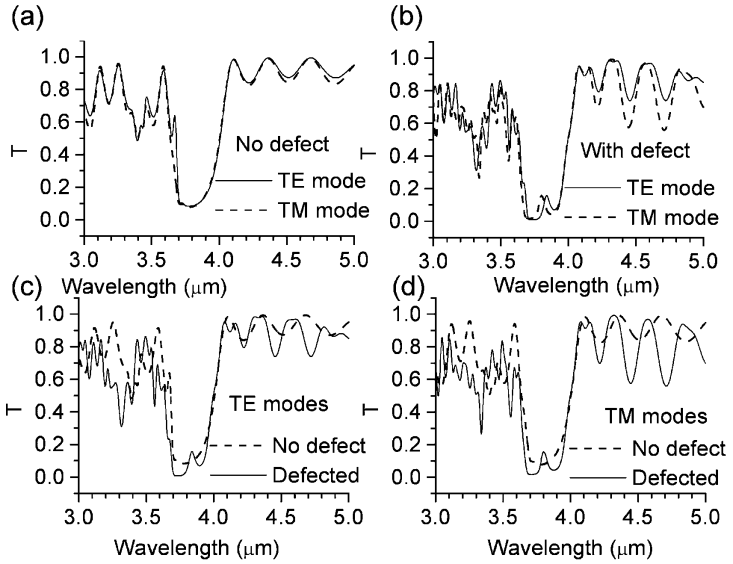

Fig. 52 Transmission spectra of the defect-free and defect-contained logpile PhC structures for different detecting laser polarizations. The existence of defect modes were theoretically proved

fect and may even become comparable to the entire illuminated volume of the sample.

Formation of the PBG and microcavity resonance was also confirmed by numerical modeling. Figure 52 shows the transmission spectra of reference (**a**) and defected (**b**) samples, calculated using the transfer-matrix technique. Transmission for TE (broken line) and TM (solid line) linearly polarized modes was considered separately in anticipation that the absence of some oriented rods in the defected sample would result in different conditions for the propagation of TE and TM modes. The calculated transmission spectrum of the reference sample is shown in Fig. 52a.

Spectral positions of the calculated transmission dips are close to those observed experimentally, but the calculated dips are somewhat deeper and broader (gap to midgap ratio is about 9%). A similar result is obtained for the defected sample (Fig. 52b), but in this case a distinct peak within the dip, marking the microcavity resonance, is seen for each polarization. The peaks are centered at 3.801 μm (TM) and 3.838 μm (TE), have Lorentzian line shapes, and almost identical amplitudes (about 16%) and Q-factors (about 85). As expected, there is a slight displacement between the peaks of different polarizations due to the anisotropic nature of the defect. Transmission at the maximum of the resonance peak is about 16%. Altogether, the numeric simulations qualitatively reproduce the experimental data, routine-

ly yielding PBG at slightly shorter wavelengths than the measured ones. This is likely to be related to our assumption about cylindrical shape of the rods, whereas in reality they are oval-shaped, with elongation along the layer stacking direction, resulting in higher lattice constant, and scaling up of the PBG center wavelength.

5.1.3 Photopolymerization Created Waveguide Channels in PhC Templates

Defects, essential to PhC functions as discussed in 5.1.2, may be produced as an intrinsic part of PhCs in the structural design and fabrication processes if PhCs are fabricated by direct laser writing. However, self-organization of colloidal particles and multi-beam interference, the two technologies which are promising for industrial manufacturing, have no individual addressing capability. Hence, how to induce defects into perfect periodic lattices is an important issue to solve. A promising method is writing defect structures in ready PhC templates using two-photon photopolymerization. In this method, liquid resin is infiltrated into the interval of a PhC structure, and then a particular pattern could be written, provided that the PhC materials are transparent to the fabricating wavelength. After washing out unpolymerized resin, the polymerized structure would be connected and retained inside the original lattice (Fig. 53a) [188].

Lee et al. [189] realized the above idea on PhCs produced by self-assembling colloidal particles. The colloidal crystals were achieved by gravity sedimentation of 1.58 μm spherical silica particles from a solution of dimethylformamide (DMF) and water. They infiltrate a precursor solution of 0.1 mM of the initiator, 9-fluorenone-2-carboxilic acid, and 0.1 M of the coinitiator, triethanolamine, in the monomer, triethylolpropane triacrylate. Polymerization was conducted using 780 nm, 80 fs, 82 MHz laser pulses. Figure 53a illustrates the procedure of their experiments. To reveal information about the polymerized structure inside the colloidal template, a Rhodamine solution in DMF was filled into the colloidal assembly after the removal of unsolidified liquid.

Figure 53b shows the single-photon fluorescence image of the entire polymerized structure; a portion of it was magnified and is shown in Fig. 53c. The lack of fluorescence in the dark region indicates that the particle interval there was sealed by resin and prevents the dye penetration. The existence of polymerized features was further confirmed by the SEM image of Fig. 53d, taken after the silica particles were removed by chemical etching in HF acid.

The defined-defect-contained colloidal crystals could be utilized as a mold for producing inverse PhC structures with ideal lattices and with sufficiently high refractive index contrast. The artificially induced defects could be removed by further processing like selective chemical etching or sinter-

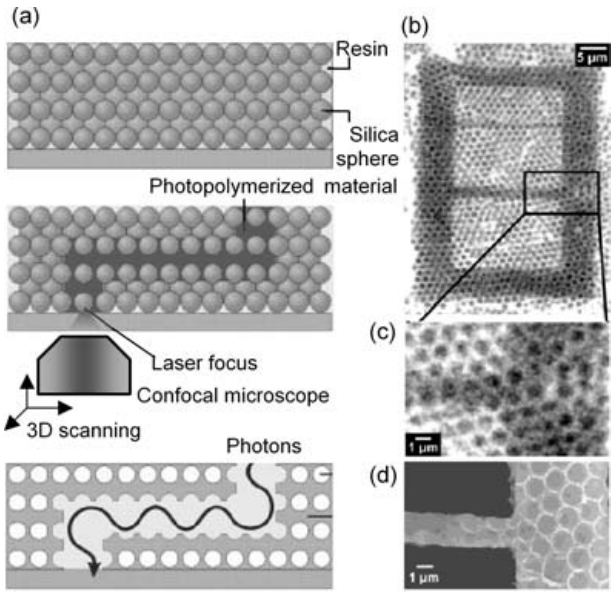

Fig. 53 Defect induced inside a colloidal PhC template by photopolymerizing the immersed resin. **a** Schematic of the experimental procedure and its future use, **b** fluorescence image of the PhC structures that contain the polymerized defect, **c** magnified view of **b**, and **d** SEM image

ing. This technology may broaden the use of colloidal PhCs [189] or multibeam interference polymerized PhCs due to the new possibility of artificially designing defects.

5.2 Functional Micromachines and Microelectromechanical Systems and their Optical Actuating

A number of micro components have been fabricated, shown in Figs. 11, 15, 45, 48d, as well as in Fig. 54, a micro-gearwheel pair (Fig. 54a), a micro-gearwheel affixed to a shaft (Fig. 54b), a microchain (Fig. 54c), and a human skeleton (Fig. 54d).

These structures are good proof of the fabrication capability of two-photon photopolymerization technology. Even more complicated devices can be produced, which should be composed of two types of components classified according to their functions, static parts for support, connection or confinement, and movable parts. Both need precise shaping, positioning and jointing during photofabrication. For movable components, an essential issue to address prior to fabrication is finding a suitable actuating mechanism. Appropriate electric, optical, thermal, magnetic, and chemical effects need to

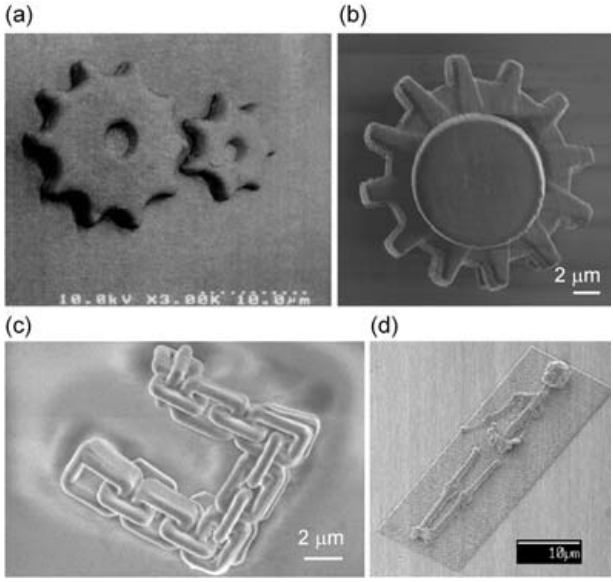

Fig. 54 Micromechanical structures produced by two-photon photopolymerization **a** a microgearwheel pair, **b** a microgearwheel affixed to a shaft, **c** a microchain, and **d** a micro human skeleton

be found to achieve this end. Electrically controlling micro systems, the requirement of MEMS, is most desirable, however, there is a long way to go before introducing conductive polymer into structures and integrating polymer devices on an IC-contained semiconductor chip or developing polymer ICs. Optical force provides a simple solution, which is the currently most practical mechanism for actuating micro-nanodevices.

5.2.1 Optical Driving of Micromechanical Devices

5.2.1.1 Optical Trapping Force

The technique of optical manipulation has been employed as a unique means of controlling microdynamics of small objects without physical contact since the pioneering works by Ashkin [190–192]. For a better understanding of the actuating mechanism, we will briefly introduce how the laser trapping force originates [190, 191]. Assume that a transparent sphere with refractive index higher than its surrounding medium is situated slightly off a laser beam axis (Fig. 55). Consider beam *a* in a typical beam ray pair *a* and *b*. The light beams undergo Fresnel reflection and refraction at the medium/sphere and sphere/medium interfaces. Forces exerted on the sphere

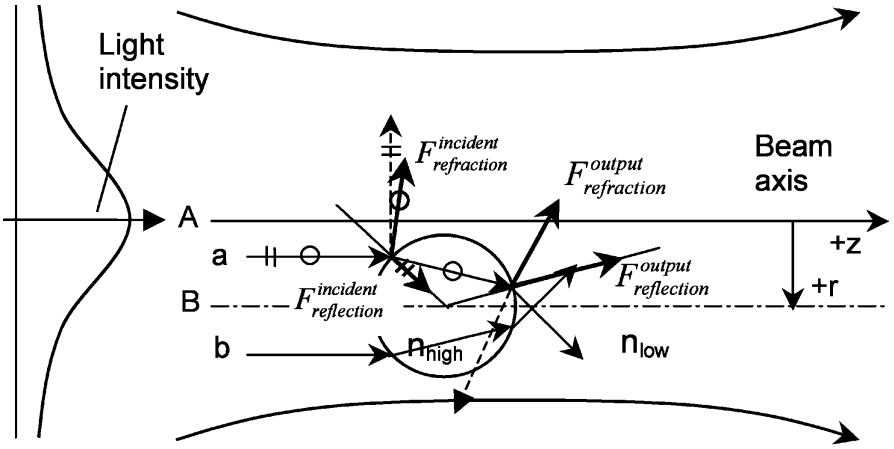

Fig. 55 The origin of optical trapping force, which provides various mechanisms for micro-nanodevice optical actuating

can be deduced from the momentum changes of photons in the beam due to elastic scattering. Four forces appear, $F^{incident}{}_{reflection}$, $F^{incident}{}_{refraction}$, $F^{output}{}_{reflection}$, $F^{output}{}_{refraction}$, as shown in the figure, and all give the bead acceleration in the beam propagation direction, $+z$. The two reflection forces at each interface are much smaller than those from refraction, and moreover $F^{incident}{}_{reflection}$ and $F^{output}{}_{reflection}$ cancel radially. The two refraction forces add radially to the $-r$ direction. Therefore the net radial force exerted by ray *a* is inward towards the beam axis direction ($-r$). The same analysis conducted for ray *b* leads to a net radial force outward. Consider the fact that a radial laser beam intensity distribution is always of Gaussian shape, so ray *a* is stronger than *b*. Summing all beams (*a*'s and *b*'s) leads to net forces interacting on the sphere in two directions. First, the bead is attracted inward towards the high intensity region. This force arises in nature from the gradient intensity distribution, therefore also called gradient force. Actually it is already known that in a nonuniform medium, for example in a waveguide, light will be guided to propagate along a high-index path. Here we see that if the media have sufficiently small mass, they can be reversibly attracted by light. The second force is simple, pushing the sphere to move along the beam propagation direction.

It is easily understood that if the light is tightly focused so that intensity gradients are nearly symmetrically constructed at two sides of the focal spot along the optical axis, the sphere is trapped at the high intensity focal spot. For an absorptive media, absorption of a large amount of directional photons (those in a laser beam) causes a net increase of momentum of the medium along the light propagation direction. In this case, the force in the laser

beam direction is also called scattering force. The laser irradiation pressure (gradient and scattering forces) as discussed above forms the basis of light actuation of micromechanical devices, which falls into three categories: windmill rotation, rotating by photon angular momentum transfer, and push-pull due to 3D trapping. In the following sections, we will describe how these optical powering approaches have been or will be applied for driving micromachines.

5.2.1.2 Windmill Rotation

Windmills rotate when facing wind, a phenomenon known since ancient times. It is not surprising that similar rotational phenomena have been frequently observed in laser-trapped particles. The rotational torque arises from the axial irradiation force as discussed above and from the asymmetrical or rotation-symmetrical shape of the particles. Actually it is believed that lifetimes of interplanetary dust grains are governed by bursting caused by solar irradiation-induced rotation! The rotation rate is proportional to the trapping laser's power, and is related to the shape of the objects and the viscous drag from the ambient medium. In a micromachine, it is important to design a device structure of helical shape and of proper rotation symmetry so that the structure could be fixed (trapped) at a suitable position and with the desired orientation, for high stability and for minimizing the friction between the rotating parts and its axle (if there is one). The translation momentum from the "photon wind" needs to be efficiently converted to the spinning momentum of the object. A number of microcomponents satisfying the above requirements have been produced by various microfabrication technologies [193–195]. Shown in Fig. 56 is a two-photon photopolymerized eight-fold rotary symmetrical rotor [195].

The resin used is a commercially-available UV optical adhesive, Norland NOA 63. A 514 nm laser was utilized as the irradiation source. When applying a 994 nm trapping laser from a LD, the rotator was first 3D trapped with its axial line coinciding with the beam axis. Two opposite orientations, whether leaf-side or shaft-side facing the laser beam, produced stable equilibrium. With the rotator position stabilized, a rotation started. Due to the large viscous drag, the rotation rate was relatively low, only several tens of Hertz. It is found that the average rotation doesn't depend on the polarization of light, consistent with the actuating mechanism: the trapping is due to the gradient force and rotation arises from momentum transfer from the photon flux, that is, the windmill effect. Scattering force is proportional to the light intensity and acts in the light propagation direction. Gradient force is proportional to the gradient of the spatial light intensity and acts in the direction of the intensity gradient. In a further experiment, the authors demonstrated that the rotor drove cogwheels. Two neighboring and slightly

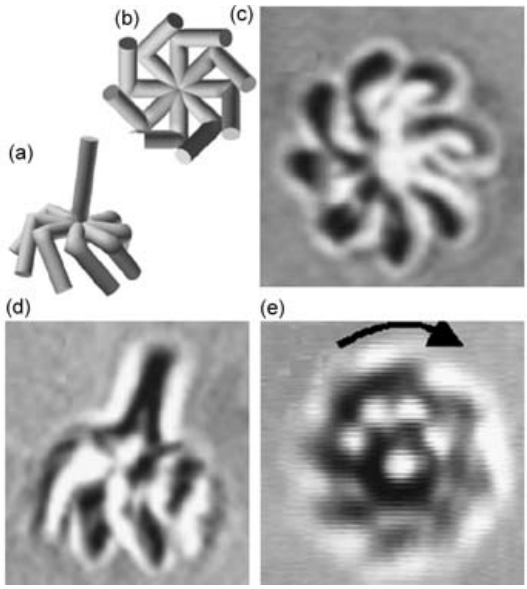

Fig. 56 Design and two-photon fabricated rotator driven by a windmill mechanism. **a** Design and **c** photograph of the rotor in an arbitrary position when it is tumbling freely, viewed from identical directions. **b** Design and **d** equivalent photograph of the rotor when it is trapped in focus but held against the cover glass thereby preventing rotation and yielding a sharp image. **e** Photograph of the spinning rotor trapped in focus and rotated by the light

touching gearwheels were affixed to separate axes that were polymerized on the substrate. When the rotating rotor was moved to one of the two engaged cogwheels, all of the three gearwheels turned.

5.2.1.3 Photon Angular Momentum Transfer

Light itself can carry angular momentum. Another machine rotating mechanism is therefore to couple the photon angular momentum to the object to be rotated. Microparticle rotating experiments have been carried out (i) using elliptically polarized light [196], (ii) by rotating the asymmetric laser beam, and (iii) using a laser beam with a helical phase structure interacting with absorptive particles [197]. When absorbing CuO particles (1–5 μm) were trapped in a focused "donut" laser beam, they rotated due to the helical phase structure of the beam. Changing the polarization of the light from plane to circular caused the rotation frequency to increase or decrease, depending on the sense of the polarization with respect to the helicity of the beam.

Although no suitable examples have been found, it is believed that these mechanisms are in principle applicable to micromachine driving.

5.2.1.4 Push-Pull Random Structures

A microparticle can be three-dimensionally trapped at the laser focus, in which case it follows the movement of the focal spot if the beam is moved. This phenomenon isn't specific to isolated particles but also applicable to a portion of an object. This implies that the entire object may be pushed or pulled in random directions if only a part of a structure is captured by a laser focus.

Compared to the last two technologies, (i) the push-pull method doesn't need designing machine to create special shapes, which is needed by the windmill driving mechanism, and (ii) the actuating isn't limited to rotating, but to any random 3D movement. As an example, a micro-oscillator system was driven by this mechanism, which will be discussed in the following section.

5.2.2 Mechanics of Two-Photon Polymerized Nanodevices

Like numerous electronic devices, such as personal computers and cellular phones, that have gained cost advantage from integrating most of their functions onto a single chip, mechanical micro-nanodevices and their integrated systems are expected to spur the next revolution in the manufacturing industry in the post-IC era [128, 129]. Therefore, developing micro-nanodevice fabrication technology and studying their performance becomes an immediate and urgent task for the research community. It is already a well-known principle in the aircraft manufacturing industry that real-size systems that are proportionally scaled up from designed models don't work. This is because the surface area and mass (or volume) of an object do not proportionally increase with dimensions; they follow different laws (square and cubic laws respectively). The same principle applies when the size of devices are scaled down to micro nanometer sizes. For example, if the feature size of a device is reduced from millimeters to nanometers, the surface-to-mass ratio increases by 10^6 times. Therefore, in the nano realm, mass and inertia are no longer important, while physical, mechanical and electric characteristics such as stress and tension, thermal transfer, phase transition, fluid phenomena, and achievable field strength abide by rules much different from current experience and would dominate [128, 129]. Without related knowledge, it is impossible to properly design, fabricate and operate nanodevices and their integrated systems.

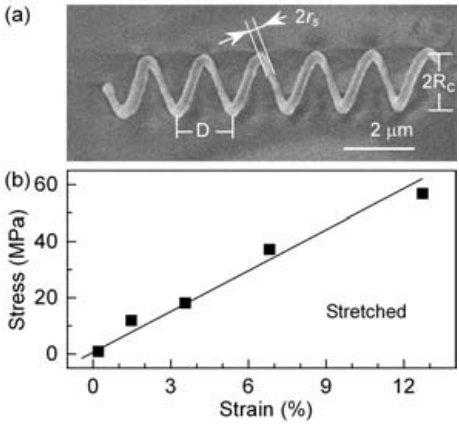

Fig. 57 **a** SEM image of a nanospring, and **b** the stress-strain plot of a resin fiber produced by UV photopolymerization

Two-photon photopolymerization has been recognized as an important method for producing micromechanical and MEMS devices. It provides a good opportunity to explore nanodevice mechanics. Sun et al. [13, 19] fabricate a nano-spring using this technology as shown in Fig. 57a.

The spring has a spiral radius of r_s=150 nm, a coil radius of R_c=1 μm, and a pitch of D=2 μm. According to these parameters, the spring constant, k, can be calculated according to the relation:

$$k = \frac{G_s r_s^4}{16 N R_c^3} \tag{23}$$

where G_s is the shear modulus of the solidified polymer, and N=4 is the number of active coils. G_s was determined from the elastic elongation of a fiber-like sample that was uniformly polymerized under UV exposure. From the stress-strain plot (Fig. 57b), the Young's modulus of the polymer was deduced to be E=0.46 GPa. Based on the relation $E=2G_s(1+\upsilon)$, G_s=0.15 GPa is obtained, where υ=0.49 is the Poisson's ratio of the material. This immediately gives rise to a spring constant of k=4.8 mN/m according to Eq. 23.

In order to know characteristics of nanodevice operation, it is critical to find an appropriate mechanism to run real-size devices. To achieve this end, the push-pull method as introduced in 5.2.1 was adopted. It is conjectured that if a spring end is trapped, moving the laser focus would prolong, compress and bend the spring itself (Fig. 58a). However, to enhance the trapping force, a microball was polymerized at the open end of the spring, and the other end was affixed to a photopolymerized anchor. Figure 58b shows the micro-oscillator system, where the spring was positioned 10 μm above the glass substrate, and had the same spiral and core diameters as those shown

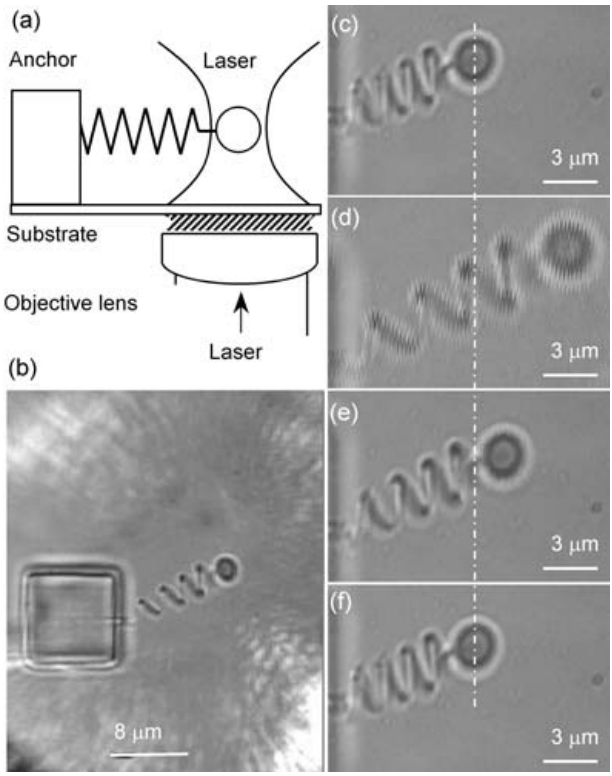

Fig. 58 A functional micro-oscillator system. **a** A designed scheme for mechanically activating the oscillator using a laser trapping force. **b** A photograph of a fabricated micro-oscillator, where the end bead was being trapped by the laser. The micro-spring is **c** in its natural state, **d** pulled by a length, **e** released, and **f** recovered to its original state 20 s after release

in Fig. 57a. The bead's diameter was $2r$=3 μm. In operation, the oscillator was kept in ethanol in order that the buoyancy would balance the gravity, eliminating the bead-substrate friction. The same laser system as was utilized for TPA photopolymerization, but with a wavelength tuned to 820 nm, was used for the laser trapping.

When the laser focus was carefully adjusted (Fig. 58b), the bead was found to be three-dimensionally trapped and able to be freely manipulated. The spring was pulled by moving the trapped bead, and then it was released by blocking the laser, initiating an oscillation. The spring was observed to be prolonged (Fig. 58d) from its original length (Fig. 58c), and restored (Fig. 58e) to its original state after the laser was turned off (Fig. 58f). Elongations of up to 7 μm over many cycles didn't cause any elasticity failure, as evidenced by the fact that the spring always returned to its original length.

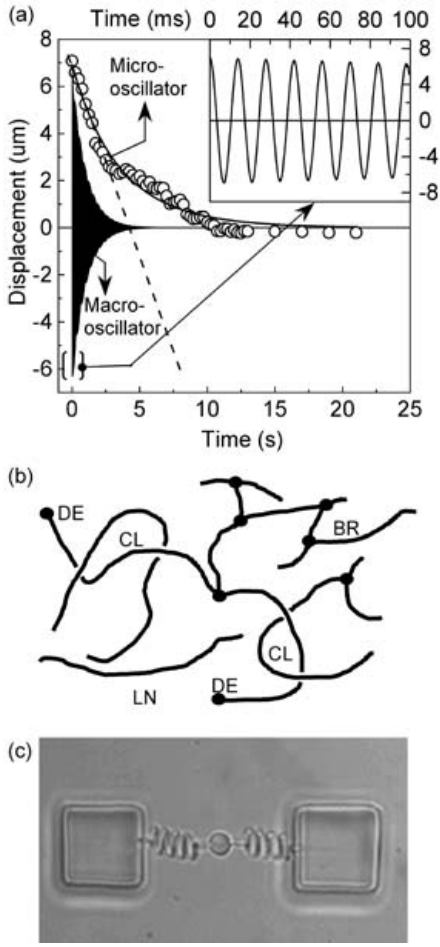

Fig. 59 **a** The bead displacement versus time for the spring recovery from the elongated state, for the micro-oscillator (circles) and a linearly 1000-times-scaled up macro-oscillator. **b** Crosslinking status of polymerized resins. **c** An oscillator consisting of a double spring

From the bead movement, it is possible to roughly estimate the spring constant. Notice that the movement isn't a reciprocating oscillation, but an over-damped one (solid line in Fig. 59a). The viscous friction should play an important role. Since the bead velocity is slow (v=1.5 μm/s at maximum, the dashed line in Fig. 59a), it is reasonable to assume the viscous resistance, a non-conservative force that is always opposed to its direction of motion, is proportional to the speed, in other words $f_{vis}=cv$, where c is a coefficient. In this case the spring oscillation can be described by the following equation:

$$\frac{\partial^2 x}{\partial t^2} + 2\mu\frac{\partial x}{\partial t} + \omega^2 x = 0 \tag{24}$$

where $\mu = \frac{c}{2m}$, and $\omega = \sqrt{\frac{k}{m}}$ is the circular frequency of the natural vibration of the spring; m (1.57×10^{-14} kg) is the mass of the bead, and k is the spring constant to be determined. The viscous resistance exerted to the bead was assumed to be $f_{vis}=6\pi\eta r v$ (Stokes Law), where $\eta=1.084\times10^{-3}$ Pa·s (25°C) is the liquid viscosity. Then by fitting the general solution with the experimental data (circles in Fig. 59a), the spring constant was derived, surprisingly, to be $k = 1 \times 10^{-8}\mathrm{Nm}^{-1}$

Here we see a five-order difference in the measured (10^{-8} N/m) and calculated (10^{-3} N/m) spring constants. To interpret the origin of the huge discrepancy, we noticed that the bead was rested before release at a stretched state of Δx=7 μm, almost the maximum of the prolongation. Calculations and dragging experiments showed that the trapping force imparted to the bead was not more than F=10 pN, which was quite consistent with reported values. Then the spring constant was directly obtained by Hook's law, $F=k\Delta x$, and was $k=10^{-6}$ N/m. This value is more reliable, since in the static state the influence from the viscosity was excluded.

For describing the motion of the micro-oscillator, we used Eq. 24, where the mass of the spring and the viscous resistance between the spring and the liquid were ignored. This may be the major source of the negative deviation of two orders, ($10^{-6}\rightarrow10^{-8}$ N/m). It is interesting to compare the performances of devices of different dimensions. When experimented in identical circumstances, an oscillator linearly scaled up by a factor of 1000 shows a typical damping oscillation (Fig. 59a), and ignoring the dimension of the spring causes a discrepancy of not more than 20%. It is the scaling effect that caused utterly different movement behaviors of nanodevices.

Materials that are assembled into micro-nanomachines are condensed in a way different from bulk matter or nanoparticles. At the mesoscale of near or sub-100 nm, the machine feature size, interactions from any single molecular bond are already less pronounced, but the collective effects of molecular arrays, orientation and molecule aggregation still play a critical role in the material's mechanical property. Like ambient factors, the material attributes themselves also influence the behaviors of nanodevices. In the calculation that used Eq. 23, physical characteristics of the spring such as modulus of elasticity and density of TPA-polymerized resin, which are determined by the degree of crosslinking, degree of crystallinity, and the value of T_g and T_m [1], were assumed identical to that polymerized under UV exposure. In photopolymers, the main contribution to the elastic strength is from the crosslinking of polymer chains. Young's modulus is related to the degree of crosslinking via $E=3nRT$, where n is the crosslink density, defined as the number of network chain segments (Fig. 59b) per unit volume, R is the gas

constant, and T the temperature. First, different from the UV exposure used for polymerizing the sample fiber, where the sample had been sufficiently illuminated and therefore fully crosslinked, in TPA fabrication the exposure duration for each voxel was short (~1 ms), which was comparable with the reaction decay time for monomer and oligomer polymerization. As a result, the polymer is more likely to be present in forms of linear (LN, in Fig. 59b) or branched (BR) chains, and a relatively small proportion is crosslinked (CL). Second, since the spiral radius is small (150 nm), the shear modulus was reduced due to a large percentage of surface volume. The surface layer is abundant in dangling ends (DE, in Fig. 59b) that are not attached to any other chain sections. G_s or E is also decreased by some weak points or segments of elasticity that were induced by the lateral fluctuation in cross-linking degree. Third, removal of remnant monomers, oligomers, and less polymerized segments by the developer, due to its relatively deep infiltration, reduced the steric hindrance, facilitating the stretching of the spring. The increase of three orders of magnitude ($10^{-6} \rightarrow 10^{-3}$ N/m) of the spring constant were interpreted by the above three factors, showing that at the nanoscale, device characteristics are also significantly affected by material status.

The ambient factors that govern the nano-oscillator operation may be minimized by actuating the spring in air or vacuum conditions. Shown in Fig. 59c is a micro-oscillator consisting of two springs, by which the bead was suspended without making contact with the substrate. Laser driving such devices may reveal much more valuable information about the mechanic and material charateristics of nanodevices.

5.2.3 Towards Photoactive Structures

The polymeric structures discussed above use passive materials; materials that have no response to light (their electron excitation status is unchanged). If photosensitive materials are used, either as an intrinsically bonded or extrinsically doped component of polymers, light can be applied to motivate the microstructures through material response: shape or volume variation for mechanical functions; refractive index change for photonic devices; and conductivity and light emission for optoelectronic devices. Various photoinduced isomerization effects are good candidates for this purpose. For example, azobenzene and derivatives [69, 198] have two geometrical isomers, the *trans* and the *cis* forms. An isomerization reaction is a light- or thermally-induced interconversion of the two isomers. The *trans* isomer is thermally more stable. When irradiated with UV light a *trans*→*cis* conversion is promoted and the *cis*-form concentration increases, which is characterized by an enhancement in visible absorption. Visible light irradiation pushes the reaction in the opposite direction. Figure 60a shows azobenzene as an example. An important class of photochromatic materials, diarylethenes also have

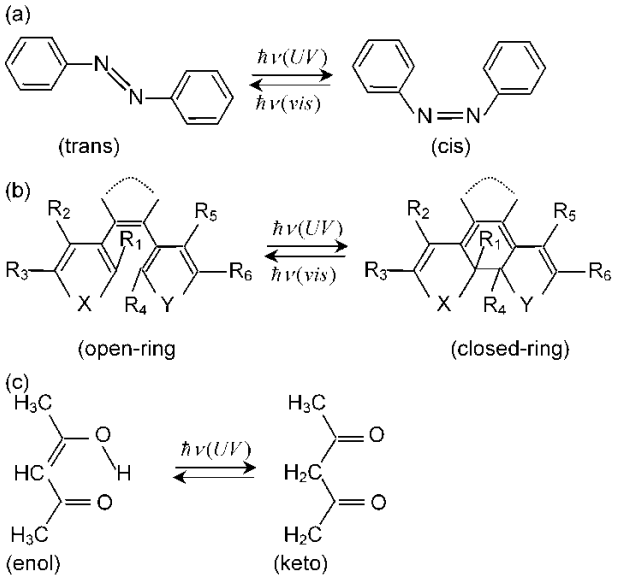

Fig. 60 Several promising photoactive materials that could be used for actuating nanodevices. **a** Photoisomerization due to *cis-trans* transition, **b** photoisomerization from ring close-open mechanism; and **c** optical tautomerization

two forms (Fig. 60b) [67, 198, 199]: open ring and closed ring, which can be interswitched by irradiation by UV and visible light, too. In both cases, the shape and size of molecules are different for the two forms, which may cause a volume change of material. However, these effects are too weak to use since the photosensitive molecules are distributed into a host polymer as a small percentage, <10% say, to avoid aggregation. It is easier to render intramolecular interval modification than impart appreciable volume change. Special measures should be taken to increase the concentration of photosensitive molecules in the matrix [199].

β-Diketone compounds, like acetylacetone, are known to exist in forms of enol and diketo tautomers (Fig. 60c). [200] A conversion from enol to diketo occurs with UV irradiation. Watanabe et al. [201] prepared a hydrogel of a cantilever shape by two-photon photopolymerizing a comonomer solution containing caryloylacetone, acrylamide, and *N,N*'-methylene bisacrylamide. They illuminated UV (244 nm) light from one side of the cantilever, which was then deflected due to the photoconversion-induced volume expansion. Compared with the previous two mechanisms, here the tautomerization reaction isn't reversible and needs an aqueous ambient for operation, therefore, the UV irradiation of the cantilever is more like a final step of the prototyping.

Functionalizing microdevices using photoactive materials is a promising direction for MEMS; however, a lot more research is needed to find suitable materials and actuating mechanisms.

6 Future Prognosis

Nanophotonics addresses detecting, controlling and fabricating features in a spatial volume less than that defined by the optical diffraction limit. There are basically two routes to access the SDL regime. First is the near-field, which works based on sharp-tip induced photon tunneling of an evanescent field, built either on a scanning tip end (apetured tip) or on a sample surface (apertureless tip). The other technology is multi-photon technology, which possesses the SDL spatial resolution due to nonlinear laser-matter interactions. Nanofabrication – production of nano-sized devices or devices with nanofeatures – is an important task of nanophotonics. Near-field fabrication, restrained by the nature of exponential decay of evanescent fields, gives rise only to 2D structures, which can't satisfy the requirement of three dimensional micro-nanodevices and systems.

Two-photon photopolymerization, as an important method of multiphoton laser micro-nanofabrication, is expected to play an essential role in producing polymer-based optoelectronic and MEMS devices. A lot of work has been done along this line as we have reviewed in the previous sections of this chapter. Future research in materials, optics and fabrication of functional devices are needed to further its use in diverse scientific research fields and industrial applications.

From a materials point of view, synthesis of two-photon chromophores with even higher two-photon cross-sections is required, so that photopolymerization may be induced by less expensive picosecond, nanosecond and even CW lasers for commercial applications. Also the high δ materials would enable polymerization simultaneously from multibeam split out of one output of a laser for batch production. Also desired is the use of copolymerization of functional molecules and resins, or doping of other functional components like nanocrystals into resins, so that particular functions could be imparted to polymerized devices. Uniform dispersion of the alien components into the matrix polymer is an important problem to solve. Finally, we need to synthesize functional polymers; in other words, instead of doping, we directly induce functional chromophores as a bonded component of monomers or oligomers, so that functions such as light-emission, polarization control, refractive index tuning and so forth become more pronounced.

From the optical standpoint, tailoring the point spread function to produce a spherical voxel shape is advantageous for precise 3D prototyping. Another important line of work is finding suitable mechanisms to construct

a parallel production system. This may be accomplished by a diffraction beam splitter or by a microlens array. The latter is preferable because (i) foci number increases simply by expanding the area of a lens array since a single micro lens occupies a fixed size, for example, 250 μm diameter (ii) no further focusing is needed since each beamlet is naturally focused after passing through the array. Measures should be taken to ensure a uniform power distribution for sensitive control of polymerization from each beam. Without the capability of batch production, the cost of single-beam writing would severely hinder the versatile industrial use of the technology.

References

1. Odian G (1991) Principles of polymerization, 3rd edn. Wiley, New York
2. Fouassier JP, Rabek JF (1990) Lasers in polymer science and technology. CRC Press, Boca Taton, FL
3. Reiser A (1989) Photoreactive polymers: The science and technology of resists. Wiley, New York
4. Fouassier JP, Rabek JF (1993) (eds) Radiation curing in polymer science and technology. Elsevier, London
5. Fouassier JP (1995) Photoinitiation, photopolymerization and photocuring: Fundamentals and applications. Hanser, Munich Vienna New York
6. Nakagawa T, Marutani Y (1996) (eds) Layered manufacturing systems: the latest development of three-dimensional copying technnologies (in Japanese). Kogyo Chosakai, Japan
7. Zhang X, Jiang XN, Sun C (1999) Sensor Actuat 77:149
8. Jiang XN, Sun C, Zhang X, Xu B, Ye YH (2000) Sensor Actuat 87:72
9. Bertsch A, Lorenz H, Renaud (1999) Sensor Actuat 73:14
10. Maruo S, Nakamura O, Kawata S (1997) Opt Lett 22:132
11. Parthenopoulos DA, Rentzepis PM (1989) Science 245:843
12. Denk W, Strickler JH, Webb WW (1990) Science 248:73
13. Kawata S, Sun HB, Tanaka T, Takada K (2001) Nature 412:697
14. Tanaka T, Sun HB, Kawata S (2002) Appl Phys Lett 80:312
15. Sun HB, Matsuo S, Misawa H (1999) Appl Phys Lett 74:786
16. Sun HB, Kawakami T, Xu Y, Ye JY, Matsuo S, Misawa H, Miwa M, Kaneko R (2000) Opt Lett 25:1110
17. Sun HB, Mizeikis V, Xu Y, Juodkazis S, Ye JY, Matsuo S, Misawa H (2001) Appl Phys Lett 79:1
18. Sun HB, Tanaka T, Takada K Kawata S (2001) Appl Phys Lett 79:1411
19. Sun HB, Takada K, Kawata S (2001) Appl Phys Lett 79:3173
20. Sun HB, Tanaka T, Kawata S (2002) Appl Phys Lett 80:3673
21. Albota M, Beljonne D, Bredas JL, Ehrlich JE, Fu JY, Heikal AA, Hess SE, Kogej T, Levin MD, Marder SR, McCord-Maughon D, Perry JW, Rockel H, Rumi M, Subramaniam C, Webb WW, Wu XL, Xu C (1998) Science 281:1653
22. Cumpston BH, Ananthavel SP, Barlow S, Dyer DL, Ehrlich JE, Erskine LL, Heikal AA, Kuebler SM, Lee IYS, McCord-Maughon D, Qin JQ, Rockel H, Rumi M, Wu XL, Marder SR, Perry JW (1999) Nature 398:51

23. Zhou WH, Kuebler SM, Braun KL, Yu TY, Cammack JK, Ober CK, Perry JW, Marder SR (2002) Science 296:1106
24. Belfield KD, Schafer KJ, Liu YU, Liu J, Ren XB, Van Stryland EW (2000) J Phys Org Chem 13:837
25. Bhawalkar JD, He GS, Prasad PN (1996) Rep Prog Phys 59:1041
26. Lehmann O, Stuke M (1995) Science 270:1644
27. Wanke MC, Lehmann O, Muller K, Wen QZ, Stuke M (1997) Science 275:1284
28. Daneshvar K, Raissi M, Bobbio SM (2000) J Appl Phys 88:2205
29. Shiomi M, Yoshidome A, Abe F, Osakada K (1999) Int J Mach Tool Manu 39:237
30. Zhang YZ, Shi LK, Zhang PZ, Xu J (2000) Rare Metal Mat Eng 29:361
31. Sun HB, Xu Y, Juodkazis S, Sun K, Watanabe M, Matsuo S, Misawa H, Nishii J (2001) Opt Lett 26:325
32. Sun HB, Xu Y, Matsuo S, Misawa H (1999) Opt Rev 6:396
33. Menzel R (2001) Photonics: Linear and nonlinear interactions of laser light and matter, Springer, Berlin Heidelberg New York
34. Saleh BEA, Teich MC (1991) Fundamentals of photonics. Wiley, New York
35. Milonni PW, Eberly JH (1988) Lasers. Wiley, New York
36. Mei DB, Cheng BY, Hu W, Li ZL, Zhan DH (1995) Opt Lett 20:429
37. Campbell M, Sharp DN, Harrison MT, Denning RG, Turberfield AJ (2000) Nature 404:53
38. Shoji S, Kawata S (2000) Appl Phys Lett 76:2668
39. Kondo T, Matsuo S, Juodkazis S, Misawa H (2001) Appl Phys Lett 79:725
40. Allmen M, Blatter A (1995) Laser-beam interactions with materials. 2nd edn. Springer Berlin Heidelberg New York
41. Grigoryants AG (1994) Basics of laser material processing. CRC, New York
42. Shen YR (1984) The principles of nonlinear optics. Wiley, New York
43. Boyd RW (1992) Nonlinear optics. Academic, San Diego
44. Kieffer JC, Matte JP, Belair S, Chaker M, Audebert P, Pepin H, Maine P, Strickland D, Bado P, Mourou G (1989) IEEE J Quantum Elect 25:2640
45. Bado P (2000) Laser Focus World 36:73
46. Diels JC, Rudolph W (1996) Ultrashort laser pulse phenomena: fundamentals, techniques, and applications on a femtosecond time scale (Optics and Photonics). Academic, New York
47. Saeta P, Wang JK, Siegal Y, Bloembergen N, Mazur E (1991) Phys Rev Lett 67:1023
48. Glezer EN, Milosavljevic M, Huang L, Finlay RJ, Her TH, Callan JP, Mazur E (1996) Opt Lett 21:2023
49. Glezer EN, Mazur E (1997) Appl Phys Lett 71:882
50. Goeppert-Mayer M (1931) Ann Phys 9:273
51. Kaiser W, Garrett CGB (1961) Phys Rev Lett 7:229
52. Eberly JH, Lambropoulos P (1978) (eds) Multiphoton processes : proceedings of an international conference at the University of Rochester, Rochester, N.Y., June 6–9, 1977. Wiley, New York
53. Kano H, Kawata S (1996) Opt Lett 21:1848
54. Higdon PD, Torok P, Wilson T (1999) J Microsc-Oxford 193:127
55. Hell S, Stelzer EHK (1992) Opt Commun 93:277
56. Bhawalkar JD, He GS, Park CK, Zhao CF, Ruland G, Prasad PN (1996) Opt Commun 124:33
57. He GS, Xu GC, Prasad PN, Reinhardt BA, Bhatt JC, Dillard AG (1995) Opt Lett 20:435
58. Fisher WG, Partridge WP, Dees C, Wachter EA (1997) Photochem Photobiol 66:141
59. He GS, Bhawalkar JD, Zhao CF, Park CK, Prasad PN (1995) Opt Lett 20:2393

60. Smith NI, Fujita K, Nakamura O, Kawata S (2001) Appl Phys Lett 78:999
61. Schaffer CB, Nishimura N, Glezer EN, Kim AMT, Mazur E (2002) Opt Express 10:196
62. Strickler JH, Webb WW (1991) Opt Lett 16:1780
63. Kawata S, Kawata Y (2000) Chem Rev 100:1777
64. Liphardt M, Goonesekera A, Jones BE, Ducharme S, Takacs JM, Zhang L (1994) Science 263:367
65. Moerner WE (1987) (ed) Persistent spectral hole burning: Science and applications. Springer, Berlin Heidelberg New York
66. Kim MK, Kachru R (1989) Opt Lett 14:423
67. Irie M (2000) Chem Rev 100:1685
68. Toriumi A, Herrmann JM, Kawata S (1997) Opt Lett 22:555
69. Sekkat Z, Knoll WJ (1995) J Opt Soc Am B 12:1855
70. Toriumi A, Kawata S, Gu M (1998) Opt Lett 23:1924
71. Kawata Y, Ishitobi H, Kawata S (1998) Opt Lett 23:756
72. Meerholz K, Volodin BL, Sandalphon, Kippelen B, Peyghambarian, N (1994) Nature 371:497
73. Day D, Gu M, Smallridge A (2001) Adv Mater 13:1005
74. Day D, Gu M (1999) Opt Lett 24:288
75. Tanaka T, Yamaguchi K, Yamamoto S (2002) Opt Commun 212:45
76. Qiu JR, Kojima K, Miura K, Mitsuyu T, Hirao K (1999) Opt Lett 24:786
77. Miura K, Qiu JR, Fujiwara S, Sakaguchi S, Hirao K (2002) Appl Phys Lett 80:2263
78. Sun HB, Juodkazis S, Watanabe M, Matsuo S, Misawa H, Nishii J (2000) J Phys Chem B 104:3450
79. Yamasaki K, Juodkazis S, Watanabe M, Sun HB, Matsuo S, Misawa H (2000) Appl Phys Lett 76:1000
80. Watanabe M, Sun HB, Juodkazis S, Takahashi T, Matsuo S, Suzuki Y, Nishii J, Misawa H (1999) Jpn J Appl Phys 37: L1527
81. Watanabe M, Juodkazis S, Sun HB, Matsuo S, Misawa H, Miwa M, Kaneko R (1999) Appl Phys Lett 74:3957
82. Watanabe M, Juodkazis S, Sun HB, Matsuo S, Misawa H (2000) Appl Phys Lett 77:13
83. Watanabe M, Juodkazis S, Sun HB, Matsuo S, Misawa H (1999) Phys Rev B 60:9959
84. Miura K, Qiu JR, Inouye H, Mitsuyu T, Hirao K (1997) Appl Phys Lett 71:3329
85. Minoshima K, Kowalevicz AM, Hartl I, Ippen EP, Fujimoto JG (2001) Opt Lett 26:1516
86. Homoelle D, Wielandy S, Gaeta AL, Borrelli NF, Smith C (1999) Opt Lett 24:1311
87. Minoshima K, Kowalevicz AM, Ippen EP, Fujimoto JG (2002) Opt Express 10:645
88. Li Y, Watanabe W, Yamada K, Shinagawa T, Itoh K, Nishii J, Jiang YY (2002) Appl Phys Lett 80:1508
89. Kawamura K, Sarukura N, Hirano M, Hosono H (2001) Appl Phys Lett 78:1038
90. Kawamura K, Sarukura N, Hirano M, Ito N, Hosono H (2001) Appl Phys Lett 79:1228
91. Watanabe W, Kuroda D, Itoh K, Nishii J (2002) Opt Express 10:978
92. Yablonovitch E (1987) Phys Rev Lett 58:2059
93. John S (1987) Phys Rev Lett 58:2486
94. Joannopoulos JD, Meade RD, Winn JN (1995) Photonic crystals: Modeling the flow of light. Princeton Univ Press, Singapore
95. Ho KM, Chan CT, Soukoulis (1990) Phys Rev Lett 65:3152
96. Fukuda K, Sun H, Matsuo S, Misawa H (1998) Jpn J Appl Phys 37: L508
97. Sun HB, Song JF, Xu Y, Matsuo S, Misawa H, Du GT, Liu SY (2000) J Opt Soc Am B 17:476

98. Sun HB, Xu Y, Ye JY, Matsuo S, Misawa H, Song JF, Du GT, Liu SY (2000) Jpn J Appl Phys 39: L591
99. Wu PW, Cheng W, Martini IB, Dunn B, Schwartz BJ, Yablonovitch E (2000) Adv Mater 12:1438
100. Stellacci F, Bauer CA, Meyer-Friedrichsen T, Wenseleers W, Alain V, Kuebler SM, Pond SJK, Zhang YD, Marder SR, Perry JW (2002) Adv Mater 14:194
101. Horiyama M, Sun HB, Miwa M, Matsuo S, Misawa H (1999) Jpn J Appl Phys Lett 38: L212
102. Maruo S, Ikuta K (2000) Appl Phys Lett 76:2656
103. Maruo S, Ikuta K (2002) Sensor Actuat A-Phys 100:70
104. Pappas SP (1985) Radiation Phys Chem25:633
105. Pappas SP (1992) (ed) Radiation curing science and technology. Plenum, New York
106. Fouassier JP, Rabek JF (1993) (eds) Radiation curing in polymer science and technology. Elsevier, London
107. Scully MO, Zubairy MS (1997) Cambridge Univ Press
108. Hopfield JJ, Worlock JM, Park KJ (1963) Phys Rev Lett 11:414
109. Frohlich D, Staginnus B (1967) Phys Rev Lett 19:476
110. Pao YH and Rentzepis PM (1965) Appl Phys Lett 6:93
111. Chin SL, Bedard G (1971) Phys Lett 36A: 271
112. Papouskova Z, Pola J, Bastl Z, Tiaskal J (1990) J Mecromol Sci Chem A27:1015
113. Morita H, Sadakiyo T (1995) J Photochem Photobiol A 87:163
114. Lee KS, Lee JH, Choi HY, Cha M, Chung MA, Kim YJ, Jung SD (2001) Mol Cryst Liq Cryst 370:155
115. Chung MA, Lee KS, Jung SD (2002) ETRI J 24:221
116. Li CD, Luo L, Wang SF, Huang WT, Gong QH, Yang YY, Feng SJ (2001) Chem Phys Lett 340:444
117. Belfield KD, Schafer KJ, Mourad WJ (2000) J Org Chem 65:4475
118. Jortner J, Ratner M (1997) (eds) Molecular electronics. Blackwell Science, London
119. Belfield KD, Hagan DJ, Van Stryland EW, Schafer KJ, Negres RA (1999) Org Lett 1:1575
120. Belfield KD, Schafer KJ, Alexander MD Jr (2000) Chem Mater 12:1184
121. Adronov A, Frechet JMJ, He GS, Kim KS, Chung SJ, Swiatkiewicz J, Prasad PN (2000) Chem Mater 12:2838
122. Hu Y (2001) MRS Bull 26:595
123. Adronov A, Frechet JMJ, He GS, Kim KS, Chung SJ, Swiatkiewicz J, Prasad PN (2000) Chem Mater 12:2838
124. Rentzepis PM (1989) US Patent 07 342 978
125. Bradbury S, Bracegirdle B (1998) Introduction to light microscopes. Springer, Berlin Heildelberg New York
126. Born M, Wolf E (1999) Principle of Optics, 7th edn. Cambridge Univ Press, Cambridge
127. Witzgall G, Vrijen R, Yablonovitch E, Doan V, Schwartz BJ (1998) Opt Lett 23:1745
128. Madou MJ (2002) Fundamentals of microfabrication: The science of miniaturization, 2nd edn. CRC Press, New York
129. Lyshevski SE (2002) MEMS and NEMS: Systems, devices, and structures. CRC Press, New York
130. (Anon) (2002) Laser Focused World 38 11
131. Cartlidge E (2002) Phys World 15:10
132. Quake SR, Scherer A (2000) Science 290:1536
133. Xia YN, Whitesides GM (1998) Ann Rev Mater Sci 28:153

134. Kumar A, Whitesides GM (1993) Appl Phys Lett 63:2002
135. Chou SY, Krauss PR, Renstrom PJ (1995) Appl Phys Lett 67:3114
136. Kim E, Xia Y, Whitesides GM (1995) Nature 376:581
137. Terris BD, Mamin HJ, Best ME, Logan JA, Rugar D (1996) Appl Phys Lett 69:4262
138. Masuda H, Fukuda K (1995) Science 268:1446
139. Xia Y, Kim E, Zhao X-M, Rogers JA, Prentiss M, Whitesides GM (1996) Science 273:347
140. Wu ES, Strickler JH, Harrell WR, Webb WW (1990) SPIE Proc 1674:776
141. Maruo S, Kawata S (1998) J IEEE MEMS, 7:411
142. Wu PW, Dunn B, Yablonovitch E, Doan V, Schwartz BJ (1999) J Opt Soc Am B 16:605
143. Brodeur A, Chin SL (1999) J Opt Soc Am B 16:637
144. Stuart BC, Feit MD, Herman S, Rubenchik AM, Shore BW, Perry MD (1996) Phys Rev B 53:1749
145. vonderLinde D, Schuler H (1996) J Opt Soc Am B 13:216
146. Boiko Y, Costa JM, Wang M, Esener S (2001) Opt Express 8:571
147. Joshi MP, Pudavar HE, Swiatkiewicz J, Prasad PN, Reianhardt BA (1999) Appl Phys Lett 74:170
148. Kirkpatrick SM, Baur JW, Clark CM, Denny LR, Tomlin DW, Reinhardt BR, Kannan R, Stone MO (1999) Appl Phys A 69:461
149. Matsumoto K (1997) P IEEE 85:612
150. Sauer BB, McLean RS, Thomas RR (1998) Langmuir 14:3045
151. Tarun A, Daza MRH, Hayazawa N, Inouye Y, Kawata S (2002) Appl Phys Lett 80:3400
152. Flory PJ (1952) Principles of polymer chemistry. Cornell University Press, New York
153. Schulz GV (1997) Chem Ber 80:232
154. Bolon DA, Webb KK (1978) J Appl Polymer Sci 22:2543
155. Decker C, Faure J, Fizet M, Rychla L (1979) Photog Sci Eng 23:137
156. Hageman HJ (1985) Prog Organic Coatings 13:123
157. Booth MJ, Wilson T (2001) J Biomed Opt 6:266
158. Booth MJ, Wilson T (2001) J Microsc-Oxford 201:416
159. Booth MJ, Neil MAA, Juskaitis R, Wilson T (2002) P Natl Acad Sci USA 99:5788
160. Fujimoto M, Aoshima S, Hosoda M, Tsuchiya Y (1999) Opt Lett 24:850
161. DeVoe RJ, Kalveit H, Leatherdale CA, Williams TR (2002) Proc SPIE
162. Stamners J (1986) Waves in focal region. Adam Hilgar, Bristol
163. Gu M (1999) Advanced optical imaging Theory. Springer, Berlin Heidelberg New York
164. Bahlmann K, Hell SW (2000) Appl Phys Lett 77:612
165. T. Wilson (1990) (ed) Confocal microscopy. Academic, London
166. Berger V, GauthierLafaye O, Costard E (1997) J Appl Phys 82:60
167. Berger V, GauthierLafaye O, Costard E (1997) Electron Lett 33:425
168. Nakata Y, Okada T, Maeda M (2002) 81: 4239
169. Sharp DN, Campbell M, Dedman ER, Harrison MT, Denning RG, Turberfield A (2002) J Opt Quant Electron 34:3
170. Yang S, Megens M, Aizenberg J, Wiltzius P, Chaikin PM, Russel WB (2002) Chem Mater 14:2831
171. Segawa H, Yoshida K, Kondo T, Matsuo S, Misawa H (2003) J Sol-Gel Sci Techn 26:1023
172. Campagnola PJ, Delguidice DM, Epling GA, Hoffacker KD, Howell AR, Pitts JD, Goodman SL (2000) Macromolecules 33:1511
173. Nakayama Y, Matsuda T (1999) J Biomed Mater Res 48:511
174. Okino H, Nakayama Y, Tanaka M, Matsuda T (2002) J Biomed Mater Res 59:233

175. Pitts JD, Campagnola PJ, Epling GA, Goodman SL (2000) Macromolecules 33:1514
176. Zhou WH, Kuebler SM, Carrig D, Perry JW, Marder SR (2002) J Am Chem Soc 124:1897
177. Zhou WH, Kuebler SM, Braun KL, Yu TY, Cammack JK, Ober CK, Perry JW, Marder SR (2002) Science 296:1106
178. Blanco A, Chomski E, Grabtchak S, Ibisate M, John S, Leonard SW, Lopez C, Meseguer F, Miguez H, Mondia JP, Ozin GA, Toader O, van Driel HM (2000) Nature 405:437
179. Gruning U, Lehmann V, Engelhardt CM (1995) Appl Phys Lett 66:3254
180. Xu Y, Sun HB, Ye JY, Matsuo S, Misawa H (2001) J Opt Soc Am B 18: 1084
181. Noda S, Tomoda K, Yamamoto N, Chutinan A (2000) Science 289:604
182. Kawakami S (1997) Electron Lett 33:1260
183. Biswas R, Chan CT, Sigalas M, Soukoulis CM, Ho KM (1995) In: Soukoulis CM (ed) Photonic band gap materials. Kluwer Academic Press, London, p 23
184. Straub M, Gu M (2002) Opt Lett 27:1824
185. Noda S, Chutinan A, Imada M (2000) Nature 407:608
186. Noda S, Yokoyama M, Imada M, Chutinan A, Mochizuki M (2001) Science 293:1123
187. Salaneck WR, Seki K, Kahn A, Pireaux JJ (2001) (eds) Conjugated polymer and molecular interfaces: science and technology for photonic and optoelectronic applications. Marcel Dekker, New York
188. Taton TA, Norris DJ (2002) Nature 416:685
189. Lee WM, Pruzinsky SA, Braun PV (2002) Adv Mater 14:271
190. Ashkin A (1970) Phys Rev Lett 24:156
191. Ashkin A, Schutze K, Dziedzic JM, Eutenuer U, Schliwa M (1990) Nature 348:346
192. Ashkin A (1992) Biophys J 61:569
193. Higurashi E, Sawada R, Ito T (1998) Appl Phys Lett 71:2951
194. Gauthier RC (1995) Appl Phys Lett 67:2269
195. Galajda P, Ormos P (2001) Appl Phys Lett 78:249
196. Friese MEJ, Enger J, Rubinsztein-Dunlop H, Heckenberg NR (1996) Phys Rev A 54:1593
197. He H, Friese MEJ, Heckenberg NR, Rubinsztein-Dunlop H (1995) Phys Rev Lett 75:826
198. Sekkat Z, Knoll W (2002) (eds) Photorefractive organic thin films. Academic, New York
199. Kaneuchi Y, Kawai T, Hamaguchi M, Yoshino K, Irie M (1997) Jpn J Appl Lett, 36:3736
200. Masuda S, Sertowa N, Petkov I (1997) J Polymer Sci A 35:3683
201. Watanabe T, Akiyama M, Totani K, Kuebler SM, Stellacci F, Wenseleers W, Braun K, Marder SR, Perry JW (2002) Adv Funct Mater 12:611

Editor: Kwang-Sup Lee Received: July 2003